

SHORT-TERM FORMATION KINETICS OF THE CONTINUOUS GALVANIZING  
INTERFACIAL LAYER ON MN-CONTAINING STEELS



SHORT-TERM FORMATION KINETICS OF THE CONTINUOUS GALVANIZING  
INTERFACIAL LAYER ON MN-CONTAINING STEELS

By

SAMANEH ALIBEIGI, B.A.Sc., M.S.Sc.

A Thesis

Submitted to the School of Graduate Studies

In Partial Fulfillment of the Requirements

For the Degree

Doctor of Philosophy

McMaster University

© Copyright by Samaneh Alibeigi, September 2014

Doctor of Philosophy (2014)

McMaster University

(Materials Science & Engineering)

Hamilton, Ontario

TITLE: Short-Term Formation Kinetics of the Continuous  
Galvanizing Interfacial Layer on Mn-containing Steels

AUTHOR: Samaneh Alibeigi, M.A.Sc. (K.N.Toosi University of  
Technology)

SUPERVISOR: Dr. Joseph R. McDermid

NUMBER OF PAGES: xv, 152

## Abstract

Aluminium is usually added to the continuous hot-dip galvanizing bath to improve coating ductility and adhesion through the rapid formation of a thin Fe-Al intermetallic layer at the substrate-liquid interface, thereby inhibiting the formation of brittle Fe-Zn intermetallic compounds. On the other hand, Mn is essential for obtaining the desired microstructure and mechanical properties in advanced high strength steels, but is selectively oxidized in conventional continuous galvanizing line annealing atmospheres. This can deteriorate reactive wetting by the liquid Zn(Al,Fe) alloy during galvanizing and prevent the formation of a well developed Fe-Al interfacial layer at the coating/substrate interface, resulting in poor zinc coating adherence and formability. However, despite Mn selective oxidation and the presence of surface MnO, complete reactive wetting and a well developed Fe-Al interfacial layer have been observed for Mn-containing steels. These observations have been attributed to the aluminothermic reduction of surface MnO in the galvanizing bath. According to this reaction, MnO is reduced by the bath dissolved Al, so the bath can have contact with the substrate and form the desired interfacial layer.

Heat treatments compatible with continuous hot-dip galvanizing were performed on four different Mn-containing steels whose compositions contained 0.2-3.0 wt% Mn. It was determined that substrate Mn selectively oxidized to MnO for all alloys and process atmospheres. Little Mn surface segregation was observed for the 0.2Mn steel, as would be expected because of its relatively low Mn content, whereas the 1.4Mn through 3.0Mn steels showed considerable Mn-oxide surface enrichment. In addition, the proportion of

the substrate surface covered with MnO and its thickness increased with increasing steel Mn content.

A galvanizing simulator equipped with a He jet spot cooler was used to arrest the reaction between the substrate and liquid zinc coating to obtain well-characterized reaction times characteristic of the timescales encountered while the strip is resident in the industrial continuous galvanizing bath and short times after in which the Zn-alloy layer continues to be liquid (i.e. before coating solidification). Two different bath dissolved Al contents (0.20 and 0.30 wt%) were chosen for this study. The 0.20 wt% Al bath was chosen as it is widely used in industrial continuous galvanizing lines. The 0.30 wt% Al bath was chosen to (partially) compensate for any dissolved Al consumption arising from MnO reduction in the galvanizing bath.

The Al uptake increased with increasing reaction time following non-parabolic growth kinetics for all experimental steels and dissolved Al baths. For the 0.20 wt% dissolved Al bath, the interfacial layer on the 1.4Mn steel showed the highest Al uptake, with the 0.2Mn, 2.5Mn and 3.0Mn substrates showing significantly lower Al uptake. However, increasing the dissolved bath Al to 0.30 wt% Al resulted in a significantly increased Al uptake being observed for the 2.5Mn and 3.0Mn steels for all reaction times. These observations were explained by the combined effects of the open microstructures associated with the multi-phase nature of an oxide-containing interfacial layer and additional Al consumption through MnO reduction. For instance, in the case of the 1.4Mn steel, the more open interfacial layer structure accelerated Fe diffusion through the interfacial layer and increased Al uptake versus the 0.2Mn substrate for the same bath Al.

However, in the case of the 2.5Mn and 3.0Mn substrates and 0.20 wt% Al bath, additional Al consumption through MnO reduction caused the interfacial layer growth to become Al limited, whereas the very open structure dominated growth in the case of the 0.30 wt% Al bath and resulted in the changing the growth kinetics from mixed diffusion-controlled to a more interface controlled growth mode.

A kinetic model based on oxide film growth (Smeltzer et al. 1961, Perrow et al. 1968) was developed to describe the Fe-Al interfacial layer growth kinetics within the context of the microstructural evolution of the Fe-Al interfacial layer for Mn-containing steels reacted in 0.20 wt% and 0.30 wt% dissolved Al baths. It indicated that the interfacial layer microstructure development and the presence of MnO at the interfacial layer had significant influence on the effective diffusion coefficient and interfacial layer growth rate. However, in the cases of the 2.5Mn and 3.0Mn steels in 0.20 wt% Al bath, the kinetic model could not predict the interfacial layer Al uptake, since the Fe-Al growth was Al limited. In fact, in these cases, additional Al was consumed for reducing their thicker surface MnO layer, resulted in limiting the dissolved Al available for Fe-Al growth.

## **Acknowledgments**

I would like to express my sincere gratitude to my supervisor, Dr. Joseph. R. McDermid, for his encouragement, scientific guidance and support during my time at McMaster. I tried my best to be one of his excellent students and make him proud of me.

I would also like to thank my supervisory committee members Dr. Ken Coley and Dr. Joey Kish for their valuable suggestions and comments.

The following people are thanked for their assistance with the experimental work: John Thomson, Mariana Budiman and Ray Fullerton from the McMaster Steel Research Centre (Galvanizing Simulator), Doug Culley and John Rodda for their help in the MSE labs and ICP training, Fred Pearson (TEM), Dr. Carmen Andrei (TEM), Dr. Steve Koprach (SEM training), Chris Butcher (SEM and optical microscopy training), Julia Huang (FIB) and Travis Casagrande (High Resolution SEM) from the Canadian Centre for Electron Microscopy, Mark MacKenzie (Welding training), Dr. Li Sun (XPS) from ArcelorMittal Dofasco and Shihong Xu (SAM) from ACSES, the Alberta Centre for Surface Engineering and Science.

I would also like to thank USSC for provision of experimental materials (0.2Mn and 1.4Mn steels) and the Academic User Access Facility (AUAF) program of the Materials Technology Laboratory of CANMET for fabrication of the two high Mn steels used in the experiments.

I would like to thank U.S. Steel Canada, Xstrata Zinc, the Natural Sciences and Engineering Research Council of Canada (NSERC) and the members of the McMaster Steel Research Centre for their financial support.

My parents and sister, Sepideh, deserve special gratitude. Their spiritual support, love and understanding are invaluable.

# TABLE OF CONTENTS

ABSTRACT .....	iii
ACKNOWLEDGMENTS .....	vi
TABLE OF CONTENTS .....	viii
LIST OF FIGURES .....	x
LIST OF TABLES .....	xv
<b>1 INTRODUCTION.....</b>	<b>1</b>
<b>2 LITERATURE REVIEW .....</b>	<b>4</b>
2.1 Dual phase steels .....	4
2.2 Continuous hot-dip galvanizing .....	5
2.3 Selective oxidation .....	7
2.3.1 Selective oxidation during annealing .....	8
2.3.1.1 The transition between internal and external oxidation .....	11
2.3.2 Selective oxidation of Mn-containing steels .....	14
2.4 Fe-Al interfacial layer .....	17
2.4.1 Interfacial layer composition and morphology .....	21
2.4.2 Interfacial layer formation .....	24
2.4.3 Parameters influencing interfacial layer formation.....	27
2.4.3.1 Reaction time.....	27
2.4.3.2 Bath dissolved Al .....	30
2.4.3.3 Substrate Mn content.....	33
2.4.3.4 Bath temperature .....	39
2.5 Kinetic models of interfacial layer growth.....	41
<b>3 RESEARCH OBJECTIVES .....</b>	<b>51</b>
<b>4 EXPERIMENTAL METHODS .....</b>	<b>53</b>
4.1 Experimental materials.....	53
4.2 McMaster galvanizing simulator.....	54
4.3 Sample preparation.....	57
4.4 Annealing and galvanizing experimental parameters .....	60
4.4.1 Reaction time calculation.....	62

4.5	Analytical procedures .....	65
4.5.1	X-ray photoelectron spectroscopy (XPS) .....	65
4.5.2	Scanning electron microscopy (SEM) .....	66
4.5.3	Scanning Auger microscopy (SAM) .....	67
4.5.4	Transmission electron microscopy (TEM) .....	68
4.5.5	Inductively coupled plasma spectroscopy (ICP) .....	70
<b>5.</b>	<b>RESULTS: SELECTIVE OXIDATION AND INTERFACIAL LAYER FORMATION .....</b>	<b>72</b>
5.1	Steel selective oxidation during annealing .....	72
5.1.1	X-ray photoelectron spectroscopy analysis .....	72
5.1.2	Scanning electron microscopy analysis .....	76
5.1.3	Scanning Auger microscopy analysis .....	77
5.2	Fe-Al interfacial layer development .....	82
5.2.1	Zn-0.20 wt% dissolved Al bath .....	82
5.2.1.1	SEM analysis of the interfacial layer .....	82
5.2.1.2	TEM analysis of the steel/coating interface .....	88
5.2.1.3	ICP analysis of the Fe-Al interfacial layer .....	97
5.2.2	Zn-0.30 wt% dissolved Al bath .....	101
5.2.2.1	SEM analysis of the interfacial layer .....	101
5.2.2.2	TEM analysis of the steel/coating interface .....	106
5.2.2.3	ICP analysis of the Fe-Al interfacial layer .....	111
<b>6</b>	<b>DISCUSSION.....</b>	<b>114</b>
6.1	Selective oxidation of experimental alloys during annealing .....	114
6.2	Fe-Al interfacial layer development .....	116
6.3	Kinetic model of Fe-Al interfacial layer development .....	126
<b>7</b>	<b>CONCLUSIONS AND RECOMMENDATIONS .....</b>	<b>140</b>
7.1	Selective oxidation.....	140
7.2	Fe-Al interfacial layer development .....	140
7.3	Recommendations for future work .....	143
<b>8</b>	<b>REFERENCES .....</b>	<b>145</b>

## LIST OF FIGURES

Figure 2.1: Schematic of the continuous hot-dip galvanizing process (Marder 2000).	6
Figure 2.2: Thermodynamic stability of Fe and Mn oxides with respect to annealing temperature and oxygen partial pressure for a N <sub>2</sub> -5%H <sub>2</sub> atmosphere. The effect of Mn alloy activity on the Mn/MnO equilibrium is shown (Fine and Geiger 1979).	11
Figure 2.3: Microstructure of Zn coating formed after 300s immersion in a 450°C, pure zinc bath: 1 (Γ-Fe <sub>3</sub> Zn <sub>8</sub> ), 2 (δ-FeZn <sub>10</sub> ) and 3 (ζ-FeZn <sub>13</sub> ) (Jordan and Marder 1997).	18
Figure 2.4: Zn rich corner of the Zn-Al-Fe phase diagram; L is liquid, ζ is FeZn <sub>13</sub> , δ is FeZn <sub>10</sub> and η is Fe <sub>2</sub> Al <sub>5</sub> Zn <sub>x</sub> . Indicated on the phase diagram are isoactivity lines for Al (with respect to pure solid Al) and Fe (with respect to pure solid α-Fe) in the liquid phase (McDermid et al. 2007).	20
Figure 2.5: Metastable versus equilibrium configuration for the Zn-rich corner of the Zn-Al-Fe at 450°C (Nakano 2006).	21
Figure 2.6: Two types of morphology of Fe-Al interfacial layer observed in 0.18 wt% Al bath: a) small equiaxed crystals and b) coarse elongated crystals (Baril and L'Esperance 1999).	23
Figure 2.7: Morphology of the interfacial layer for a bath with 0.13 wt% dissolved Al (Chen et al. 2008).	24
Figure 2.8: Schematic representation of galvanizing reactions (Giorgi et al. 2005).	25
Figure 2.9: Schematic representation of interfacial layer formation on an IF steel surface using a 0.20 wt. % dissolved Al bath (Chen et al. 2008).	26
Figure 2.10: Interfacial layer Al uptake vs. (a) reaction time (Chen et al. 2008) and (b) immersion time (Toussaint et al., 1998) for a 0.20 wt% dissolved Al bath as a function of bath temperature.	29
Figure 2.11: Morphology of the interfacial layer for a 0.20 wt% dissolved Al bath at different reaction times: (a) 2.186s, (b) 3.086s, (c) 5.086s, and (d) 7.086s (Chen et al. 2008).	30
Figure 2.12: Effects of bath dissolved Al on interfacial Al uptake (a) for 470°C bath and different immersion times (Isobe 1992), (b) for 460°C bath and different immersion times (Toussaint et al., 1998) and (c) for 450°C-470°C baths (Liu and Tang 2004).	33

Figure 2.13: Change in MnO layer thickness vs. reaction time for a 460°C 0.20 wt% dissolved Al bath (Kavitha and McDermid 2012).	36
Figure 2.14: (a) HRTEM image of MnO–Zn interface, (b) EELS O–K edge spectra from Al <sub>2</sub> O <sub>3</sub> at the MnO–Zn interface, and (c) EELS Al–K edge spectra from Al <sub>2</sub> O <sub>3</sub> at the MnO–Zn interface. Arrows correspond to the characteristic energy loss peaks and configuration for Al <sub>2</sub> O <sub>3</sub> (Kavitha and McDermid 2012).	37
Figure 2.15: Schematic drawing illustrating the Fe-Al interfacial layer formation mechanism in the presence of surface oxides (Sagl et al. 2013).	38
Figure 2.16: Morphology of the interfacial layer for a bath with 0.13 wt% dissolved Al as a function of bath temperature: (a) 450 °C, (b) 460 °C, (c) 470 °C and (d) 480 °C (reaction times~4 s) (Chen et al. 2008).	40
Figure 2.17: Effects of bath temperature on interfacial layer Al uptake for a bath with 0.13 wt% dissolved Al and different immersion times (Chen et al. 2008).	40
Figure 2.18: Prediction of the mathematical model with experimental results (Toussaint et al. 1998).	44
Figure 2.19: The model of Giorgi et al. (2005) vs. the experimental results from Toussaint et al. (1998) for 0.20 wt% Al bath and 460°C bath temperature.	46
Figure 2.20: Al uptake as a function of reaction time for a 0.20 wt% dissolved Al bath (Chen et al. 2008).	49
Figure 4.1: a) The McMaster Galvanizing Simulator (MGS), b) Main Column and c) humidification system.	56
Figure 4.2: Schematic of the McMaster Galvanizing Simulator (Chen 2006).	57
Figure 4.3: Steel panel dimensions for a) selective oxidation experiments, b) reaction time calibration and c) galvanizing experiments.	59
Figure 4.4: Time, temperature and position log for a galvanized sample.	64
Figure 4.5: Steps of FIB sample preparation taken from the quench spot a) milling of trenches on either side of the sample, b) milling around the sample and welding of the probe to the sample, c) welding of the sample to the Cu grid and d) further milling to achieve an electron transparent sample.	69
Figure 5.1: XPS spectra as a function of sputtering depth for a) Fe and b) Mn (please note the difference in the depth scale order).	74

Figure 5.2: Mn XPS depth profile as a function of steel Mn content for the as-annealed alloys.	75
Figure 5.3: SEM images of the distribution of oxides on the steel surface annealed at -30°C dew point, (a) 0.2Mn, (b) 1.4Mn, (c) 2.5Mn, (d) 3.0Mn steels.	77
Figure 5.4: SAM elemental mapping of the 1.4Mn after Ar sputtering to 20 nm: (a) secondary electron image, (b) oxygen, (c) manganese and (d) iron.	79
Figure 5.5: SAM elemental mapping of the 2.5Mn after Ar sputtering to 20 nm: (a) secondary electron image, (b) oxygen, (c) manganese and (d) iron.	80
Figure 5.6: SAM elemental mapping of the 3.0Mn after Ar sputtering to 20 nm: (a) secondary electron image, (b) oxygen, (c) manganese and (d) iron.	81
Figure 5.7: SEM micrographs of the Fe-Al interfacial layer for the 0.2Mn steel galvanized in a 0.20 wt% dissolved Al bath for reaction times of: a) 2.13s, b) 3.55s, c) 5.56s and d) 7.61s.	83
Figure 5.8: SEM micrographs of the Fe-Al interfacial layer for the 1.4Mn steel galvanized in a 0.20 wt% dissolved Al bath for reaction times of: a) 2.20s, b) 3.62s, c) 5.66s and d) 7.68s.	84
Figure 5.9: SEM micrographs of the Fe-Al interfacial layer for the 2.5Mn steel galvanized in a 0.20 wt% dissolved Al bath for reaction times of: a) 2.23s, b) 3.65s, c) 5.66s and d) 7.71s.	86
Figure 5.10: SEM micrographs of the Fe-Al interfacial layer for the 3.0Mn steel galvanized in a 0.20 wt% dissolved Al bath for reaction times of: a) 2.23s, b) 3.65s, c) 5.66s and d) 7.71s.	87
Figure 5.11: High resolution SEM images of the Fe-Al interfacial layer for the 0.20 wt% dissolved Al bath as a function of alloy Mn content and reaction time for a 2s immersion time: a) 0.2Mn-3.55s, b) 1.4Mn-3.62s, c) 2.5Mn-3.65s and d) 3.0Mn-3.65s.	88
Figure 5.12: TEM micrograph and EDX mapping of the steel/coating interface for the 0.2Mn steel at 2.13s reaction time a) bright field image, b) Al, c) Fe and d) Zn maps.	89
Figure 5.13: TEM micrograph and EDX mapping of the steel/coating interface for the 1.4Mn steel at 2.20s reaction time a) bright field image, b) Al, c) Fe and d) Zn maps.	91

Figure 5.14: TEM micrograph and EDX mapping of the steel/coating interface for the 2.5Mn steel at 2.23s reaction time a) bright field image, b) Al, c) Fe and d) Zn maps.	93
Figure 5.15: TEM micrograph and EDX mapping of the steel/coating interface for the 2.5Mn steel at 2.23s reaction time a) bright field image, b) Al, c) Fe and d) Zn maps.	94
Figure 5.16: TEM micrograph and EDX mapping of the steel/coating interface for the 3.0Mn steel at 2.23s reaction time a) bright field image, b) Al, c) Fe and d) Zn maps.	95
Figure 5.17: TEM micrograph and EDX mapping of the steel/coating interface for the 3.0Mn steel at 2.23s reaction time a) bright field image, b) Al, c) Fe and d) Zn maps.	96
Figure 5.18: Interfacial layer Al-uptake as a function of reaction time and steel Mn content for a 0.20 wt% dissolved Al bath.	98
Figure 5.19: SEM micrographs of the Fe-Al interfacial layer for the 0.2Mn steel galvanized in a 0.30 wt% dissolved Al bath for reaction times of: a) 2.13s, b) 3.55s, c) 5.56s and d) 7.61s.	102
Figure 5.20: SEM micrographs of the Fe-Al interfacial layer for the 1.4Mn steel galvanized in a 0.30 wt% dissolved Al bath for reaction times of: a) 2.20s, b) 3.62s, c) 5.66s and d) 7.68s.	103
Figure 5.21: SEM micrographs of the Fe-Al interfacial layer for the 2.5Mn steel galvanized in a 0.30 wt% dissolved Al bath for reaction times of: a) 2.23s, b) 3.65s, c) 5.66s and d) 7.71s.	104
Figure 5.22: SEM micrographs of the Fe-Al interfacial layer for the 3.0Mn steel galvanized in a 0.30 wt% dissolved Al bath for reaction times of: a) 2.23s, b) 3.65s, c) 5.66s and d) 7.71s.	105
Figure 5.23: High resolution SEM images of the Fe-Al interfacial layer for the 0.30 wt% dissolved Al bath as a function of alloy Mn content and reaction time for a 2s immersion time: a) 0.2Mn-3.55s, b) 1.4Mn-3.62s, c) 2.5Mn-3.65s and d) 3.0Mn-3.65s.	106
Figure 5.24: TEM micrograph and EDX mapping of the steel/coating interface for the 1.4Mn steel at 2.20s reaction time a) bright field image, b) Al, c) Fe and d) Zn maps.	108

Figure 5.25: TEM micrograph and EDX mapping of the steel/coating interface for the 2.5Mn steel at 2.23s reaction time a) bright field image, b) Al, c) Fe and d) Zn maps.	109
Figure 5.26: TEM micrograph and EDX mapping of the steel/coating interface for the 2.5Mn steel at 7.71s reaction time a) bright field image, b) Al, c) Fe and d) Zn maps.	110
Figure 5.27: Interfacial layer Al-uptake as a function of reaction time and steel Mn content for the 0.30 wt% dissolved Al bath.	112
Figure 6.1: MnO layer thickness as a function of substrate Mn content.	115
Figure 6.2: Comparison of interfacial layer Al uptake as a function of steel Mn content and bath Al content for: a) 2s, b) 4s, c) 6s and d) 8s reaction times.	118
Figure 6.3: Interfacial layer Al uptake and Fe dissolution from the strip versus bath dissolved Al for a 460 °C bath (Liu and Tang 2004).	119
Figure 6.4: Comparison of effective parabolic constant, $K_p(eff)$ , as a function of steel Mn content and bath Al content.	129
Figure 6.5: Calculation of Fe-Al interfacial layer and short-circuit diffusion paths areas for the 1.4Mn steel galvanized in a 0.20 wt% dissolved Al bath for reaction times of: (a,b) 2.20s and (c,d) 7.68s. Yellow= Fe-Al interfacial layer and black=short circuit diffusion paths.	131
Figure 6.6: Comparison of Fe-Al interfacial layer openness for different Mn-containing steels for the (a) 0.20 wt% and (b) 0.30 wt% dissolved Al baths.	133
Figure 6.7: Computation of $K_p$ values from interfacial layer growth data for different Mn-containing steels for the (a) 0.20 wt% and (b) 0.30 wt% dissolved Al baths.	137
Figure 6.8: Experimental data of interfacial layer Al uptake as a function of reaction time and steel Mn content for (a) 0.20 wt% and (b) 0.30 wt% dissolved Al baths shown with modelling results (data points and lines are experimental and model results, respectively).	139

## LIST OF TABLES

Table 2.1: Characteristics of Fe-Zn and Fe-Al intermetallic compounds (Guttman 1994)	19
Table 4.1: Chemical composition of experimental steels (wt. %)	53
Table 4.2: Experimental parameters	60
Table 4.3: Reaction time calculation	64
Table 5.1: XPS identification of steel surface constituents (after 9 nm sputtering)	75
Table 5.2: Effect of steel Mn content on FWHM MnO thickness and area percentage oxide coverage	75
Table 5.3: TEM-EDX point analyses for the 1.4Mn steel corresponding to the points indicated in Figure 5.13a (atomic%)	92
Table 5.4: TEM-EDX point analysis of the 2.5Mn and 3.0Mn steels corresponding to the points indicated in Figure 5.14a through Figure 5.17a (atomic%)	97
Table 5.5: Growth rate equation (5.1) parameters for interfacial layer in 0.20 wt% Al bath	100
Table 5.6: TEM-EDX point analysis of the 1.4Mn and 2.5Mn steels corresponding to the points indicated in Figure 5.24a through Figure 5.26a (atomic%)	111
Table 5.7: Growth rate equation (5.1) parameters for the interfacial layer in 0.30 wt% Al bath	113
Table 6.1: Effective parabolic constant values for interfacial layer growth (equation (6.9))	130
Table 6.2: Fe-Al interfacial layer openness constant values	133
Table 6.3: Values for interfacial layer growth model (equations (6.13) through (6.15))	138



# 1 INTRODUCTION

Advanced high strength steels (AHSS) play an important role in reducing the weight of automobiles through the use of smaller cross-sections in load-bearing and crash-critical components (Mintz 2001, Bode et al. 2004). Among this class of AHSS are the manganese-containing dual phase (DP) steels. DP steels are strong candidates for automotive industry to produce lighter weight, fuel efficient vehicles without sacrificing safety due to their excellent combination of high strength, formability and relatively low price. DP steels have a two phase microstructure which consists of a soft ferrite matrix and hard martensite. This microstructure enables DP steels to achieve the desired mechanical properties.

However, in order to ensure long-term performance and meet consumer expectations for product life, any DP steels used in exposed applications must be protected from corrosion. Continuous hot dip galvanizing is the most cost effective and industrially relevant means of protecting DP steels, but the alloying elements essential to obtaining the desired microstructure and mechanical properties (Mintz 2001) can lead to the formation of oxides on the surface during the annealing stage; in fact, the currently used industrial CGL annealing atmospheres cannot reduce surface Mn oxide(s). As a result, reactive wetting by the liquid Zn(Al,Fe) bath during galvanizing and the formation of a well developed interfacial reaction layer at the coating/substrate interface can be

prevented, resulting in poor zinc coating adherence and formability. The interfacial or “inhibition” layer is a thin layer of Fe-Al intermetallic phase(s) which forms very rapidly at the liquid zinc/steel substrate interface through the addition of small amounts of Al (0.16 to 0.20 wt%) to the zinc bath. This layer subsequently hinders or “inhibits” the formation of undesirable brittle Fe-Zn intermetallic compounds and enhances the adhesion and formability of zinc coatings.

However, despite the presence of surface Mn oxides formed during annealing prior to dipping, good reactive wetting and a well-formed Fe-Al interfacial layer has been observed for high Mn DP steels. Khondker et al. (2007) have proposed the in situ aluminothermic reduction of surface manganese oxides by the bath dissolved Al as a partial explanation for the observed good reactive wetting, where this reaction will allow the substrate metallic Fe to be accessible for the formation of the desired Fe-Al interfacial layer. More recently, Kavitha and McDermid (2012) verified that the reaction kinetics are linear and proceed by a dissolution mechanism. However, this reaction consumes bath dissolved Al, also needed to form the desired Fe-Al interfacial layer.

Based on the preceding discussion, it is obvious that understanding the interfacial layer formation mechanism, kinetics, and composition is very important in that it leads to better management of the galvanizing process and higher quality products. However, fundamental knowledge concerning this reaction is scarce and there is virtually no information on how this process functions in the case of AHSS. For example, we have

some knowledge concerning the role of reaction time, dissolved bath Al content and temperature on the interfacial layer reaction for simple low C or interstitial free steels (Guttman 1994, Toussaint et al. 1998, Baril et al. 1999, Chen et al. 2008), but have virtually no knowledge concerning the role of alloying elements or their surface oxides on the kinetics and microstructural development of the Fe-Al interfacial layer.

This thesis undertakes the investigation of the formation kinetics and microstructural evolution of the Fe-Al interfacial layer as a function of steel Mn content and bath dissolved Al content. Mn selective oxidation of a variety of Mn-containing steel surfaces during annealing prior to hot-dip galvanizing and Fe-Al interfacial layer development as a function of alloy Mn content, reaction time and dissolved Al bath content will be discussed in Chapter 5. Interfacial layer formation mechanism as a function of the above experimental variables will be discussed in Chapter 6. In particular, the effect of the MnO layer arising from selective oxidation during annealing on the formation of the Fe-Al interfacial layer during continuous hot-dip galvanizing will be explored.

## **2 LITERATURE REVIEW**

This chapter will focus on the continuous hot-dip galvanizing process and the influence of process parameters on interfacial layer characteristics. The effect of steel alloying elements on interfacial layer development, particularly Mn, will be discussed.

### **2.1 Dual phase steels**

Manganese-containing dual phase (DP) steels are amongst the class of advanced high strength steels (AHSS) which have attracted automotive industry attention due to their excellent combination of high strength, good formability and relatively low price. In fact, AHSS are strong candidate materials which are critical to allowing the automotive industry to produce lighter weight, fuel efficient vehicles without compromising safety. Dual phase steels have a two phase microstructure which consists of a soft ferrite matrix and dispersed islands of a hard martensite. This microstructure enables dual phase steels to achieve the desired mechanical properties such as continuous yielding behaviour, high yield strength (YS) to ultimate tensile strength (UTS) ratio and high rate of work hardening (Messien et al. 1981, Liewellyn and Hillis 1996, Mintz 2001, Bode et al. 2004). DP steel properties are dependent on alloying element additions such as Mn, in which Mn plays a significant role as an austenite ( $\gamma$ ) stabilizer (thereby improving hardenability) and solid-solution strengthener (Tanaka et al. 1979, Messien et al. 1981, Liewellyn and Hillis

1996, Mintz 2001) and which also allow alloy C levels to be kept within a range to allow for good weldability.

To be used in automotive exposed parts, corrosion protection of AHSS is essential and continuous hot-dip galvanizing is amongst the most cost effective and industrially relevant means of accomplishing this objective. The following section will discuss the continuous hot-dip galvanizing process.

## **2.2 Continuous hot-dip galvanizing**

Galvanizing is a leading technique in the production of corrosion resistant steels, as zinc coatings provide both barrier and galvanic protection against corrosive environments. Amongst several galvanizing methods, the continuous hot-dip galvanizing of steel sheet has several advantages; for example, the process is cost-effective, is capable of high tonnage throughputs and the coatings produced can be used in highly demanding exposed applications due to their high quality finish, uniformity and paintability. The continuous hot-dip galvanizing process consists of a series of steps (Figure 2.1), as follows:

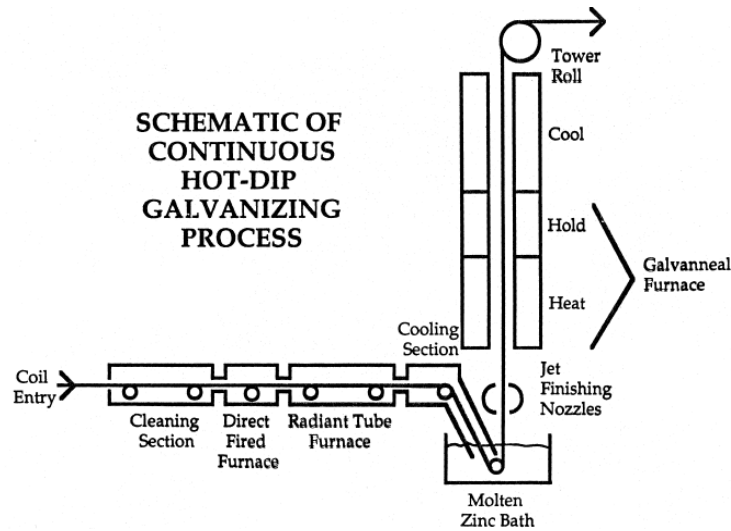


Figure 2.1: Schematic of the continuous hot-dip galvanizing process (Marder 2000).

1. Steel coils of steel are welded end-to-end to form a continuous strip.
2. The steel strip surface is cleaned using an alkali solution and mechanical brushing to removing oils, dirt, and loose oxides. In more modern lines, electrolytic cleaning is sometimes incorporated into the cleaning section.
3. The steel is annealed in a  $N_2/H_2$  reducing atmosphere with a controlled dew point (i.e. fixed  $p_{H_2O}$ ) to obtain a metallic Fe surface and the desired mechanical properties and substrate microstructure. As a result, the annealing temperature used is dependent on the type of steel being coated. A typical process atmosphere dew point is in the range of  $-10^\circ\text{C}$  to  $-30^\circ\text{C}$ . This oxide reduction step is very critical to obtain good reactive wetting of the steel surface by the liquid Zn bath.

4. The strip is cooled to the liquid zinc bath temperature (typically 460°C).
5. The zinc coating is applied by immersing the steel strip into the molten Zn (Al,Fe) bath. It is essential that the Zn bath reactively wet the steel strip during this stage in order for a high-quality, adherent coating be produced. This stage of the galvanizing process will be the focus of this thesis. Typical galvanizing bath dissolved Al contents and temperatures range from 0.15 to 0.25 wt. % and 450°C to 470°C, respectively.
6. Excess coating metal is removed by gas jet wiping (air or nitrogen) to obtain the desired coating thickness.
7. The steel is cooled and the zinc coating solidifies upon exiting the zinc bath by natural convection.
8. In some cases the steel is annealed to develop a fully alloyed coating of Fe-Zn intermetallics prior to cooling the coated steel strip. This step is known as galvannealing and will not be discussed in the present study.
9. Finishing: Roller levelling, temper rolling, pre-phosphating, oiling, cutting and recoiling.

### **2.3 Selective oxidation**

Selective oxidation, within the context of the present work, is the process by which the less noble elements in a steel are oxidized in preference to iron (where Fe is the

dominant compositional element and comprises the matrix phase). As mentioned above, in the continuous galvanizing process the steel sheets are heat treated in a  $N_2/H_2$  atmosphere which is reducing with respect to Fe prior to dipping into the zinc bath in order to obtain the desired microstructure and to reduce any surface iron oxides. However, the alloying elements manganese (Mn) and silicon (Si), commonly used in advanced high strength steel (AHSS) compositions, tend to be oxidized during annealing, as the equilibrium partial pressure of oxygen for oxidation of these elements is significantly lower than that of typical industrial annealing atmospheres (Olefjord et al. 1980, Kofstad 1988, Maitaine et al. 1992, Grabke et al. 1995, Birks et al. 2006, Shastry et al. 2007, Thorning et al. 2007). The presence of oxides such as MnO and  $SiO_2$  can result in poor reactive wetting by the zinc bath and therefore poor adherence of the zinc coating (Mahieu et al. 2001, Drillet et al. 2004, Mahieu et al. 2004).

### 2.3.1 Selective oxidation during annealing

The process atmosphere in the continuous galvanizing line (CGL) is composed of a  $N_2-H_2$  mixture with a controlled dew point ( $dp$ ). Dew point is defined as the temperature,  $T_{dp}$ , at which gaseous water at a fixed partial pressure,  $p_{H_2O}$ , condenses. In another word, at a defined  $T_{dp}$  reaction (2.1) is in equilibrium.

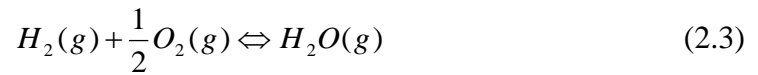


The partial pressure of  $H_2O(g)$  can be determined from equation (2.2):

$$\Delta G_{(2.1)}^o = -RT_{dp} \ln \left[ \frac{P_{H_2O(g)}}{a_{H_2O(l)}} \right] \quad (2.2)$$

where  $\Delta G$  is the standard Gibbs free energy change and  $R$  is the universal gas constant. Since the annealing conditions under discussion are at high temperature and atmospheric pressure, it can be assumed that the gases behave ideally. Also,  $H_2O(l)$  is assumed to be a pure condensed species (*i.e.*  $a_{H_2O(l)} = 1$ ).

Since the CGL annealing atmosphere consists of fixed partial pressures of hydrogen ( $H_2$ ) and water vapour, the partial pressure of oxygen is fixed at the annealing temperature,  $T_A$ , and can be specified from reaction (2.3) and using equation (2.4).



$$\Delta G_{(2.3)}^o = -RT_A \ln \left[ \frac{P_{H_2O(g)}}{P_{H_2(g)}P_{O_2(g)}^{1/2}} \right] \quad (2.4)$$

Reaction (2.5) shows the general formula for the oxidation of an alloying element,  $M$ , to its stoichiometric oxide,  $M_xO_y$ , by a  $O_2$ -containing atmosphere.



$$\Delta G_{(2.5)}^o = -RT_A \ln \left[ \frac{a_{M_xO_y}^{1/y}}{a_M^{x/y} P_{O_2(g)}^{1/2}} \right] \quad (2.6)$$

Taking the activity of the pure condensed oxide as unity ( $a_{M_xO_y}=1$ ) and assuming the activity of the species being oxidized/reduced in the alloy ( $a_M$ ) is known, the critical oxidation potential above which the oxide is stable and below which the oxide is reduced can be evaluated by equation (2.6). The oxygen partial pressure as a function of annealing temperature and alloy Mn activity for a N<sub>2</sub>-5%H<sub>2</sub> atmosphere is shown in Figure 2.2. The activities of 0.002 and 0.03 were chosen as they are approximately the minimum and maximum mole fraction of Mn in the experimental alloys and assuming an ideal solution, the activities of Mn in the experimental alloys are estimated to be between 0.002 and 0.03.

Typically, a N<sub>2</sub>-5%H<sub>2</sub> and -30°C dew point atmosphere are used for annealing in industrial continuous galvanizing lines and are used in the present study. It can be predicted that in the temperature range of 400 °C to 900 °C and at dew point of -30°C, iron oxides are reduced to metallic iron; however, Mn would be oxidized. In addition, by increasing the alloying element concentration the equilibrium  $pO_2$  needed for oxidation decreases.

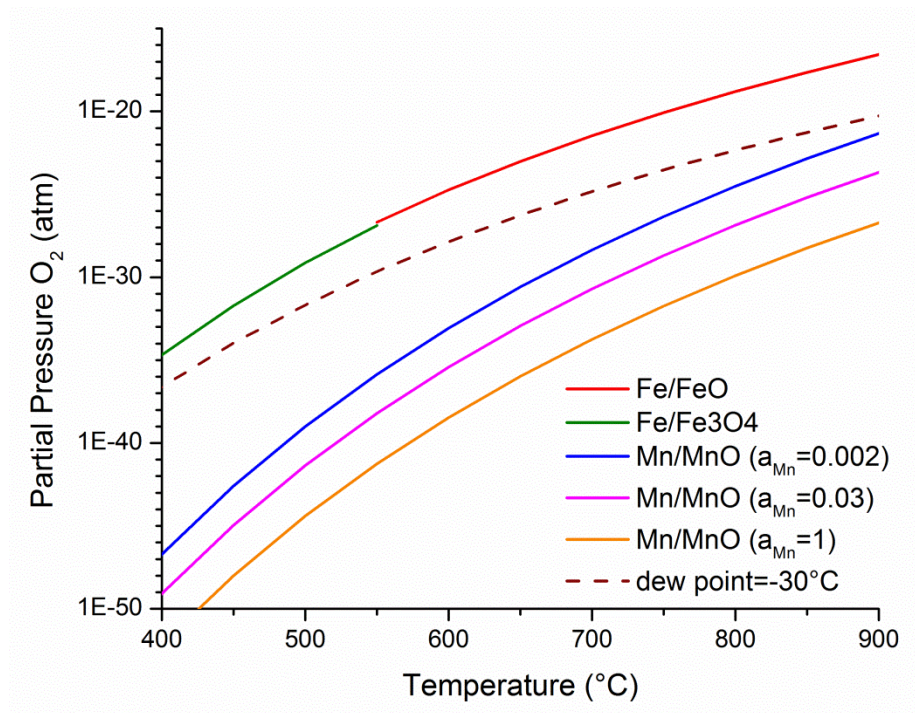


Figure 2.2: Thermodynamic stability of Fe and Mn oxides with respect to annealing temperature and oxygen partial pressure for a  $N_2$ -5% $H_2$  atmosphere. The effect of Mn alloy activity on the Mn/MnO equilibrium is shown (Fine and Geiger 1979).

### 2.3.1.1 The transition between internal and external oxidation

There are two types of selective oxidation: internal and external. In internal oxidation, the oxide particles precipitate in the alloy matrix beneath the free surface and in external oxidation an oxide film forms on the surface of the substrate. The oxidation mode is a function of temperature, partial pressure of oxygen of the annealing atmosphere and the concentration of the alloying element. It should be mentioned that during galvanizing, it is important to minimize the external surface oxides by promoting

subsurface oxides formation in order to improve the reactive wetting (Mahieu et al. 2001, Vanden Eynde et al. 2004, Mahieu et al. 2004).

The criterion for the transition between internal and external oxidation was first developed by Wagner (1959) for a binary alloy single crystal. According to Wagner's theory (1959), during isothermal annealing under a constant partial pressure of oxygen the internal oxidation of an element  $X$  in a binary  $M$ - $X$  alloy occurs when the mole fraction of element  $X$  ( $N_X$ ) is less than a critical value:

$$N_{X,crit}^0 = \left[ \frac{\pi g^* V N_O^s D_O}{2n V_{XO_n} D_X} \right]^{\frac{1}{2}} \quad (2.7)$$

where  $N_O^s$  is the molar fraction of dissolved oxygen at the surface,  $V$  the alloy molar volume,  $V_{XO_n}$  the molar volume of oxide  $XO_n$ ,  $n$  the stoichiometric ratio between the oxygen and metal atoms in the oxide,  $g^*$  the critical volume fraction of participated oxides which leads to blockage of all inward diffusion of oxygen and was determined to be 0.3 by Rapp (1965) and  $D_O$  the bulk diffusion coefficient for oxygen, and  $D_X$  the bulk diffusion coefficient for the alloying element  $X$ . The diffusivities of oxygen and alloying elements  $X$  can be computed using equations (2.8) and (2.9), respectively.

$$D_O = D_O' \exp(-Q_O / RT) \quad (2.8)$$

$$D_X = D_X' \exp(-Q_X / RT) \quad (2.9)$$

where  $Q_O$  and  $Q_X$  are respectively the activation energies for diffusion of oxygen and alloying elements X (J/mol),  $D'_O$  and  $D'_X$  are their respective pre-exponential factors ( $\text{cm}^2/\text{s}$ ),  $T$  is the absolute temperature (K) and  $R$  is the universal gas constant.

According to the Wagner's model (1959), the selective oxidation mode (internal or external) is dependent on the competition between the inward oxygen flow and the outward alloying element flow. When the flux of oxygen atoms through the substrate is greater than the flux of alloying elements to the surface, internal oxidation occurs and continues until a compact layer of oxides obstructs further flow of oxygen into the steel. By contrast, if the flux of alloying elements to the surface is greater than the inward flux of oxygen atoms, external oxidation occurs (Wagner 1959, Maigne et al. 1992, Grabke et al. 1995, Vanden Eynde et al. 2002, Vanden Eynde et al. 2003, Cvijovic et al. 2006, Shastry et al. 2007, Khondker et al. 2007, Thorning and Sridhar 2007).

It should be noted that equation (2.7) is for a binary single crystal, so the grain boundary diffusion normally found in polycrystalline solids was neglected. Therefore, several extensions to the original Wagner's model (1959) applicable to Fe based alloys have been developed (Maigne et al. 1992, Grabke et al. 1995, Shastry et al. 2007).

Maigne et al. (1992) developed Wagner's model (1959) further to account for grain boundary oxidation by assuming that the grain boundary diffusion activation energy is half its value for lattice diffusion as follows:

$$N_{X,crit.GB}^0 = \left[ \frac{\pi g^* V N_o^s D_o' \exp(-Q_o / 2RT)}{2n V_{XO_n} D_X' \exp(-Q_X / 2RT)} \right]^{\frac{1}{2}} \quad (2.10)$$

In the case of multi-component alloys, Grabke et al. (1995) modified Wagner's model by assuming an additive effect of the oxidizable alloying elements (equation 2.11). External oxidation will occur when the inequality in equation (2.11) is satisfied.

$$\sum_X N_X^{(0)} [nD_X V_{XO_n}]^{\frac{1}{2}} > \left[ \frac{\pi g^*}{2} V D_o N_o^{(S)} \right]^{\frac{1}{2}} \quad (2.11)$$

Furthermore, Shastry et al. (2007) modified Wagner's model for two-phase steels consist of ferrite and austenite (equation 2.12). In equation (2.12)  $f$  is the volume fraction of austenite and  $a_X$  the alloying elements activity. If the left side of equation (2.12) is greater than the right side (i.e. the inequality is satisfied) then external oxidation will occur.

$$f \left( \sum_X a_X [nD_X V_{XO_n}]^{\frac{1}{2}} \right)_{\gamma} + (1-f) \left( \sum_X a_X [nD_X V_{XO_n}]^{\frac{1}{2}} \right)_{\alpha} > \left[ \frac{\pi g^*}{2} V D_o N_o^{(S)} \right]^{\frac{1}{2}} \quad (2.12)$$

It should be noted that the complex oxides formation and interactions between the elements that affects their diffusivities are not considered in these models.

### 2.3.2 Selective oxidation of Mn-containing steels

As was discussed in §2.3.1, annealing of advanced high strength steels during continuous galvanizing can result in significant selective oxidation and poor reactive wetting during galvanizing. A selection of results from the literature will be presented in

this section providing an overview of the effect of Mn alloying element and process atmospheres on the oxidation of Mn-containing steels. It should be mentioned that many researchers have used different parameters such as volume% H<sub>2</sub>, dew point and  $p_{H_2O}/p_{H_2}$  ratio to characterize the annealing atmosphere oxidation potentials. However, the more accurate parameter representative of the atmosphere oxidation potential is partial pressure of oxygen ( $p_{O_2}$ ). Thus,  $p_{O_2}$  is provided in the following discussion.

Mn selective oxidation in the form of MnO for Fe-Mn steels has been reported by a number of authors (Loison et al. 2001, Vanden Eynde et al. 2003, Khondker et al 2007, Meguerian 2007, Li et al. 2011, Kavitha et al. 2012, Song et al. 2012, Sagl et al. 2013). The addition of other AHSS alloying elements such as Si and Al has also been shown to result in the formation of various oxides and spinel-type oxides such as SiO<sub>2</sub>, Al<sub>2</sub>O<sub>3</sub>, Mn<sub>2</sub>SiO<sub>4</sub>, MnSiO<sub>3</sub>, and MnAl<sub>2</sub>O<sub>4</sub> as well as MnO (Drillet et al. 2001 and 2004, Mahieu et al. 2001 and 2004, Cvijovic et al. 2006, Swaminathan et al. 2007, Bellhouse et al. 2007, Bellhouse et al. 2008, Li et al. 2007, Wang et al. 2009, Gong et al. 2008, Gong et al. 2009, Ollivier-Leduc et al. 2010, Bellhouse and McDermid 2010, 2011 and 2012, Kim et al. 2012, Gong et al. 2011, Cho et al. 2013).

The effect of annealing atmosphere dew point on Mn selective oxidation was studied for an Fe-1.5wt%Mn steel annealed in a N<sub>2</sub>-5%H<sub>2</sub> atmosphere at 800°C for 60s by Vanden Eynde et al. (2003). MnO was detected by XPS for all dew points from -60 to 0 °C (i.e.  $7 \times 10^{-26} \leq p_{O_2} \leq 6.5 \times 10^{-21}$  atm). The lowest surface Mn segregation and finest

MnO nodules were observed for the -60 °C dew point atmosphere, while the -30 °C dew point atmosphere ( $4.5 \times 10^{-23}$  atm  $pO_2$ ) showed the highest surface Mn enrichment and almost full surface coverage of MnO. Also, they reported a transition from external to internal oxidation by increasing the dew point due to higher inward oxygen flow.

The same general trends were reported by Khondker et al. (2007). They studied the influence of the annealing atmosphere  $pH_2O/pH_2$  ratio from 0.00211 to 0.14180 (i.e.  $3 \times 10^{-24} \leq pO_2 \leq 10^{-20}$  atm) on the selective oxidation of a Fe-2wt%Mn alloy at 800 °C by glow discharge optical emission spectrometer (GDOES). They considered O and Mn diffusion for both ferrite and austenite and their grain boundaries to predict the Mn selective oxidation mode. A significant Mn selective oxidation in the form of MnO was observed for all experimental annealing atmospheres. A transition was reported from external to internal oxidation for  $pO_2$  higher than  $8 \times 10^{-22}$  atm. No information regarding the oxide morphology was provided.

Li et al. (2011) investigated the influence of annealing duration on MnO morphology and distribution for an Fe-1.9wt%Mn dual phase steel in an annealing atmosphere of N<sub>2</sub>-5%H<sub>2</sub>, -55°C dew point and 820 °C annealing temperature ( $6.4 \times 10^{-25}$  atm  $pO_2$ ) using scanning electron microscopy (SEM). They reported that by increasing the annealing time from 45s to 120s, the surface MnO thickness increased from 80nm to 140 nm; also, the oxide morphology changed from nodular to film-like.

Kim et al. (2012) studied the influence of steel Mn content (1.8, 2.2 and 2.6 wt% Mn) on Mn selective oxidation by SEM. Annealing was conducted at 800 °C in a reducing atmosphere of N<sub>2</sub>-15%H<sub>2</sub> at a dew point of -60°C ( $7.5 \times 10^{-27}$  atm  $pO_2$ ). They reported that the oxide nodule size and the surface oxide coverage increased by increasing the alloy Mn content; however, no significant change in oxide morphology was observed.

As shown by these results, normal CGL annealing atmosphere promotes Mn selective oxidation in the form of MnO for Mn-containing steels. Also, atmosphere oxidation potential, annealing time and substrate Mn content strongly affect the surface MnO density, morphology and thickness which are all important factors in determining the reactive wetting behaviour during galvanizing as will be discussed in detail in §2.4.3.3.

## **2.4 Fe-Al interfacial layer**

Galvanizing in a pure zinc bath will result in the formation of a coating with several layers of Fe- Zn intermetallics comprising gamma ( $\Gamma$ -Fe<sub>3</sub>Zn<sub>10</sub>), delta ( $\delta$ -FeZn<sub>10</sub>), zeta ( $\zeta$ -FeZn<sub>13</sub>), and metallic Zn, as shown in Figure 2.3 (Jordan and Marder 1997). These intermetallics are hard and brittle and their presence leads to the formation of cracks at the coating/substrate interface during substrate deformation and poor coating adhesion.

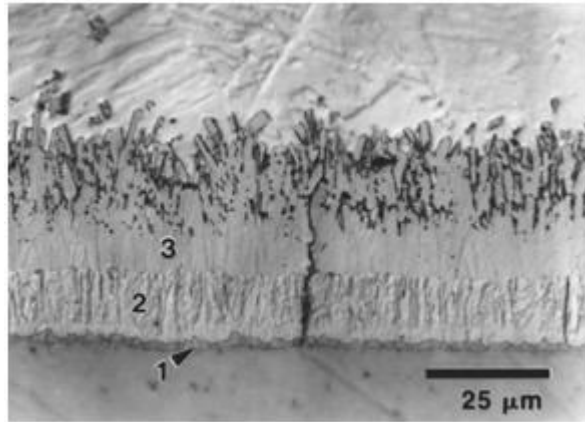


Figure 2.3: Microstructure of Zn coating formed after 300s immersion in a 450°C, pure zinc bath: 1 ( $\Gamma$ -Fe<sub>3</sub>Zn<sub>8</sub>), 2 ( $\delta$ -FeZn<sub>10</sub>) and 3 ( $\zeta$ -FeZn<sub>13</sub>) (Jordan and Marder 1997).

It is common practice to deliberately add small amount of aluminium (0.15-0.25 wt% Al) to the continuous hot-dip galvanizing bath to improve coating ductility and adhesion through the rapid formation of a thin interfacial layer of Fe-Al intermetallic phase(s) between the liquid metallic zinc coating overlay and steel substrate. Since the Gibbs free energy of formation of the Fe-Al intermetallic phases are more negative than that of the Fe-Zn intermetallic phases (Table 2.1), the thermodynamic driving force for the formation of Fe-Al intermetallics is considerably higher than that for the formation of Fe-Zn intermetallics. As a result, the formation of brittle Fe-Zn intermetallic between the zinc coating overlay and steel substrate is temporarily hindered or “inhibited” by the formation of the Fe-Al intermetallic layer, which acts as a diffusion barrier between iron

and zinc. For this reason, the Fe-Al interfacial layer is usually referred to as the inhibition layer by the industry and in the literature (Guttman 1994, Marder 2000).

However, the Fe-Al intermetallic layer cannot permanently prevent the formation of Fe-Zn intermetallic compounds and after prolonged exposure to the liquid zinc bath inhibition breakdown will occur by formation of outbursts of Fe-Zn intermetallics at the steel/coating interface.

Table 2.1: Characteristics of Fe-Zn and Fe-Al intermetallic compounds (Guttman 1994)

Phase	Crystal Lattice	$\Delta H$ (kJ/mol)	$\Delta G(450^\circ\text{C})$ (kJ/mol)
$\zeta$ -FeZn <sub>13</sub>	Monoclinic	-11.7	-2.8
$\delta$ -FeZn <sub>10</sub>	Hexagonal	-11.5	-3.5
$\Gamma 1$ - Fe <sub>5</sub> Zn <sub>25</sub>	FCC	-11.7	-4.1
$\Gamma$ - Fe <sub>3</sub> Zn <sub>10</sub>	BCC	-10.9	-4.2
$\theta$ - FeAl <sub>3</sub>	Monoclinic	-35.1	-30
$\eta$ - Fe <sub>2</sub> Al <sub>5</sub>	Orthorhombic	-34.6	-32
$\zeta$ - FeAl <sub>2</sub>	Rhombohedral		-31
$\alpha$ -FeAl	BCC		-32

Studying the influence of bath dissolved Al (known as effective Al in industry) in the zinc bath and the phase transformations that happen in the bath are important to control the microstructure and properties of galvanized coatings. Fe is present in the Zn bath due to Fe dissolution from the steel strip during dipping as  $\alpha$ -Fe is not in equilibrium with the Zn bath (Guttman 1994). Figure 2.4 shows the Zn-rich corner of the Zn-Al-Fe phase

diagram at 460°C per McDermid et al. 2007. It can be seen that Al and Fe have limited solubility in liquid Zn and by addition of Al to the bath the Fe solubility decreases. On the other hand, there is a higher metastable iron solubility in the vicinity of the steel substrate (Figure 2.5), resulting in the continuous Fe dissolution and dross precipitation and, therefore creating a local supersaturation of Fe in the vicinity of the steel substrate. The Fe supersaturation leads to the nucleation of Fe-Al or Fe-Zn intermetallic compound on the steel surface according to the Al content of the bath, as the equilibrium configuration of the zinc bath has to be obeyed.

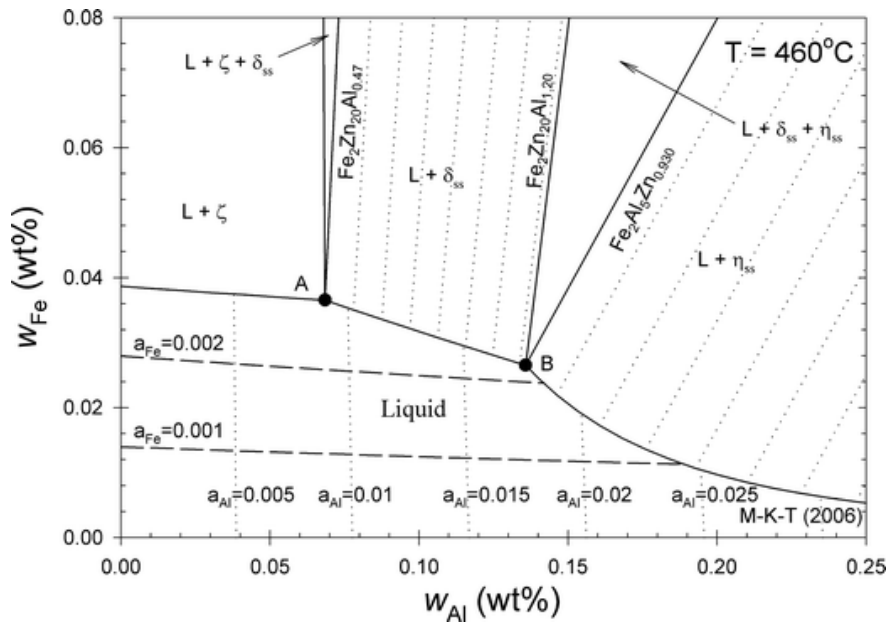


Figure 2.4: Zn rich corner of the Zn-Al-Fe phase diagram; L is liquid,  $\zeta$  is  $\text{FeZn}_{13}$ ,  $\delta$  is  $\text{FeZn}_{10}$  and  $\eta$  is  $\text{Fe}_2\text{Al}_5\text{Zn}_x$ . Indicated on the phase diagram are isoactivity lines for Al (with respect to pure solid Al) and Fe (with respect to pure solid  $\alpha$ -Fe) in the liquid phase (McDermid et al. 2007).

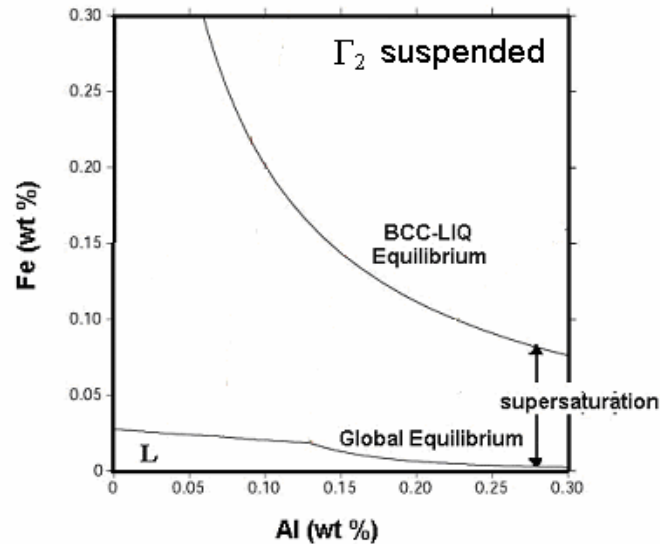


Figure 2.5: Metastable versus equilibrium configuration for the Zn-rich corner of the Zn-Al-Fe at 450°C (Nakano 2006).

#### 2.4.1 Interfacial layer composition and morphology

There is some disagreement among researchers concerning the composition of the interfacial layer; in fact, several different results have been obtained for the composition of the interfacial layer due to variations in experimental technique such as X-ray diffraction (XRD), transmission electron microscopy (TEM), scanning electron microscopes/energy-dispersive X-ray spectroscopy (SEM/EDX), electron backscatter diffraction (EBSD) and auger electron spectroscopy (AES). Most researchers (Harvey et al. 1973, Faderl et al. 1992, Guttman et al. 1995, Lin et al. 1995, Morimoto et al. 1997, Hertveldt et al. 1998, Baril and L'Esperance 1999, Chen et al. 2008, Wang et al. 2010,

Sagl et al. 2013) have found that the interfacial layer is a Zn-bearing  $\text{Fe}_2\text{Al}_5$  intermetallic ( $\text{Fe}_2\text{Al}_{5-x}\text{Zn}_x$   $0 \leq x \leq 1$ ). However, it has been reported by some researchers (Lin et al. 1995, Morimoto et al. 1997, McDevitt et al. 1997, Hertveldt et al. 1998, Chen et al. 2008, Bellhouse and McDermid 2008) that the Fe-Al interfacial layer is composed of both  $\text{Fe}_2\text{Al}_5$  and  $\text{FeAl}_3$ , particularly in the initial stages of the interfacial layer formation (Chen et al. 2008, Bellhouse and McDermid 2008). It should be noted that in the case of advanced high strength steels, selective oxidation products such as  $\text{MnO}$ ,  $\text{SiO}_2$  and  $\text{Mn}_2\text{SiO}_4$  were detected at the Fe-Al interfacial layer (Wang et al. 2009, Bellhouse and McDermid 2010, 2011 and 2012, Song et al. 2012, Sagl et al. 2013). This will be discussed in detail in §2.4.3.3.

The morphology of the Fe-Al interfacial layer is strongly related to the dissolved Al content of the galvanizing bath (Baril and L'Esperance 1999). It has been proposed that the interfacial layer in higher dissolved Al baths ( $> 0.15$  wt%) consists of two sublayers (Figure 2.6). The lower layer, which is in contact with the substrate, is a compact layer of small, roughly equiaxed, closed packed crystals with diameters of the order of tens of nanometers, whereas the upper layer that is in contact with the zinc bath consists of coarser, elongated, non-compact crystals on the order of hundreds of nanometers (Guttmann et al. 1995, Baril and L'Esperance 1999, Marder 2000, Chen et al. 2008).

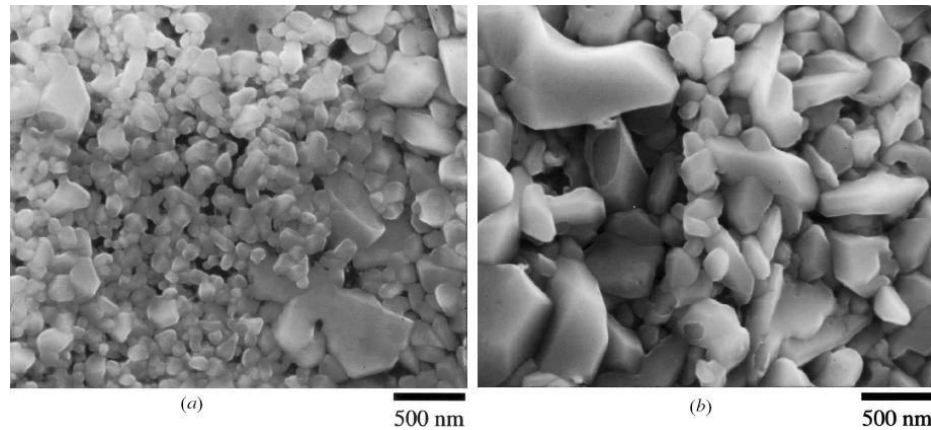


Figure 2.6: Two types of morphology of Fe-Al interfacial layer observed in 0.18 wt% Al bath: a) small equiaxed crystals and b) coarse elongated crystals (Baril and L'Esperance 1999).

However, for lower dissolved Al baths ( $< 0.14$  wt%), the Fe-Al interfacial layer has been observed to have only one layer, but Fe-Zn intermetallic compounds were also observed in the interfacial layer, as shown in Figure 2.7. In fact, the Fe-Al layer forms initially and continues to grow; then, the Fe-Zn phases nucleate and grow by the mechanism of interfacial layer breakdown for longer reaction times (Guttmann 1994, Jordan and Marder 1997, Tang 1998, Baril and L'Esperance 1999, Marder 2000, Chen et al. 2008).

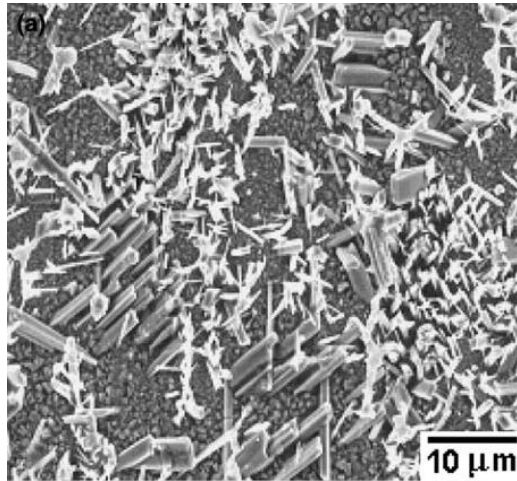


Figure 2.7: Morphology of the interfacial layer for a bath with 0.13 wt% dissolved Al (Chen et al. 2008).

#### 2.4.2 Interfacial layer formation

A full understanding of the formation mechanisms and kinetics of the Fe-Al interfacial layer is still a matter of debate. However, it is generally accepted that the formation of the interfacial layer can be broken into three stages (Guttman 1994, Tang 1995, Toussaint et al. 1998, Marder 2000, Giorgi et al. 2005, Chen et al. 2008, Dutta et al. 2009). In the first stage, Fe is dissolved from the steel strip surface into the liquid zinc as the zinc bath approaches metastable equilibrium with the steel strip. In the second stage, nucleation and lateral growth of the Fe-Al interfacial layer at the interface of the steel substrate and zinc bath occurs and is completed when the surface is fully covered by crystals (Figure 2.8). The third stage is diffusion controlled growth of the interfacial layer, limited by Fe transport from the substrate to the liquid through the existing Fe-Al layer.

These three stages occur in a few seconds. In particular, the first two stages are thought to be completed in significantly less than one second, although these events have yet to be observed experimentally (Guttman 1994, Tang 1995, Toussaint et al. 1998, Marder 2000, Giorgi et al. 2005, Chen et al. 2008, Dutta et al. 2009).

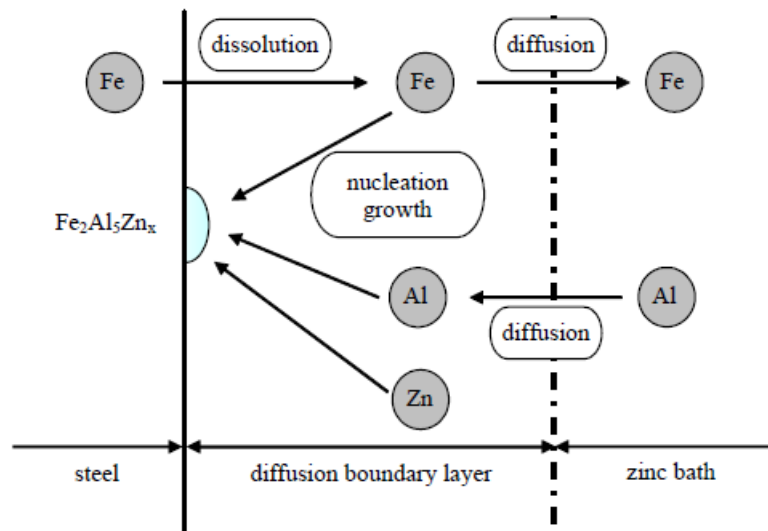
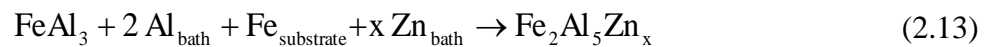


Figure 2.8: Schematic representation of galvanizing reactions (Giorgi et al. 2005).

Chen et al. (2008) proposed that the formation of the interfacial layer for high dissolved Al bath starts with the nucleation of  $\text{FeAl}_3$  on the substrate surface and this layer continues to grow until the surface is completely covered with a layer of small, equiaxed crystals. Simultaneously the  $\text{FeAl}_3$  layer transforms to  $\text{Fe}_2\text{Al}_5\text{Zn}_x$  by a diffusive reaction mechanism as follows:



The  $\text{FeAl}_3$  continues to transform to  $\text{Fe}_2\text{Al}_5\text{Zn}_x$  and grows by diffusion to form the coarse, non-compact outer interfacial layer by diffusion of Fe through the interfacial layer and reaction with dissolved Al and Zn from the bath. This leads to the disappearance of  $\text{FeAl}_3$  and the observed two-layer structure of the  $\text{Fe}_2\text{Al}_5\text{Zn}_x$  interfacial layer (Chen et al. 2008). Figure 2.9 shows a schematic of the above process for interfacial layer formation in a high dissolved Al bath. It is worth noting that at short reaction times and low bath temperatures the interfacial layer only consists of the lower layer with small, equiaxed crystals.

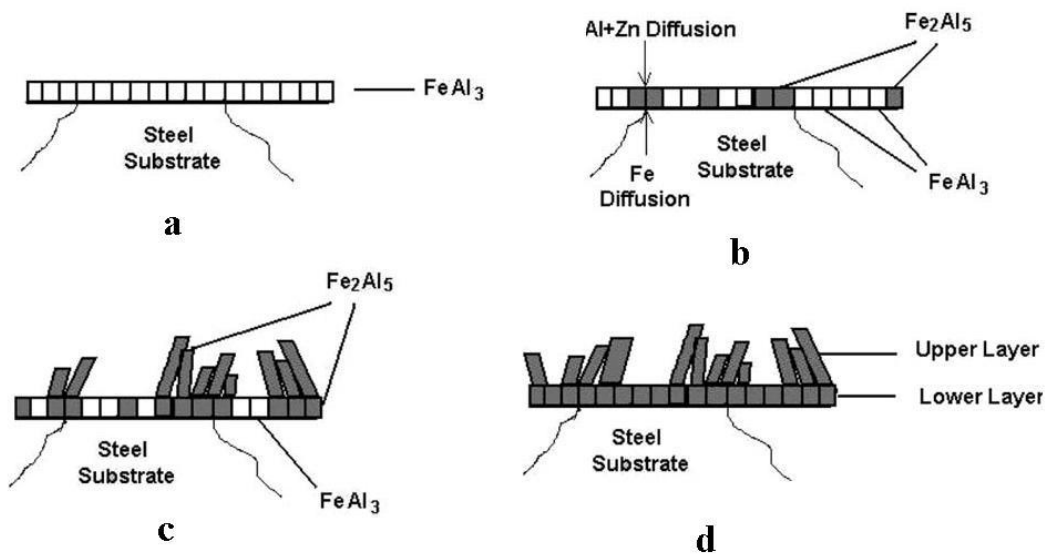


Figure 2.9: Schematic representation of interfacial layer formation on an IF steel surface using a 0.20 wt. % dissolved Al bath (Chen et al. 2008).

For low dissolved Al baths, interfacial layer formation is similar to what stated for the high Al bath, but the microstructure consists of only one discontinuous sublayer which results in the rapid inhibition breakdown and formation of Fe-Zn phases (Inagaki et al. 1995, Kiusalaas et al. 1989, Guttman 1994, Tang 1998, Baril and L'Esperance 1999, Marder 2000, Chen et al. 2008).

### **2.4.3 Parameters influencing interfacial layer formation**

There have been several parameters identified as having a significant influence on the interfacial layer morphology, composition and aluminium uptake. By definition, Al uptake is the weight of aluminium present in the interfacial layer per unit surface area, usually expressed as  $\text{mg/m}^2$ , which generally gives an estimation of the interfacial layer thickness ( $1 \text{ mg/m}^2=0.444\text{nm}$ ) (Faderl et al. 1995, Tang 1995, Toussaint et al. 1998). In the next sections the influence of several important parameters will be discussed: reaction time, dissolved bath Al, substrate Mn content and bath temperature.

#### **2.4.3.1 Reaction time**

As was mentioned in §2.4.2, interfacial layer formation is very rapid, so reaction time is a crucial parameter in determining interfacial layer characteristics. Another time parameter that many researchers have used to evaluate Al uptake by the Fe-Al layer is bath immersion time (i.e. the time the substrate is immersed in the Zn-alloy bath) (Isobe 1992, Morimoto et al. 1997, Baril et al. 1998, Toussaint et al. 1998). However, it has been observed that the dissolved Al content of the zinc overlay is significantly lower than that

of the original Zn bath due to post-dipping diffusion of Al in the liquid overlay before solidification is completed and which leads to further growth of the Fe-Al layer (Faderl et al. 1995, Baril et al. 1998). In another words, Al in the zinc overlay diffuses to the interfacial layer/liquid interface to react with Fe, indicating strongly that interfacial layer growth continues during substrate withdrawal from the zinc bath and subsequent solidification of the coating.

Also, the solidification time can vary strongly with the experimental environment and processing conditions such as bath temperature, strip thickness and cooling rate. For example, the Al uptake value reported by Chen et al. (2008) for a 2s reaction time (i.e. 0.1s immersion time ) is lower than that reported by Toussaint et al. (1998) for a 0.1s immersion time for the same bath Al content and bath temperature, as shown in Figure 2.10. These differences can be attributed to the different cooling rates and, therefore, solidification times, considered by Chen et al (2008). Consequently, in studying the evolution of the interfacial layer, the sum of immersion time and time-temperature adjusted solidification time should be considered as the isothermal reaction time (Chen et al. 2008).

It has been reported that Al uptake in the interfacial layer increases by increasing the reaction time (or immersion time) via diffusion controlled growth of the interfacial layer. In fact, as shown in Figure 2.10, Al uptake occurs very rapidly and the majority of interfacial layer Al uptake occurs within approximately 2s reaction time (about 0.1s

immersion time) (Isobe 1992, Tang 1995, Toussaint et al. 1998, Baril et al. 1998, Chen et al. 2008). In addition, the interfacial layer morphology changes from a compact, finely crystalline layer to a coarser and non-compact morphology by increasing the reaction time (Toussaint et al. 1998, Baril et al. 1998, Chen et al. 2008) (Figure 2.11).

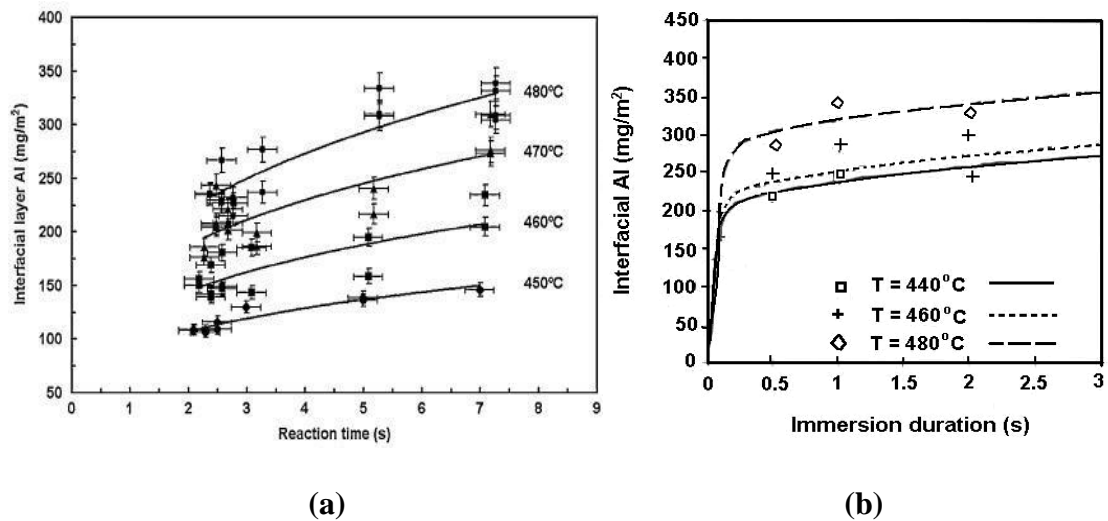


Figure 2.10: Interfacial layer Al uptake vs. (a) reaction time (Chen et al. 2008) and (b) immersion time (Toussaint et al., 1998) for a 0.20 wt% dissolved Al bath as a function of bath temperature.

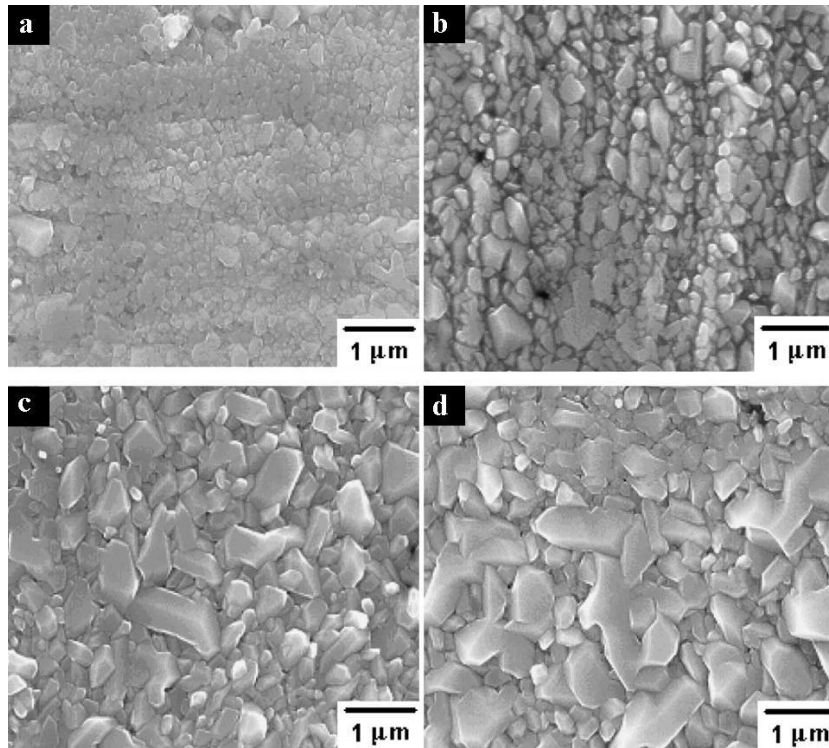


Figure 2.11: Morphology of the interfacial layer for a 0.20 wt% dissolved Al bath at different reaction times: (a) 2.186s, (b) 3.086s, (c) 5.086s, and (d) 7.086s (Chen et al. 2008).

#### 2.4.3.2 Bath dissolved Al

Aluminium exists in two forms in the zinc bath. Some Al is dissolved in the liquid Zn phase (dissolved Al, also known as the effective Al) and the remaining Al is present in the intermetallic particles entrapped in the bath known as dross. The former is a significant parameter that affects interfacial layer formation and characteristics whereas the Al associated with dross particles does not participate in interfacial layer formation. In

fact, although according to the Fe-Al-Zn phase diagram (Figure 2.4) for a dissolved bath Al of less than 0.14 wt%  $\text{Fe}_2\text{Al}_5\text{Zn}_x$  is not the equilibrium intermetallic (McDermid et al. 2007), it has been observed that the Fe-Al interfacial layer forms on the substrate for dissolved bath Al as low as 0.05wt% due to the large driving force for Fe-Al intermetallic formation vs. Fe-Zn intermetallic formation, as shown in Table 2.1 (Guttman 1994, Lin et al. 1995, Tang 1995, Baril et al. 1999).

However, for lower dissolved bath Al contents, the microstructure of the Fe-Al interfacial layer has only a thin discontinuous layer, as the system is Al limited and Fe saturated, which results in the rapid inhibition breakdown and formation of Fe-Zn phases (Inagaki et al. 1995, Kiusalaas et al. 1989, Guttman 1994, Tang 1998, Baril and L'Esperance 1999, Chen et al. 2008).

It has been reported that the Al uptake of the interfacial layer increases by increasing the dissolved Al content of the CGL bath (Faderl et al. 1992, Tang 1995, Toussaint et al. 1998, Baril and L'Esperance 1999, Chen et al. 2008, Wang et al. 2010). Nevertheless, it has been reported by several authors (Isobe 1992, Toussaint et al. 1998, Liu and Tang 2004) that increasing the dissolved bath Al to greater than 0.20 wt% leads to a reduction of interfacial layer Al uptake (Figure 2.12). The possible reason for this observation is that by increasing the bath Al to more than 0.20wt%, the incubation time for interfacial layer nucleation and complete coverage of the substrate decreases and, therefore, less Fe which participates in interfacial layer formation is dissolved from the

substrate (Figure 2.12c). As a result, the system is Fe limited and diffusion controlled growth of the interfacial layer (i.e. Fe diffusion from the substrate through the interfacial layer) starts sooner than that observed for the lower Al baths (Isobe 1992, Toussaint et al. 1998, Liu and Tang 2004). In fact, based on Liu and Tang's model (2004) the maximum interfacial layer Al uptake occurs at a bath dissolved Al of approximately 0.20wt% Al (Figure 2.12c); below this bath dissolved Al the interfacial layer growth is Al limited and above this bath dissolved Al it is Fe limited.

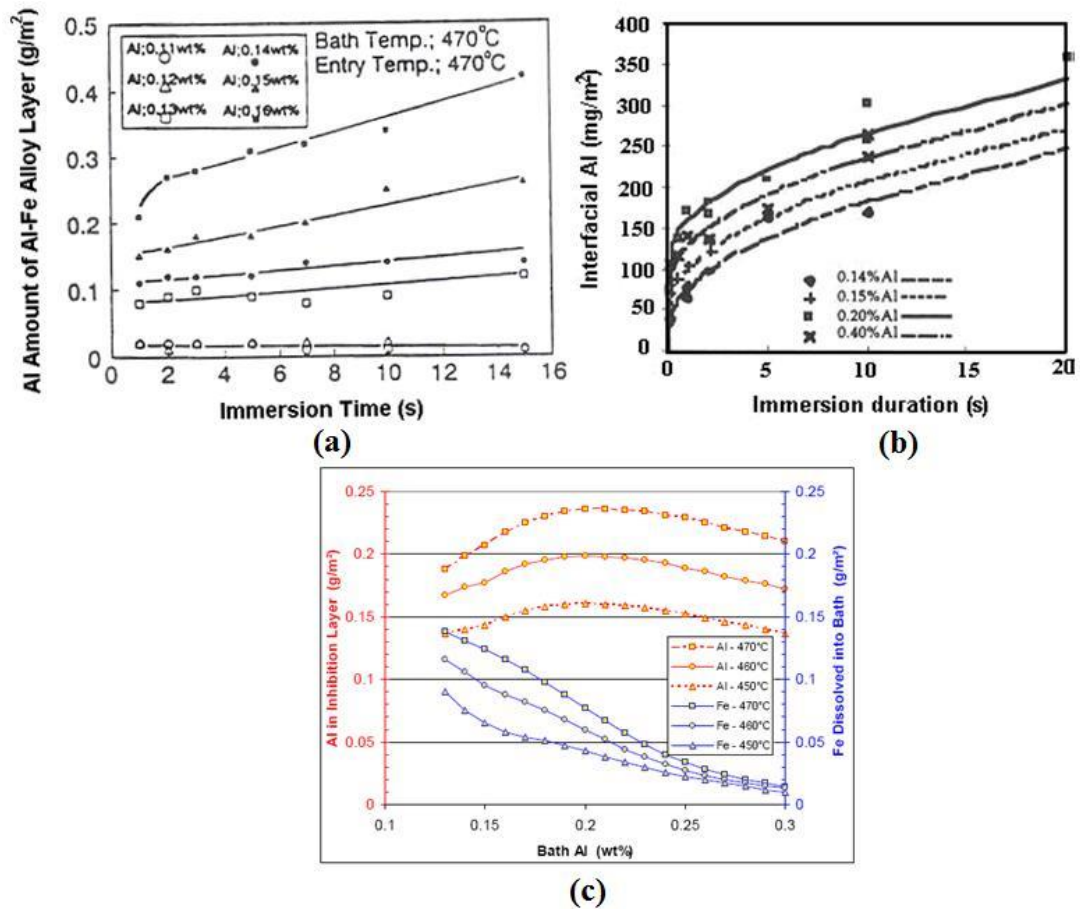
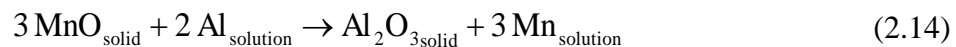


Figure 2.12: Effects of bath dissolved Al on interfacial Al uptake (a) for  $470^\circ\text{C}$  bath and different immersion times (Isobe 1992), (b) for  $460^\circ\text{C}$  bath and different immersion times (Toussaint et al. 1998) and (c) for  $450^\circ\text{C}$ - $470^\circ\text{C}$  baths (Liu and Tang 2004).

### 2.4.3.3 Substrate Mn content

The galvanizability of Mn-containing steels has been studied by a few researchers (Mahieu et al. 2001, Khondker et al. 2007, Bellhouse et al. 2007, Li et al. 2011, Staudte et al. 2011, Alibeigi et al. 2011, Kavitha and McDermid 2012, Sagl et al. 2013, Cho et al.

2013). As discussed in §2.3, Mn is selectively oxidized in conventional continuous galvanizing line process atmospheres. However, despite the presence of surface Mn oxides formed during annealing prior to dipping, good reactive wetting and a well-formed Fe-Al interfacial layer has been observed for Mn-containing steels with as much as 5wt% Mn steels (Khondker et al. 2007, Meguerian 2007, Bellhouse et al. 2007, Wang et al. 2009, Bellhouse and McDermid 2010, 2011 and 2012, Deng et al. 2011, Alibeigi et al. 2011, Li et al. 2011, Sagl et al. 2013). In order to partially explain this seemingly unexpected result, Khondker et al. (2007) proposed the *in situ* aluminothermic reduction of surface MnO by the bath dissolved Al (equation (2.14)) as a mechanism by which the MnO could be removed from the substrate surface, thereby allowing the substrate metallic Fe to be accessible for the formation of the desired Fe-Al interfacial layer. In fact, small quantities of Mn were detected by Dubois (1998) in an industrial Zn bath after galvanizing many coils of Mn containing steels. However, this result does not necessarily support aluminothermic reduction as Mn is also in solid solution in the substrate and will dissolve into the bath with the Fe matrix in the initial stages of contact with the Zn (Al, Fe) bath.



In addition, it has been reported that MnO thickness and morphology are critical in the combined aluminothermic reduction and reactive wetting processes (Bellhouse and

McDermid 2010, 2011 and 2012, Staudte et al. 2011 and Li et al. 2012). They attributed poor wetting to closely spaced and dense oxides morphology or thicker oxide films not being completely reduced by aluminothermic reduction, implying that the MnO reduction kinetics were insufficient in these cases.

Recently, Kavitha and McDermid (2012) verified that the MnO reduction reaction as written in equation (2.14) occurs and that its kinetics are linear, as shown in Figure 2.13 and as characterized by equation (2.15):

$$\Delta x(\text{MnO}) = -49.3 - 9.45t_{\text{reaction}}, t_{\text{reaction}} \geq 1.2\text{s} \quad (2.15)$$

where  $\Delta x$  is the change in MnO layer thickness (nm) and  $t_{\text{reaction}}$  is the reaction time. It can be seen that the MnO dissolution reaction is a strong function of reaction time and has a limited ability to reduce MnO films greater than 100 nm in thickness for normal continuous galvanizing reaction times. In another words, the rate of MnO dissolution is very rapid in its initial stages (i.e. an average of 42 nm (MnO)/s were removed in the first 1.2 s) and the dissolution reaction slows down considerably for reaction times greater than 1.2s (i.e. 9.5 nm (MnO)/s). It should be pointed out that these two different rates for reaction times greater and less than 1.2s may suggest that the aluminothermic reduction reaction is mass-transport limited with respect to Al transport to the bath-oxide interface, further implying that significant Al depletion in the mass transport boundary layer occurring during the initial reaction may limit the subsequent reaction kinetics. This

conclusion is consistent with the observations of thicker or compact nodular surface films resulting in insufficient reactive wetting and bare spot coating defects (Bellhouse and McDermid 2010, 2011 and 2012, Staudte et al. 2011 and Li et al. 2012).

It should be mentioned that Kavitha and McDermid (2012) prevented any Al consumption through Fe-Al interfacial layer formation by producing a continuous, thick layer of MnO on the substrate surface. As a result, the aluminothermic reduction reaction kinetics may change when the dissolved Al bath is consumed through Fe-Al interfacial layer formation as well as aluminothermic reduction.

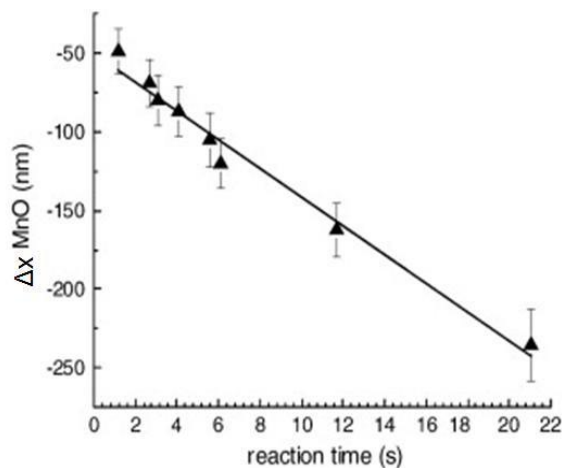


Figure 2.13: Change in MnO layer thickness vs. reaction time for a 460°C 0.20 wt% dissolved Al bath (Kavitha and McDermid 2012).

Kavitha and McDermid (2012), also, detected the resulting  $\text{Al}_2\text{O}_3$  product at the MnO-coating interface as well as high Mn concentration metallic coating adjacent to the reaction front by electron energy loss spectroscopy (EELS), as shown in Figure 2.14.

Similarly, Wang et al. (2009) and Sagl et al. (2013) detected  $\text{Al}_2\text{O}_3$  trapped in the Fe-Al interfacial layer.

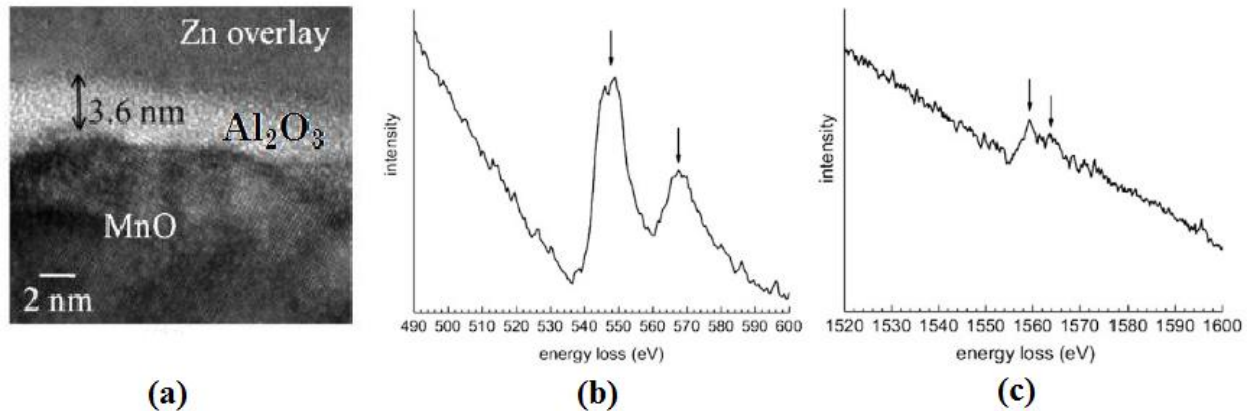


Figure 2.14: (a) HRTEM image of MnO–Zn interface, (b) EELS O–K edge spectra from  $\text{Al}_2\text{O}_3$  at the MnO–Zn interface, and (c) EELS Al–K edge spectra from  $\text{Al}_2\text{O}_3$  at the MnO–Zn interface. Arrows correspond to the characteristic energy loss peaks and configuration for  $\text{Al}_2\text{O}_3$  (Kavitha and McDermid 2012).

Bellhouse and McDermid (2010, 2011 and 2012) and Sagl et al. (2013) demonstrated that surface oxide morphology was significantly altered by interactions with the bath in a way which allowed reactive wetting and the formation of desired  $\text{Fe}_2\text{Al}_5\text{Zn}_x$  interfacial layer between, above or below oxides not chemically removed from the substrate surface by aluminothermic reduction. Moreover, they related good reactive wetting to the cracking and spalling of oxide particles from the surface, allowing liquid infiltration of bath metal between the oxide and substrate. Cracking of the oxide likely occurs as a result of the differences in thermal expansion coefficients between MnO and

Fe, resulting in large stress being imposed on the oxide upon cooling prior dipping to the zinc bath (Kofstad 1988, Birks et al. 2006, Bellhouse and McDermid 2011). Sagl et al. (2013) also stated that surface oxide morphology is crucial for galvanizability rather than oxide chemical composition only. They attributed good reactive wetting to the flaking of oxides from the steel surface induced by the growth of the  $\text{Fe}_2\text{Al}_5\text{Zn}_x$  crystals (Figure 2.15(a,b) and the incorporation of oxides into the interfacial layer (Figure 2.15(c,d)).

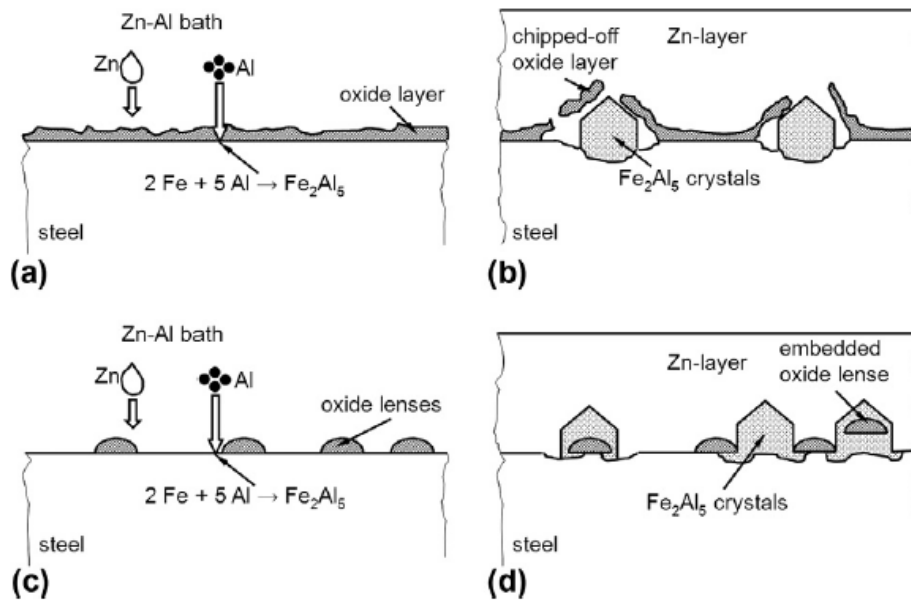


Figure 2.15: Schematic drawing illustrating the Fe-Al interfacial layer formation mechanism in the presence of surface oxides (Sagl et al. 2013).

Moreover, Wang et al. (2009), Deng et al. 2011 and Li et al. (2011) observed two kinds of fine and coarse Fe-Al grains as well as some bare areas for dual phase steels (1-2 wt% Mn) galvanized using a 0.20wt% Al bath. They concluded that fine grains of  $\text{Fe}_2\text{Al}_5$

form on surfaces where small and thin oxides were completely removed by aluminothermic reduction. On the other hand, due to the lower number of nucleation sites between dense oxides not completely being reduced, higher dissolved Al is available for Fe-Al nuclei growing into coarse grains. Also, film-type oxide results in a discontinuous interfacial layer.

However, the aluminothermic reduction reaction will consume bath Al and, presumably, affect the formation kinetics and morphology of the interfacial layer. As a result, further study on the influence of Mn and its oxide on the galvanizability and interfacial layer formation is required and is a central facet of the present thesis.

#### **2.4.3.4 Bath temperature**

The bath temperature has an influence on the Al uptake and the interfacial layer morphology and composition. In high dissolved Al baths, by increasing the bath temperature the interfacial layer Al uptake increases (Figure 2.10) and the interfacial layer becomes non-compact and coarser. On the other hand, in low dissolved Al baths, increasing the bath temperature accelerates the inhibition breakdown and Zn-Fe intermetallic formation (Figure 2.16) due to higher Zn diffusion through the interfacial layer and grain boundaries of the steel substrate, and therefore, decreases the interfacial layer Al uptake (Figure 2.17) (Tang 1995, Toussaint et al. 1998, Chen et al. 2008, Dutta et al. 2009).

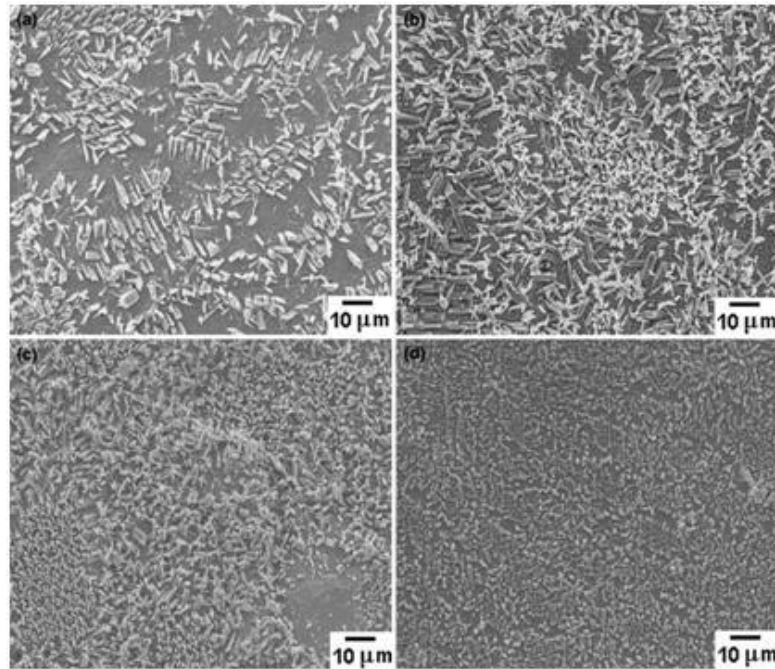


Figure 2.16: Morphology of the interfacial layer for a bath with 0.13 wt% dissolved Al as a function of bath temperature: (a) 450 °C, (b) 460 °C, (c) 470 °C and (d) 480 °C (reaction times ~4 s) (Chen et al. 2008).

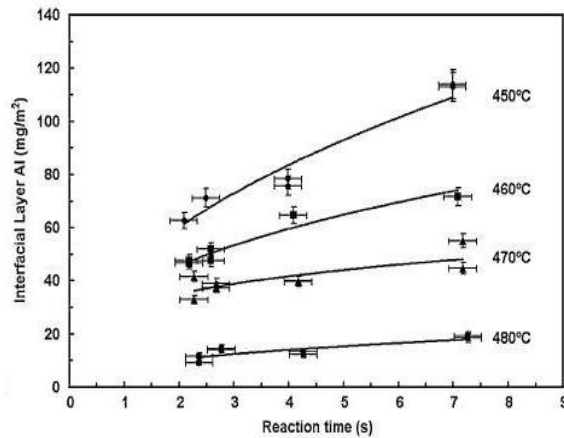


Figure 2.17: Effects of bath temperature on interfacial layer Al uptake for a bath with 0.13 wt% dissolved Al and different immersion times (Chen et al. 2008).

## 2.5 Kinetic models of interfacial layer growth

As was mentioned in section §2.3, by entering the steel sheet into the zinc bath the system comes out of equilibrium and a local supersaturation of iron in the vicinity of the sheet surface occurs which results in the nucleation of the interfacial layer (Nakano 2006, Leprêtre et al. 1998, Perrot et al. 1992). It is worth repeating that according to the Fe-Al-Zn phase diagram (Figure 2.4) for dissolved bath Al of less than 0.14 wt%,  $\text{Fe}_2\text{Al}_5$  is not in equilibrium with the liquid phase; rather,  $\delta\text{-FeZn}_{10}$  and  $\zeta\text{-FeZn}_{13}$  are the equilibrium intermetallics. However, it has been observed by multiple authors that  $\text{Fe}_2\text{Al}_5\text{Zn}_x$  forms on the substrate for dissolved Al baths as low as 0.05wt% (Guttman 1994, Leprêtre et al. 1998, Tang 1998, Baril and L'Esperance 1999). This is due to the high driving force for Fe-Al compound formation versus that for Fe-Zn intermetallic formation and because the system is in a metastable, not equilibrium, configuration. For this reason, kinetics rather than thermodynamic factors dominate this system for the time scales of interest and interfacial layer formation should be studied from the kinetics point of view. It should be noted that these studies are focused on simple alloy systems such as IF steels and there is virtually no knowledge concerning the role of alloying elements or their surface oxides on interfacial layer formation kinetics.

Tang (1995) proposed that interfacial layer formation commences through heterogeneous nucleation of a hemispherical cap of  $\text{Fe}_2\text{Al}_5$  with a critical nucleus diameter of  $d^*$  and nucleation energy barrier  $\Delta G^*$ , which can be written as:

$$d^* = \frac{-2\Delta\gamma}{\Delta G_v} \quad (2.16)$$

$$\Delta G^* = \frac{\pi\Delta\gamma^3}{3\Delta G_v^2} \quad (2.17)$$

where  $\Delta\gamma$  is the interfacial free energy change due to the formation of a hemispherical  $\text{Fe}_2\text{Al}_5$  nucleus ( $1.305 \text{ J/m}^2$ ), and  $\Delta G_v$  is the free energy change per unit volume of hemispherical  $\text{Fe}_2\text{Al}_5$  formed, calculated from the molar mass ( $0.247 \text{ kg/mol}$ ) and the density ( $4125 \text{ kg/m}^3$ ) of  $\text{Fe}_2\text{Al}_5$ . For a  $460 \text{ }^\circ\text{C}$  bath, the critical nucleus diameter and the energy barrier are  $0.65 \text{ nm}$  and  $1.36 \times 10^{-19} \text{ J}$  respectively; that is, the critical nucleus diameter is on the order of the diameter of Fe and Al atoms, implying that there is no practical nucleation barrier for interfacial layer nucleation.

Toussaint et al. (1998) proposed a mathematical model (equation 2.18) in terms of interfacial Al uptake ( $\text{mg/m}^2$ ) as a function of immersion time, considering the mixed-mode solid state diffusional growth (Smeltzer 1961) of the interfacial layer:

$$Q = A.t^{0.5} \quad (2.18)$$

where  $Q$  is the interfacial layer Al uptake ( $\text{mg/m}^2$ ),  $t$  is the immersion time (s) and  $A$  is a constant ( $\text{mg/m}^2.\text{s}^{0.5}$ ) calculated theoretically as follows:

$$A = f.A_{boundaries} + (1-f).A_{crystal} \quad (2.19)$$

$$A^2 = \left(\frac{135^2}{112^2}\right).2D\Delta C\rho\phi \quad (2.20)$$

where  $\phi$  is the Fe mass fraction of iron in  $\text{Fe}_2\text{Al}_5$  (112/247),  $\Delta C$  is the change in Fe concentration from one side of the interfacial layer to the other ( $5 \times 10^7 \text{ mg/m}^3$ ), (135/112) is the Al/Fe mass ratio in the  $\text{Fe}_2\text{Al}_5$  molecule,  $\rho$  is the density of the interfacial layer ( $4125 \times 10^6 \text{ mg/m}^3$ ),  $f$  is the volume fraction of boundaries, and  $D$  is the diffusion constant of Fe in  $\text{Fe}_2\text{Al}_5$  through the bulk lattice and grain boundaries, as proposed by Teixeira et al. (1987).

There are several issues in Toussaint's model (1998) which should be carefully considered.

(1) It is worth recalling that their model calculation is based on immersion time implying that the interfacial layer growth during solidification time has been neglected, so higher Al uptake values are calculated with the model.

(2) On the other hand, the volume fraction of grain boundaries ( $f$ ) in equation (2.19) was assumed to be 1; that is, the influence of bulk diffusion on the interfacial layer growth was neglected.

(3) Also, in calculating the diffusion of iron through the interfacial layer during the growth of the interfacial layer, data for the diffusion of Fe in Al (fcc) were used. This is

likely a poor assumption as it is known that the diffusion of Fe in Al is lower than the diffusion of Fe in  $\text{Fe}_2\text{Al}_5\text{Zn}_x$  due to the significantly higher vacancy concentration in the latter compound (Chen et al. 1990, Nakano 2007). Hence, lower Al uptake values are calculated with the model.

However, despite the fact that their model contains some significant errors due to incorrect galvanizing time estimation and assumptions for the interfacial layer microstructure and diffusion values, Toussaint et al. (1998) found that their model is in agreement with their experimental results, as shown in Figure 2.18.

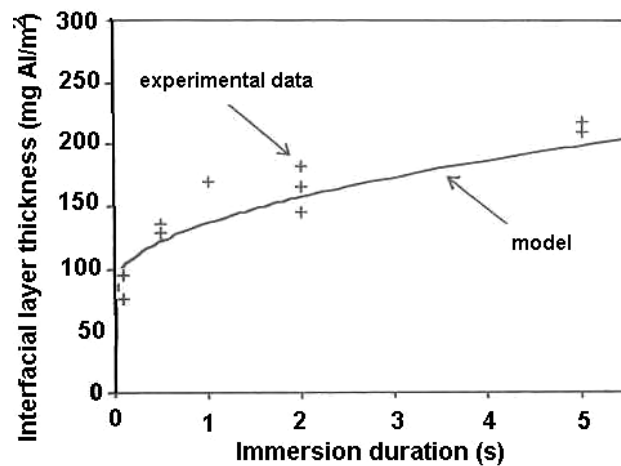


Figure 2.18: Prediction of the mathematical model with experimental results (Toussaint et al. 1998).

Giorgi et al. (2005) developed a model for the kinetics of galvanizing reactions based on solving the diffusion equations for iron and aluminium in the bath to obtain the

concentration profiles of iron and aluminium as a function of immersion time and space perpendicular to the steel surface, given by:

$$D_{Fe}^{Zn(L)} \frac{\partial^2 c_{Fe}}{\partial z^2} = \frac{\partial c_{Fe}}{\partial t} \quad (2.21)$$

$$D_{Al}^{Zn(L)} \frac{\partial^2 c_{Al}}{\partial z^2} = \frac{\partial c_{Al}}{\partial t} \quad (2.22)$$

where  $D_{Fe}^{Zn(L)}$  and  $D_{Al}^{Zn(L)}$  are the diffusion coefficients of Fe and Al in the zinc bath ( $m^2/s$ ).  $c_{Fe}$  and  $c_{Al}$  represent the Fe and Al concentration in the bath ( $mol/m^3$ ),  $z$  is the space variable in the direction perpendicular to the steel surface (m) and  $t$  is the immersion time (s). It should be mentioned that in their model, growth of the interfacial layer occurs in two steps: (i) lateral growth of Fe-Al crystals until the complete coverage of the steel surface, (ii) Fe diffusion controlled growth perpendicular to the steel surface towards. Based on their model (Figure 2.19), the growth of the interfacial layer starts after an incubation period of about 0.1 second, corresponding to the time needed for iron dissolved off the strip to reach supersaturation in the Zn bath. The growth rate is very high from 0.1 second to 0.4 second and then decreases significantly.

They validated their calculation results for the mass of Al in the interfacial layer with the experimental results of Toussaint et al. (1998) for 0.20 wt% Al bath and 460°C bath temperature (Figure 2.19). It can be seen that except for short immersion times, the experimental results were fit well by their model. The difference between experimental

and calculation results for short immersion time can be attributed to the overestimated interfacial Al measurements at 0.1 second due to the cooling time during which growth continued and /or underestimated because of some unwell known parameters of the model.

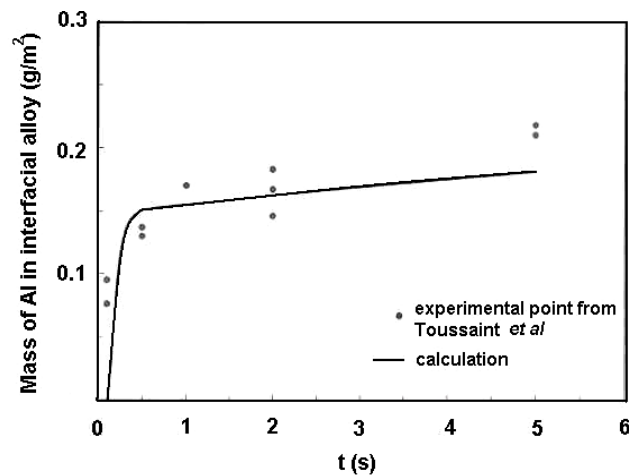


Figure 2.19: The model of Giorgi et al. (2005) vs. the experimental results from Toussaint et al. (1998) for 0.20 wt% Al bath and 460°C bath temperature.

Chen et al. (2008) proposed a kinetic model for Al uptake during interfacial layer growth (with  $\text{Fe}_2\text{Al}_5\text{Zn}_x$  as the composition) as a function of reaction time and temperature. They used the growth of an oxide film as an analogy for the growth of the interfacial layer (Smeltzer et al. 1961, Perrow et al. 1968, Herchl et al. 1972). In their model, the bulk lattice and grain boundaries were two paths for Fe diffusion through the

interfacial layer to react with Al in the liquid. Thus, the growth rate and the effective diffusion coefficient for Fe in the  $\text{Fe}_2\text{Al}_5\text{Zn}_x$  structure were defined as:

$$\frac{dx}{dt} = \Omega D_{eff} \frac{\Delta c}{x} \quad (2.23)$$

$$D_{eff} = D_L(1-f) + D_B f \quad (2.24)$$

where  $x$  is the interfacial layer thickness (m),  $\Omega$  the volume per Fe atom in the  $\text{Fe}_2\text{Al}_5\text{Zn}_x$  structure ( $\text{m}^3/\text{ion}$ ),  $\Delta c$  the concentration gradient of Fe ions at the interfacial layer ( $\text{ion}/\text{m}^3$ ),  $D_L$  is the lattice diffusion coefficient ( $\text{m}^2/\text{s}$ ),  $D_B$  the grain boundary diffusion coefficient ( $\text{m}^2/\text{s}$ ) and  $f$  the volume fraction of grain boundaries, taken to be a function of time as follows:

$$f(t) = \frac{2w}{d_t} = \frac{2w}{(d_0^2 + Kt)^{0.5}} \quad (2.25)$$

where  $w$  is the width of grain boundary (assumed to be 1 nm),  $d_t$  the mean grain size of the interfacial layer at reaction time  $t$  (m),  $d_0$  the initial grain size (zero in the present case), and  $K$  the rate constant for grain coarsening ( $\text{m}^2/\text{s}$ ). The experimental data and the line-intercept method were used to determine  $d_t$ . In order to simplify their geometry somewhat, Chen et al. (2008) assumed that the structure of the interfacial layer consisted of cubes of size  $d_t$  with a grain boundary of width  $w$ .

Following the derivation of Herchl et al. (1972) (substitution of equation (2.24) and equation (2.25) into equation (2.23)), and integrating using the boundary condition

that  $x=0$  at  $t=0$  and assuming that  $D_B \gg D_L$ , the growth law for the interfacial layer as a function of reaction time and bath temperature was obtained:

$$x^2 = K_p \left\{ t + \frac{D_B}{D_L} \frac{4w}{K} (d_0^2 + Kt)^{0.5} \right\} \quad (2.26)$$

$$K_p = 2\Omega D_L \Delta c \quad (2.27)$$

where  $K_p$  is the parabolic rate constant ( $\text{m}^2/\text{s}$ ).

Finally, the Al pick-up of the interfacial layer ( $\text{mg}/\text{m}^2$ ) was calculated as a function of reaction time as follows:

$$Al = 0.45 \times x \times \rho \quad (2.28)$$

where  $\rho$  is the density of  $\text{Fe}_2\text{Al}_5\text{Zn}_x$  ( $4125 \times 10^6 \text{ mg}/\text{m}^3$ ), and the factor 0.45 is the mass fraction of Al in  $\text{Fe}_2\text{Al}_5\text{Zn}_x$ .

Figure 2.20 shows that Chen et al.'s model (Chen et al. 2008) was in good agreement with their experimental results. It is worth to noting that the Chen et al.'s model (2008) was similar to Toussaint et al.'s model (1998). However, Chen et al.'s model was based on reaction time rather than immersion time. Also, the volume fraction of grain boundaries ( $f$ ) was not assumed to be 1 and was calculated via equation (2.25). In addition, the effects of the two Fe diffusion paths (grain boundaries and bulk diffusion) were considered quantitatively in the growth of the interfacial layer in this model (equation (2.24)). However, because of a lack of values for the diffusion of Fe in

$\text{Fe}_2\text{Al}_5\text{Zn}_x$ , the bulk to lattice diffusion ratio ( $D_B/D_L$ ) was chosen to be 100 in order to best fit the experimental data. Although this value is in the lower end of the ratio generally proposed for this ratio (10-1000), this lower value is consistent with the significant concentration of vacancies in the  $\text{Fe}_2\text{Al}_5\text{Zn}_x$  structure (Chen et al. 1990, Nakano 2007). Except for the adjustable parameter of  $D_B/D_L$ , the other parameters in equation (2.26) were derived directly from their experimental data.

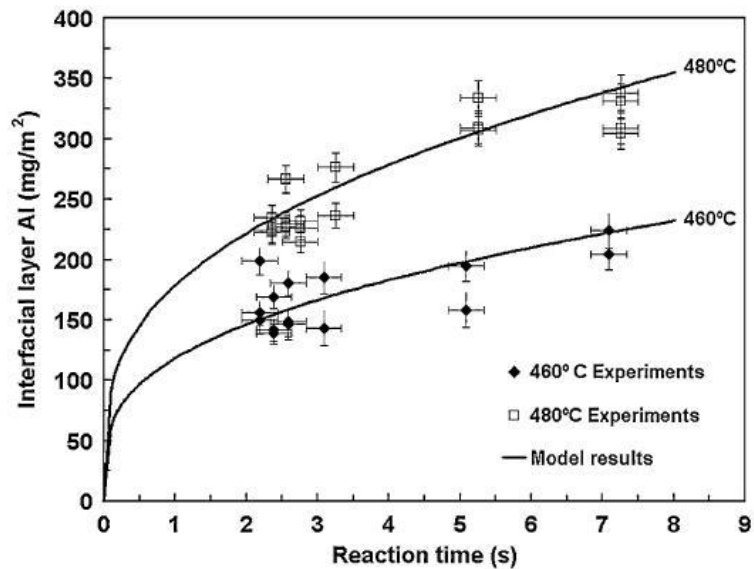


Figure 2.20: Al uptake as a function of reaction time for a 0.20 wt% dissolved Al bath (Chen et al. 2008).

It should be pointed out that above models (Toussaint et al. 1998, Chen et al. 2008) are based on the assumptions that: (i) the flux of Fe through the interfacial layer to react with Al in the zinc bath is the rate-limiting step in the growth process and (ii) the

bath dissolved Al supply is unlimited. Therefore, the effects of bath dissolved Al consumption via aluminothermic reduction of MnO layer on the interfacial layer formation kinetics particularly for high Mn-containing steels are not accounted for by these models. In fact, the effects of the alloying elements and their selective oxidation on the interfacial layer formation kinetics are areas in the current literature where data is lacking.

### **3 RESEARCH OBJECTIVES**

The overall objective of this study was to determine the short-time microstructural development and formation kinetics of the Fe-Al interfacial layer on Mn-containing steels. This study focused on three major areas:

(1) The selective oxidation of Mn-containing steel surfaces during annealing prior to hot-dip galvanizing as a function of steel chemistry, in this case focussing on the substrate Mn content. It should be noted that for the present study, the substrates being investigated will have relatively low C contents and Mn contents of 3.0wt% or less. In particular, the relationship between surface Mn oxide thickness and morphology and its possible effects on Fe-Al interfacial layer formation was one of the primary objectives of this investigation.

(2) The effect of the galvanizing parameters, including reaction time and bath dissolved Al content, on Fe-Al interfacial layer formation and development for a variety of Mn containing steels specified above. Using the hypothesis that aluminothermic reduction of the surface Mn oxide by the bath dissolved Al may affect the formation of the Fe-Al layer, a galvanizing bath with higher than conventional Al content(0.30 wt% Al) was considered as well as a bath of reasonably conventional Al content (0.20wt%). In the

present case, the investigation will be confined to a single bath temperature, in this case the relatively industrially convention temperature of 460°C.

(3) To develop microstructure-based model for the Fe-Al interfacial layer growth kinetics as a function of substrate Mn content, reaction time and bath dissolved Al content for a bath temperature of 460°C.

## 4 EXPERIMENTAL METHODS

### 4.1 Experimental materials

Four experimental steels with Mn contents ranging from 0.20-3.0 wt% were studied. The chemical compositions of the experimental steels are shown in Table 4.1. Although the chemistries listed show some slight variation in the majority of their alloying elements, the primary compositional experimental variable being explored in the present investigation is alloy Mn content. The 0.2Mn and 1.4Mn steels were supplied by U.S. Steel Canada and the 2.5Mn and 3.0Mn grades were fabricated at the CANMET Materials Technology Laboratory. Steels were received as cold-rolled sheet in a range of thicknesses between 0.8mm and 1.6mm. It should be noted that low Si and Al content of experimental steels guaranteed that no Si or Al oxides would be present on the annealed samples surfaces prior to dipping.

Table 4.1: Chemical composition of experimental steels (wt. %)

Alloy Name	C	Mn	Mo	Si	Nb	Al	P	S
0.2Mn	0.047	0.20	0.004	0.012	0.004	0.035	0.010	0.011
1.4Mn	0.066	1.40	0.003	0.085	0.071	0.036	0.007	0.004
2.5Mn	0.068	2.47	0.110	0.037	0.020	0.003	0.003	0.003
3.0Mn	0.077	2.98	0.086	0.028	0.022	0.005	0.003	0.003

## 4.2 McMaster galvanizing simulator

The McMaster Galvanizing Simulator (MGS, Iwatani-Surtec, Düsseldorf, Germany) was used for all experiments. The MGS and its schematic are shown in Figure 4.1 and Figure 4.2, respectively. The sample preparation section of the MGS consists of an atmosphere controlled column comprising several sections (Figure 4.1b and Figure 4.2). At the top of the column is the drive mechanism which allows rapid and precise movement of the sample to each process region of the MGS. Below this section are the sample loading/cooling and heating sections, respectively. The sample cooling rate is controlled by flowing N<sub>2</sub> through two parallel cooling plates. The MGS has two sample heating furnaces: a quartz lamp infrared furnace and a high frequency induction furnace. However, only the former was used in this study for sample heat treatments where the latter is used largely for galvannealing. The three upper sections are separated from the lower chamber by a pneumatically controlled gate valve to allow for evacuation of the upper chamber (0.0003 mbar) at the beginning of each experiment. The lower section consists of the molten zinc bath, gas-jet wiping to control the Zn-alloy coating thickness and a He jet spot cooler. The zinc pot consists of a resistance heated 50 kg graphite crucible controlled to within  $\pm 2$  °C using a type K thermocouple and a conventional process controller. Gas-jet wiping is located immediately above the zinc pot and controls the coating thickness using a 500 L/min N<sub>2</sub> gas flow. The He jet spot cooler used a He

flow rate of 500 L/min to achieve the high cooling rates (approximately 100°C/s) required to rapidly solidify the zinc coating in order to effectively arrest the reaction between the substrate and molten zinc overlay in a well-controlled manner. The lower chamber was maintained at a low oxygen partial pressure ( $pO_2$ ) of approximately  $10^{-15}$  atm by continuous  $N_2$  purging. In addition, the molten zinc surface was skimmed immediately prior to panels being dipped in the zinc bath via a graphite paddle dross removal system.

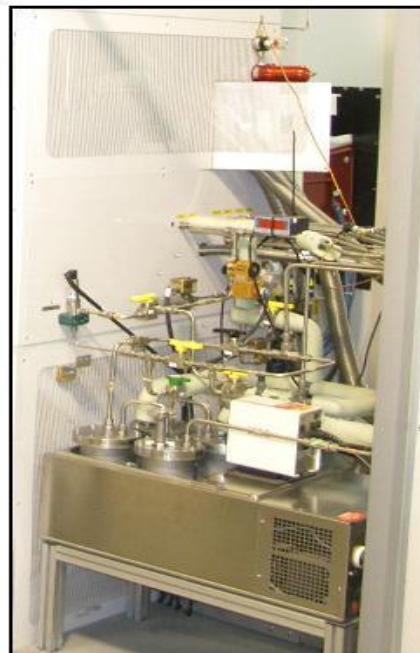
Process gases, dry  $N_2$  and  $H_2$ , were premixed in the gas mixing station and then fed into the upper column via two streams: (i) one dry stream and (ii) one wet (water saturated) stream passed through the humidification system (Figure 4.1c). The relative feed rates of the wet and dry gas streams controls the  $pH_2O$  of the annealing atmosphere, which then determines the  $pO_2$  through the water-gas reaction.



a)



b)



c)

Figure 4.1: a) The McMaster Galvanizing Simulator (MGS), b) Main Column and c) humidification system.

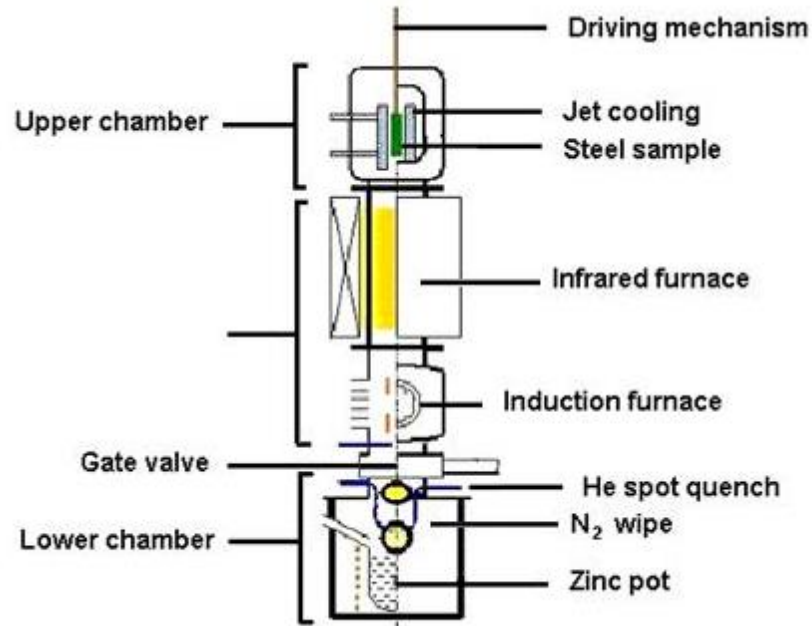


Figure 4.2: Schematic of the McMaster Galvanizing Simulator (Chen 2008).

### 4.3 Sample preparation

Selected samples were subjected to the annealing cycle without dipping in the zinc bath in order to study the selective oxidation of the steels surfaces as a function of steel Mn content. Samples for oxidation experiments comprised 12 mm x 50 mm strips, as shown in Figure 4.3a. Their surfaces were polished to 0.05 $\mu$ m with diamond paste and alumina suspension before annealing in order to eliminate the effect of surface roughness from subsequent analyses. After annealing and removal of the sample from the MGS and

prior to analysis, samples were stored in anhydrous isopropanol to minimize further oxidation of the surface.

Prior to annealing and galvanizing, steel panels were degreased in an 80°C 2 wt% aqueous sodium hydroxide solution, rinsed with deionized water, cleaned ultrasonically in isopropanol and dried with warm air. A final cleaning with acetone was performed immediately prior to the sample entering the galvanizing simulator. The purpose of this step was to remove loose iron fines and organic contaminants in a manner similar to that employed industrially (Sendzimer 1938).

Galvanized samples comprised 120 mm x 200 mm panels with the longitudinal axis of the sample oriented parallel to the rolling and dipping direction (Figure 4.3b). Two type K (0.5 mm) thermocouples were welded directly onto the steel panel surface prior to the start of experiments (Figure 4.3b). The first thermocouple was placed above the galvanizing line and was used to control the sample thermal cycle. The second thermocouple was placed on the He quench spot to monitor the temperature changes at this location during He spot quenching for the purposes of calibrating the quenching rate at this location. Sample temperature measurements were accurate to within  $\pm 3$  °C. However, the galvanized sample thermal cycles were controlled only with the upper thermocouple during galvanizing (Figure 4.3c). The galvanized panel dimensions used for reaction time calibration and galvanizing experiments, the location of the two thermocouples and the quench spot position are shown in Figure 4.3(b,c).

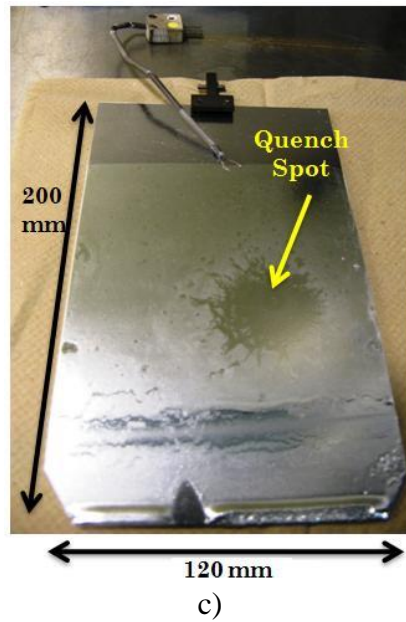
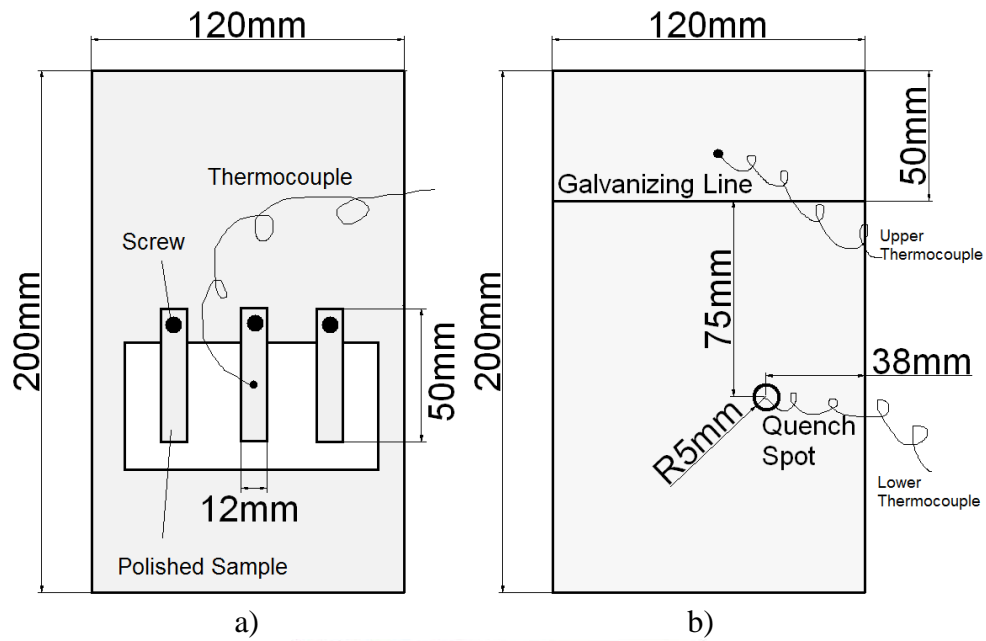


Figure 4.3: Steel panel dimensions for a) selective oxidation experiments, b) reaction time calibration and c) galvanizing experiments.

#### 4.4 Annealing and galvanizing experimental parameters

Before running each experiment, the upper chamber of the MGS was evacuated to  $2.97 \times 10^{-7}$  atm in order to remove ambient oxygen and adsorbed moisture before an annealing cycle. Annealing was started by setting the process atmosphere dew point ( $dp$ ) to  $-30^\circ\text{C}$  and flowing the process gas (95%  $\text{N}_2$ , 5%  $\text{H}_2$  (volume %)) into the column. The heat treatment prior to galvanizing consisted of heating at  $10^\circ\text{C/s}$  to the peak annealing temperature (PAT), holding isothermally at the peak annealing temperature for 120s and finally cooling at  $-20^\circ\text{C/s}$  to the bath temperature of  $460^\circ\text{C}$ . The 95%  $\text{N}_2$ , 5%  $\text{H}_2$ ,  $-30^\circ\text{C}$   $dp$  process atmosphere was chosen as this is typical of those used in industrial continuous galvanizing lines. The PAT was chosen to produce a microstructure comprising 30% austenite ( $\gamma$ ) + 70% ferrite ( $\alpha$ ) (volume %) for each alloy composition, as calculated using Thermo-Calc® software and the TCFE2 database and is shown in Table 4.2. The process atmosphere  $pO_2$  is strongly temperature dependent and was calculated as a function of steel PAT (Table 4.2) using the thermodynamic data of Fine and Geiger (1979).

Table 4.2: Experimental parameters

Alloy Name	PAT (°C)	$pO_2$ at PAT(atm)	Immersion Time(s)	Reaction Time (s)
0.2Mn	840	$3.39 \times 10^{-22}$	0.5/0.7/1.0/	2.13/2.26/2.66/3.01/3.55/4.02/5.56/7.61
1.4Mn	770	$9.22 \times 10^{-24}$	1.5/2.0/2.5/	2.20/2.33/2.73/3.08/3.62/4.09/5.63/7.68
2.5Mn	724	$6.59 \times 10^{-25}$	4.0/6.0	2.23/2.36/2.76/3.11/3.65/4.12/5.66/7.71
3.0Mn	704	$1.94 \times 10^{-25}$		2.23/2.36/2.76/3.11/3.65/4.12/5.66/7.71

The Zn (Al, Fe) bath was held at 460°C and had an Fe content such that the bath was saturated with respect to  $\text{Fe}_2\text{Al}_5\text{Zn}_x$  (McDermid et al. 2007). Two different bath dissolved Al contents (0.20 and 0.30 wt. %) were chosen in the present work. The 0.20 wt. % Al bath was chosen as it is widely used in industrial continuous galvanizing lines. The 0.30 wt. % Al bath was chosen to compensate for any dissolved Al consumption arising from MnO reduction in the galvanizing bath (Kavitha and McDermid 2012). Sample immersion times were varied from 0.5s to 6s (Table 4.2). As was noted in §2.3.3.1, sample immersion time is not equal to sample reaction time and the present research is based on the latter. The reaction time was calculated through the logged samples time/temperature/position profile of the thermocouple at the He spot cooling position during calibration runs as shown in Table 4.2. Complete details concerning the reaction time calculation will be discussed in §4.4.1. In addition, samples subjected to immersion times greater than one second were oscillated at 10 mm/s and 0.5 Hz within the bath to ensure a continuous supply of fresh bath metal to the steel surface.

After dipping and before rapid cooling,  $\text{N}_2$  gas jet wiping was used to obtain an average coating weight of 60 g/m<sup>2</sup>. Immediately following gas-jet wiping, the sample was moved to the He spot cooling position, where the He spot cooling position was subject to a He flow rate of 500 L/min for 7s. Only material from the spot cooling position was used for subsequent analyses. Cooling to ambient temperature was performed in the upper

chamber where the sample was cooled to room temperature by 500 L/min N<sub>2</sub> gas from both sides, after which the sample was removed from the MGS for further processing.

#### 4.4.1 Reaction time calculation

As mentioned before, the sample reaction time is different from the immersion time as post-immersion diffusion of Al to the substrate-coating interface occurs during coating solidification after wiping. For this reason, the sample reaction time should be considered when assessing the kinetics of interfacial layer formation. The reaction time was calculated through the logged samples time/temperature/position profile as shown in Figure 4.4. In this Figure, the blue and red curves indicate the temperatures for the upper and quench spot thermocouples (Figure 4.3b), respectively. The sample position in the simulator is illustrated by the green curve; this data is based on the distance between the top of the steel panel and the reference position (i.e. ground). It should be noted that the system starts counting immersion time after the steel panel reaches its minimum position in the zinc pot. As a result, the spot cooling position on the steel panel has already contacted the zinc bath before the immersion time counter starts. As a result, the calculation of the reaction time is defined as the sum of four times (equation (4.1)):

$$t_{reaction} = t_1 + t_2 + t_3 + t_4 \quad (4.1)$$

where  $t_1$  is the difference between the time when the rapid cooling spot contacts the zinc bath and the time when the immersion time counter is started (i.e. travel time of the spot

cooling position in the bath before the start of the immersion time count),  $t_2$  the immersion time,  $t_3$  the time taken for the spot cooling position to move from the immersion position to the spot cooling position and  $t_4$  the time taken for the spot cooling temperature to fall below 420°C (i.e. the zinc melting temperature), at which time the interfacial reaction layer growth is considered to be arrested. Here, it was assumed that the reaction rate decreased significantly when the temperature was below 420°C, as liquid reactions are much faster than solid state reactions. Table 4.3 summarizes the reaction time for all samples. Different  $t_4$  value for different Mn-containing steels is due to the different panel thickness which affects the cooling rate.

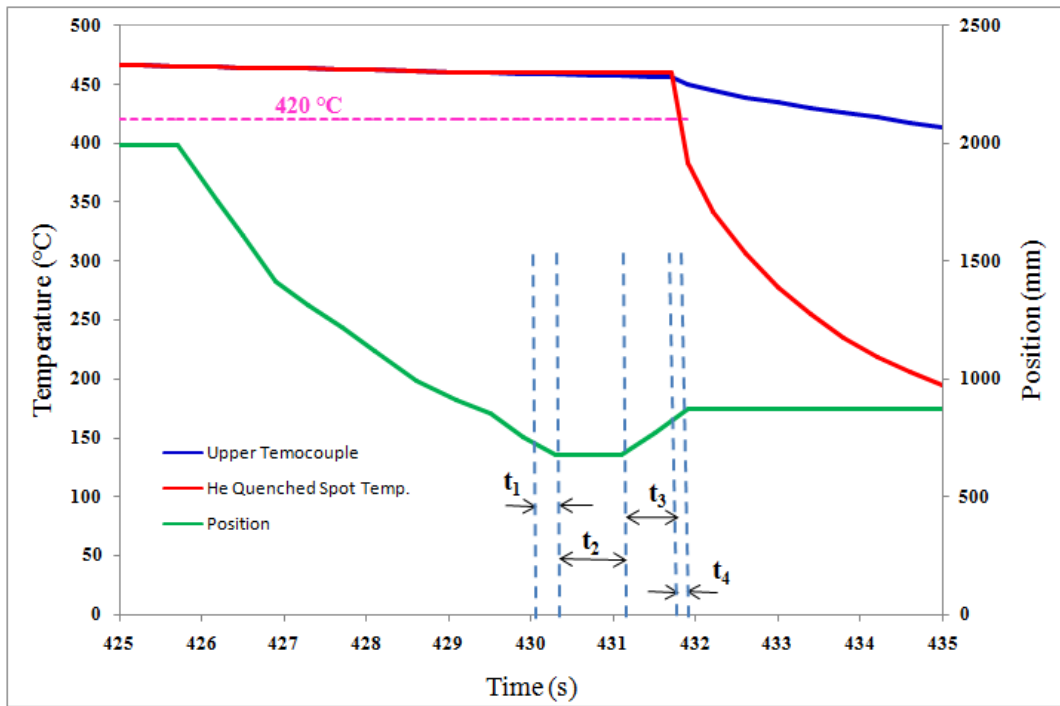


Figure 4.4: Time, temperature and position log for a galvanized sample.

Table 4.3: Reaction time calculation

Alloy Name	$t_1$ (s)	$t_2$ (s)	$t_3$ (s)	$t_4$ (s)	Total Reaction Time (s)
0.2Mn				0.11	$1.44+t_2$
1.4Mn	0.41	0.69/0.82/1.22/	0.92	0.18	$1.51+t_2$
2.5Mn		1.57/2.11/2.58/		0.21	$1.54+t_2$
3.0Mn		4.12/6.17		0.21	$1.54+t_2$

## 4.5 Analytical procedures

### 4.5.1 X-ray photoelectron spectroscopy (XPS)

XPS is a surface analysis technique in which the sample surface is bombarded under an ultra-high vacuum with X-rays, which are absorbed by the atoms of the sample. Absorbed X-ray energy is used to eject a photoelectron from either a core level or a valence level of an atom by overcoming the electron binding energy. By measuring the kinetic energy of the outgoing photoelectron, the binding energy ( $E_B$ ) can be calculated from equation (4.2) (Bubert and Jenett 2011), where  $E_B$  is characteristic of a specific electron orbital in a specific atom and varies for elements in different chemical states (e.g. metal vs. oxides or other compounds), and from which the chemical state of a compound or element on the surface of the sample can be determined. It should be noted that XPS cannot be used for H or He analysis because their binding energies (1s orbital) are very low (13.6 and 24.6 eV, respectively).

$$E_{kin} = h\nu - E_B - \phi_s \quad (4.2)$$

where  $E_{kin}$  is the measured kinetic energy of the photoelectron,  $h\nu$  is the energy of the incident X-ray photons (where  $h$  is Plank's constant and  $\nu$  the frequency of the incident X-rays),  $E_B$  the electron binding energy relative to the Fermi level and  $\phi_s$  the work function of the spectrometer (a constant representing the difference between vacuum and the Fermi level).

The chemical state of the elements or compounds present on the annealed sample surface and subsurface prior to dipping, compositional depth profiles and oxide layer thicknesses were determined using X-ray photoelectron spectroscopy (XPS) *via* a PHI Quantera XPS (Physical Electronics, Chanhassen, MN) equipped with an Al K $\alpha$  X-ray source (1486.6 eV). XPS data was processed using MultiPak software (Version 6). The spot size was 100 $\mu$ m and the take off angle was 45°. All spectra were calibrated using the metallic iron binding energy peak position at 706.6 eV. The binding energy values obtained were accurate to within  $\pm 0.1$ eV and the accuracy of the chemical composition measurements was  $\pm 5\%$  of the measured value in atomic percent. The XPS binding energy results shown were collected after 9nm sputtering with Ar to remove any surface contamination and further oxidation which may have occurred during sample handling. XPS depth profiles were obtained by Argon sputtering followed by analysis of the new surface. The error associated with the depth measurements is  $\pm 10\%$  of the indicated depth.

#### **4.5.2 Scanning electron microscopy (SEM)**

The oxide morphology on the surface of the as-annealed steels was observed with a JEOL 7000F field emission gun scanning electron microscope (FEG-SEM). An acceleration voltage of 5 keV and a working distance of 6 mm were used for all samples. All samples were sputter coated with platinum to avoid sample charging.

The interfacial layer microstructures were also studied by analyzing the steel substrate/zinc coating interface via a JEOL 7000F FEG-SEM using an acceleration voltage of 5 keV and a working distance of 6 mm and via a FEI Magellan 400high resolution SEM (XHR-SEM) using an acceleration voltage of 3 keV and a working distance of 3 mm. The interfacial layer on the spot cooling side was exposed for SEM analysis by stripping the Zn overlay using 10 vol. % aqueous sulphuric acid ( $H_2SO_4$ ) which dissolves only the Zn overlay, leaving any Fe-Zn and Fe-Al intermetallics intact. Stripping was stopped when a small amount of the Zn overlay remained at the centre of the sample. This solution did not uniformly strip the coating and resulted in three different layers on the sample surface: remained Zn overlay at the centre of the sample surrounded by a dark gray layer consisted of Fe-Zn and Fe-Al intermetallics and light grey area of steel substrate at the sample edges. The side opposite the spot cooling side was protected from dissolution using electrogalvanizer's tape.

#### **4.5.3 Scanning Auger microscopy (SAM)**

Scanning Auger microscopy (SAM) is an analytical technique that is used to determine the elemental composition of the top few nanometres of the sample surface by measuring the kinetic energy of the Auger electrons produced through interactions of the atoms with the incident electron beam, which are characteristic of the atoms from which they were emitted (Grant 2003, Briggs and Rivière 1983).

The correlation between surface oxide morphology and elemental distribution was determined using a JEOL JAMP-9500F Field Emission Auger Microprobe (FEG-SAM). Auger maps were collected at the steel surface and after Ar sputtering to a depth of 20 nm in order to eliminate surface iron oxides formed after sample removal from the galvanizing simulator. The accuracy of the sputtering depth was  $\pm 10\%$ . The primary electron beam energy was 15 keV and the samples were tilted at  $30^\circ$  toward the electron analyzer. The signal intensity (I) was calculated using equation (4.3) to attenuate the effect of topography.

$$I = \frac{\text{peak-background}}{\text{background}} \quad (4.3)$$

#### **4.5.4 Transmission electron microscopy (TEM)**

Cross-sections of the steel/zinc coating interface were analyzed by transmission electron microscopy (TEM) to investigate the fine-scale structure of the Fe-Al interfacial layer formation and remaining Mn oxides. TEM was performed using a JEOL 2010F TEM equipped with an Oxford INCA energy dispersive X-ray (EDX) spectrometer. EDX was performed in scanning transmission electron microscopy (STEM) mode for elemental mapping and for quantitative point analysis. The acceleration voltage was 200 keV and probe size was 1 nm.

TEM samples were prepared using focused ion beam (FIB) milling *via* a NVision 40 by Zeiss. FIB is an ideal technique in making thin samples of the cross-section across

the steel/coating interface from a specific area of interest with uniform thickness (Goldstein et al. 2003). The different steps of FIB sample preparation are shown in Figure 4.5. As Zn is sputtered more easily than Fe, a protecting tungsten film was deposited over the FIB samples to minimize the preferential thinning of the Zn overlay.

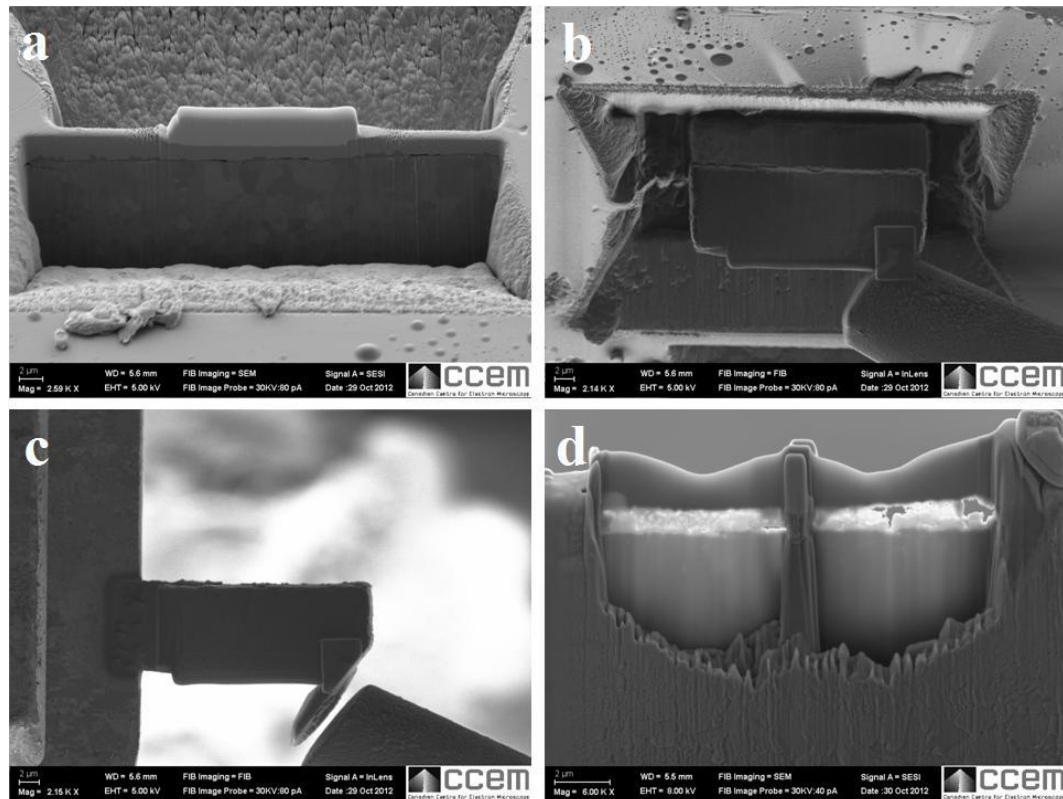


Figure 4.5: Steps of FIB sample preparation taken from the quench spot a) milling of trenches on either side of the sample, b) milling around the sample and welding of the probe to the sample, c) welding of the sample to the Cu grid and d) further milling to achieve an electron transparent sample.

#### **4.5.5 Inductively coupled plasma spectroscopy (ICP)**

ICP is a wet chemical analytical technique capable of identifying and quantifying elements at concentration as low as parts per billion (ppb). ICP requires that the elements which are to be analyzed be in solution. The resident nebulizer transforms the solution into an aerosol which is carried into the plasma to create ions and subsequently emission of photons. These photons have characteristic energies. Thus, the wavelength of the photons can be used to identify the elements from which they originated and converted to an electrical signal by a photodetector. The signal is processed and measured quantitatively. The intensity of the electrical signal is compared to previously measured intensities of known concentration of the element via calibration and a concentration computed (Dean 2005, Hill 2007).

The chemical composition, in particular the Al uptake in  $\text{mg/m}^2$ , of the interfacial layer at the rapid cooling spot was determined by wet chemical analysis using ICP and matrix-matched standards. The standards used for calibration are samples in which their matrices and elemental concentrations are close to that of the samples to be analyzed.

The quench spot was first cut from the steel panel and its area determined using a Leica optical stereoscope coupled with an image analysis system (Clemex IA, Clemex Technologies, Inc., Longueuil, QC, Canada). The zinc overlay was stripped with fuming nitric acid ( $\text{HNO}_3$ ) which strips the zinc overlay and Fe-Zn intermetallics leaving any Fe-Al intermetallics intact. A 10 vol. %  $\text{H}_2\text{SO}_4$  solution with Rodine<sup>TM</sup> 85 inhibitor was then

used to dissolve the exposed Fe-Al interfacial layer from the steel substrate using the procedure “Zinc products and applications – galvanized coatings selective stripping procedure” provided by Noranda Inc.: 1) cover the opposite side of the sample with electrogalvanizer’s tape; 2) immerse the sample with polymeric pliers into 40ml of the 10 vol. % H<sub>2</sub>SO<sub>4</sub> solution with Rodine™ 85 inhibitor solution; 3) remove the sample when the steel substrate is of uniform appearance; 4) pour the stripping solution into a 50ml volumetric flask and dilute to 50ml with 10 vol. % H<sub>2</sub>SO<sub>4</sub> solution with Rodine™ 85 inhibitor. The Al content of the above solution was measured by ICP using matrix-matched standards, i.e. 0.1, 0.3, 0.5, 1, 3 ppm Al, Fe, Mn, Zn reference solutions dissolved in a 10 vol. % H<sub>2</sub>SO<sub>4</sub> solution with Rodine™ 85 inhibitor. The accuracy of this technique is ±0.5% of the analyte. The obtained results was used to assess the interfacial layer Al uptake expressed in units of mg(Al)/m<sup>2</sup> of substrate.

## **5. RESULTS: SELECTIVE OXIDATION AND INTERFACIAL LAYER FORMATION**

Mn selective oxidation of Mn-containing steel surfaces during annealing prior to hot-dip galvanizing was studied. The effect of the MnO layer arising from selective oxidation as well as the bath dissolved Al content were then related to the formation kinetics and microstructural evolution of the Fe-Al interfacial layer.

### **5.1 Steel selective oxidation during annealing**

The selective oxidation of the steel surface during annealing prior to dipping in the molten zinc bath was examined using a variety of advanced analysis techniques such as XPS, SEM and SAM. Surface chemistry and oxide morphology are discussed as a function of steel Mn content.

#### **5.1.1 X-ray photoelectron spectroscopy analysis**

The chemical state of the elements present on the sample surface prior to dipping, compositional depth profiles and oxide layer thicknesses were determined using X-ray photoelectron spectroscopy (XPS). Fe and Mn XPS spectra for the 1.4Mn steel for all sputtering depths are shown in Figure 5.1. Similar trends in the XPS spectra were observed for the other experimental steels. However, weaker Mn spectra were observed for 0.2Mn steel. According to the binding energies in Table 5.1 taken from the XPS spectra, Mn surface enrichment occurred during annealing for all experimental steels in the form of MnO (Strohmeier and Hercules 1984), where their intensity decreased with

increasing sputtering depth (Figure 5.1b). It should be noted that the small peaks at 646 eV in Figure 5.1 are bare satellite peaks corresponding to MnO (Biesinger et al. 2011). It should be noted that Fe oxides and/or hydroxides (Grosvenor et al. 2004) were detected only the first few nanometers at the surface of the samples (red curve at the bottom of Figure 5.1a) and can be considered to be an artefact from exposing the samples to the ambient atmosphere upon removal from the galvanizing simulator.

XPS depth profiles for Mn are shown for all experimental steels in Figure 5.2. As expected, the 0.2Mn steel showed little Mn segregation at the surface because of its relatively low Mn content, whereas the 1.4Mn through 3.0Mn steels showed considerable Mn surface enrichment. Oxide thickness was assessed by measuring the depth at which the Mn concentration profile reached half of its maximum value, usually referred to as the full width at half maximum (FWHM). The influence of steel Mn content on the FWHM oxide thickness is shown in Table 5.2. It can be seen that the oxide layer thickness increased with the alloy Mn content.

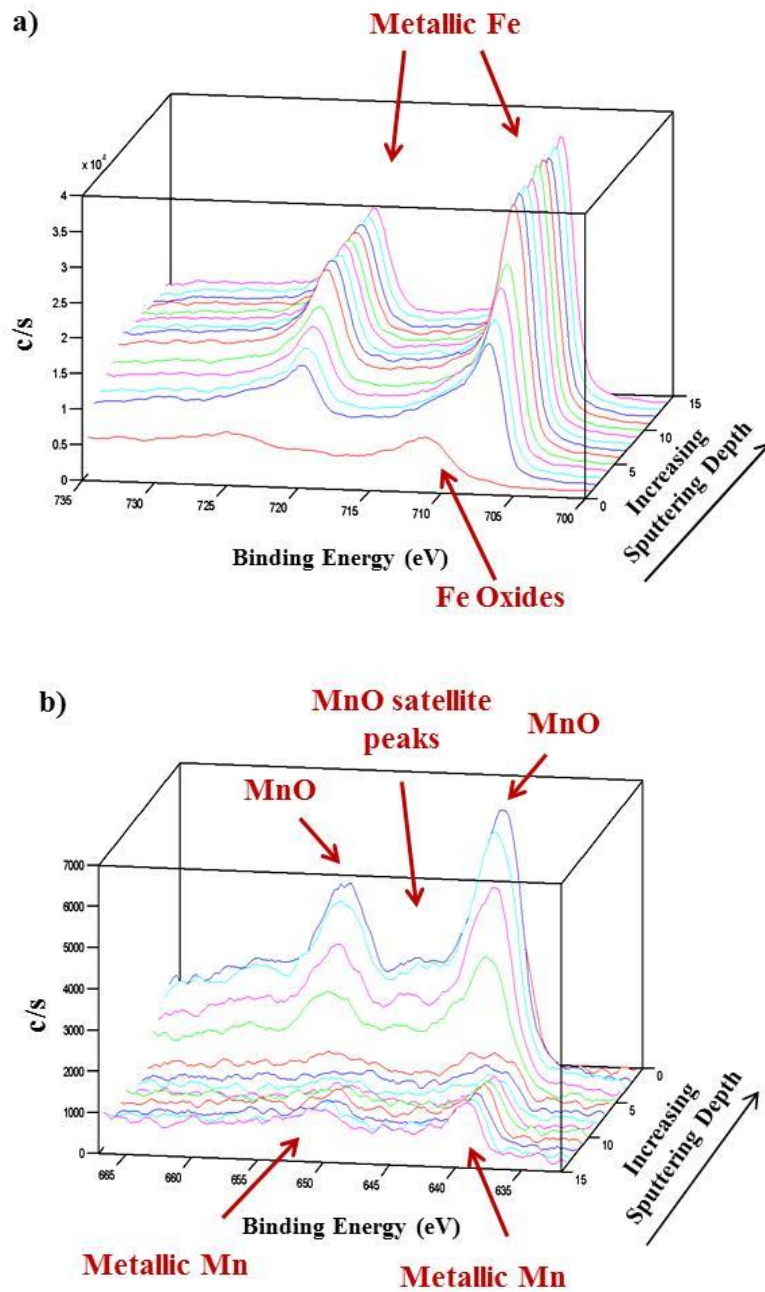


Figure 5.1: XPS spectra as a function of sputtering depth for a) Fe and b) Mn (please note the difference in the depth scale order).

Table 5.1: XPS identification of steel surface constituents (after 9 nm sputtering)

Measured Binding Energy (eV)				State (Compound)
Fe 2p <sub>3/2</sub>	Mn 2p <sub>3/2</sub>	Mn 2p <sub>1/2</sub>	O 1s	
706.6	641.6	653.4	530.4	MnO, Fe (metallic)

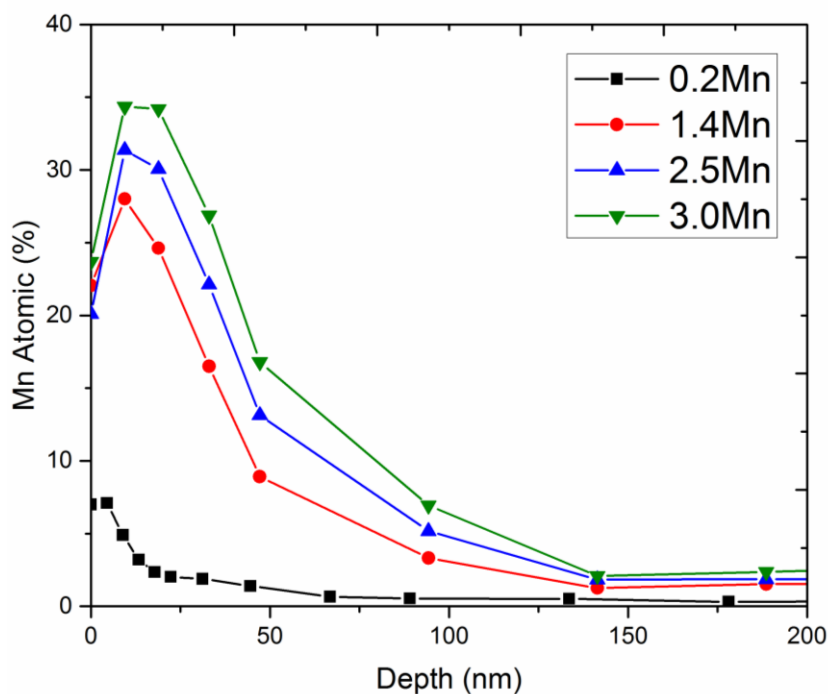


Figure 5.2: Mn XPS depth profile as a function of steel Mn content for the as-annealed alloys.

Table 5.2: Effect of steel Mn content on FWHM MnO thickness and area percentage oxide coverage

Alloy Name	MnO FWHM Thickness (nm)	Surface MnO Coverage (%)
0.2Mn	12	-
1.4Mn	38	29.8
2.5Mn	44	34.9
3.0Mn	47	60.4

### **5.1.2 Scanning electron microscopy analysis**

The surface of the as-annealed steels was studied using scanning electron microscopy (SEM) (Figure 5.3). The 0.2Mn steel showed some oxides at the grain boundaries with small sparse oxide particles on the bulk grain surface. However, significant populations of oxide nodules on the bulk grains as well as oxide ridges at the grain boundaries were observed for all the higher Mn steels. In fact, by increasing the steel Mn content the population of oxide nodules on the surface increased and their coalescence were observed for higher Mn steels (Figure 5.3c and d). The film morphology at the grain boundaries is indicative of external oxidation at these short circuit diffusion paths arising from the increased O and Mn diffusion rates. In addition, the oxide particle size on the 0.2Mn steel surface was considerably smaller than that on the higher Mn steels surfaces.

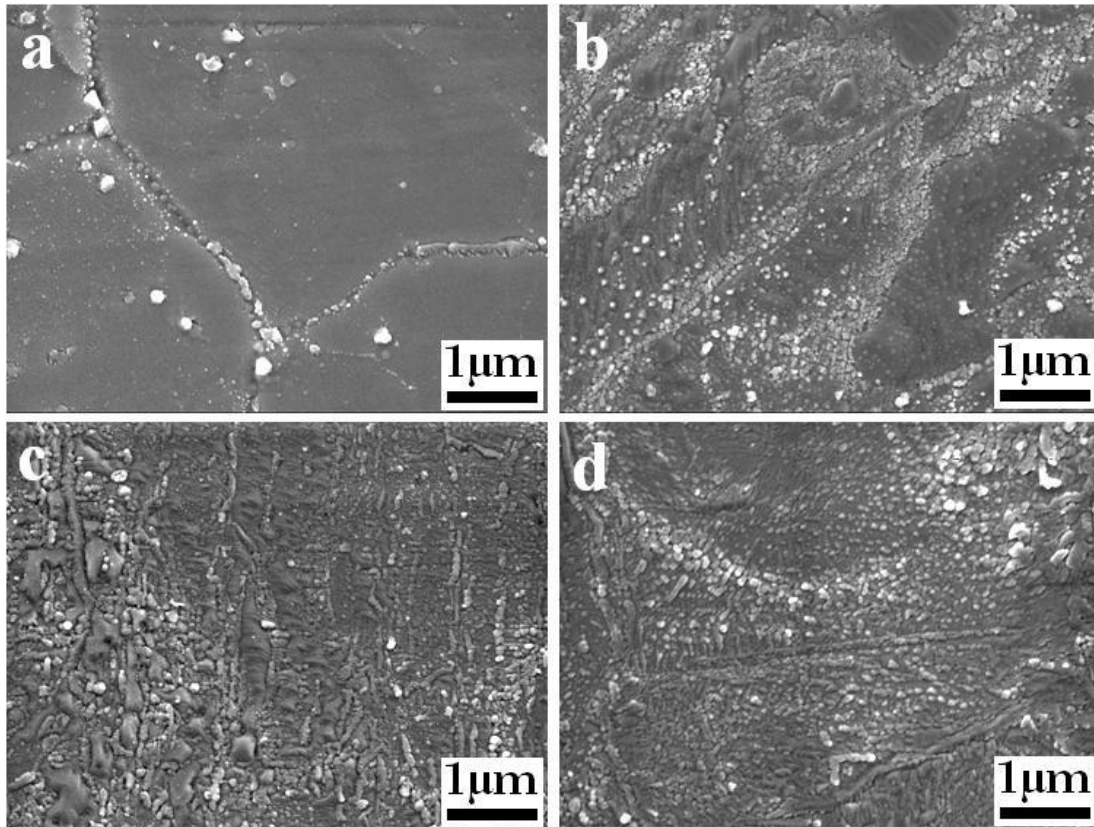


Figure 5.3: SEM images of the distribution of oxides on the steel surface annealed at  $-30^{\circ}\text{C}$  dew point, (a) 0.2Mn, (b) 1.4Mn, (c) 2.5Mn, (d) 3.0Mn steels.

### 5.1.3 Scanning Auger microscopy analysis

The distribution and morphology of surface oxides on the 1.4Mn, 2.5Mn and 3.0Mn steels were further investigated using scanning Auger microscopy (SAM). Secondary electron images of the steel surface and corresponding elemental maps are shown in Figure 5.4 through Figure 5.6. Two sets of maps were collected for each sample: one set for the as-received steel surface and the other after 20 nm sputtering with

Ar. Elemental maps before sputtering showed that the surface was oxidized to Fe oxides, as previously discussed in XPS results (red curve in Figure 5.1a), an artefact of removing the sample from the galvanizing simulator after annealing. As a result, the only maps shown after 20 nm sputtering are shown here to highlight the strong correlation between the O and Mn rich areas, which are indicative of the MnO morphology on the as-annealed surfaces.

The 1.4Mn steel showed sparse oxide nodules on the bulk grains as well as oxide ridges at the grain boundaries (Figure 5.4) which is in consistent with SEM results (Figure 5.3b). However, for the higher Mn steels, larger oxide nodules were distributed on the bulk grain surfaces and oxide films at the grain boundaries and adjacent areas were observed (Figure 5.5 and Figure 5.6) which is in agreement with SEM images (Figure 5.3c and d). These nodules and ridges were identified as MnO through comparison of the SAM secondary electron image to the Mn and O maps and the XPS results (Table 5.1). The oxide film morphology at the grain boundaries is indicative of external oxidation at these short circuit O and Mn diffusion paths. A significant amount of non-oxidized Fe was observed on the surface of all the steels. The fraction of the surface covered by MnO was determined using image analysis and is shown in Table 5.2. It can be seen that the proportion of the surface covered by MnO increased with increasing steel Mn content.

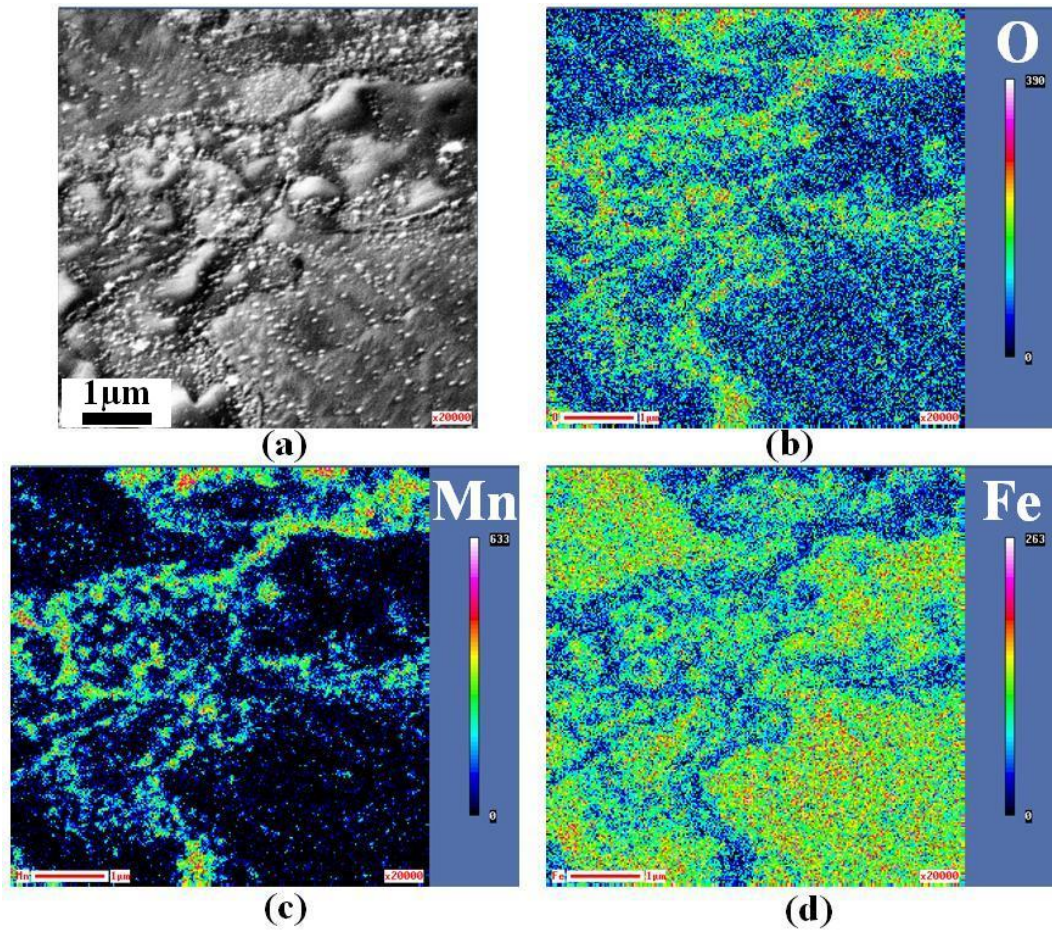


Figure 5.4: SAM elemental mapping of the 1.4Mn after Ar sputtering to 20 nm: (a) secondary electron image, (b) oxygen, (c) manganese and (d) iron.

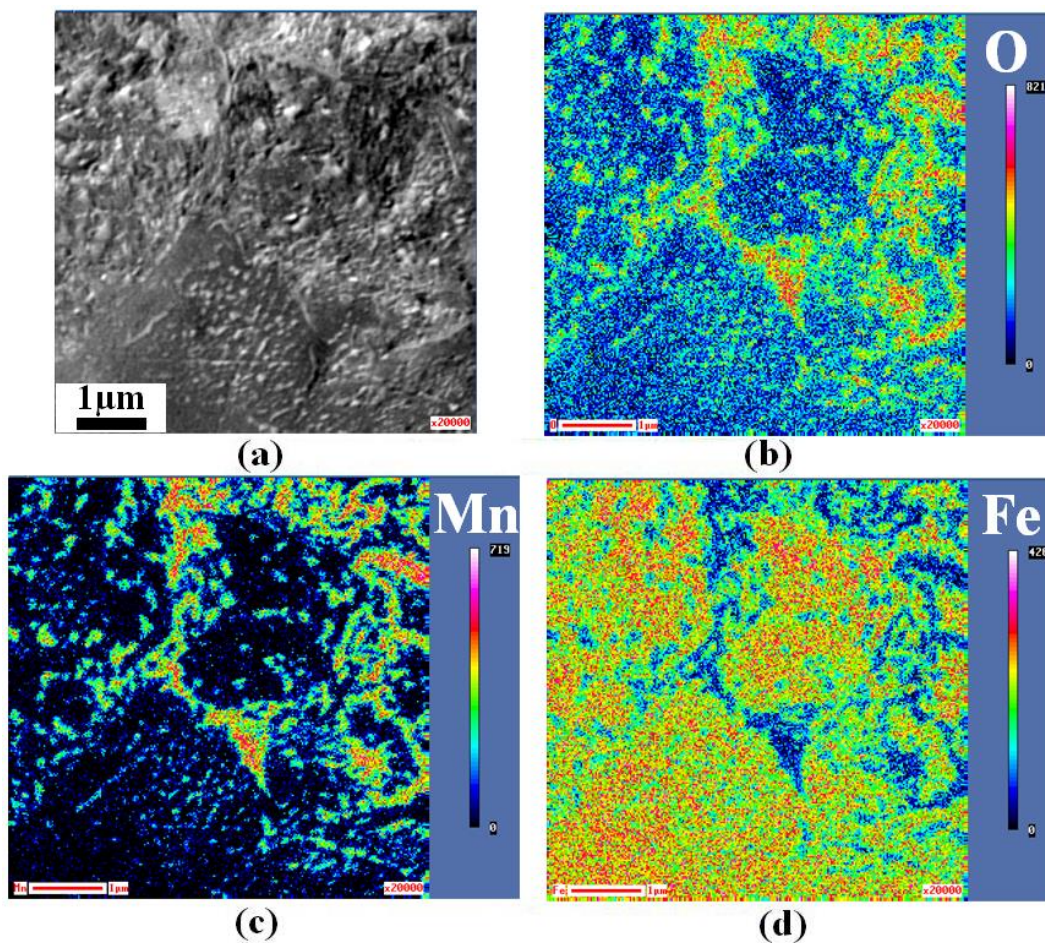


Figure 5.5: SAM elemental mapping of the 2.5Mn after Ar sputtering to 20 nm: (a) secondary electron image, (b) oxygen, (c) manganese and (d) iron.

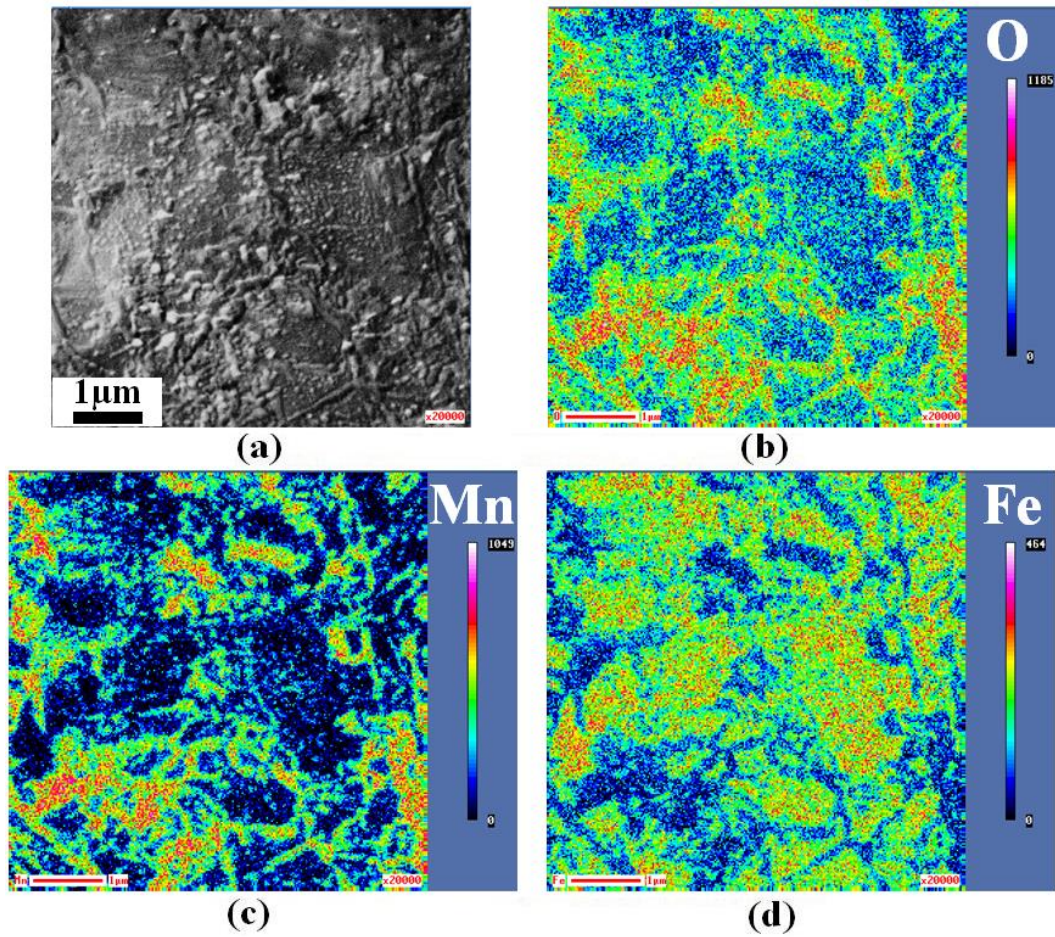


Figure 5.6: SAM elemental mapping of the 3.0Mn after Ar sputtering to 20 nm: (a) secondary electron image, (b) oxygen, (c) manganese and (d) iron.

## **5.2 Fe-Al interfacial layer development**

The Fe-Al interfacial layer development was studied as a function of reaction time, bath dissolved Al content and steel Mn content using well defined reaction times. The interfacial layer morphology was examined by SEM and high resolution SEM. TEM was also used to analyze interfacial reaction products, determine if any oxide remained at the Fe-Zn interface after galvanizing and identify the location of the oxide. In addition, the interfacial layer formation kinetics was determined using ICP.

### **5.2.1 Zn-0.20 wt% dissolved Al bath**

#### **5.2.1.1 SEM analysis of the interfacial layer**

The morphology of the interfacial layer as determined by Scanning Electron Microscopy (SEM) following selective stripping of the Zn overlay by 10 vol. %  $\text{H}_2\text{SO}_4$ , is shown in Figure 5.7 through Figure 5.10. It should be recalled that stripping the coating with 10 vol. %  $\text{H}_2\text{SO}_4$  will leave both the Fe-Al and Fe-Zn intermetallics intact. High resolution SEM was performed on selected samples subjected to the 2s immersion time (Table 4.2) to further investigate the fine Fe-Al interfacial layer microstructure, as shown in Figure 5.11.

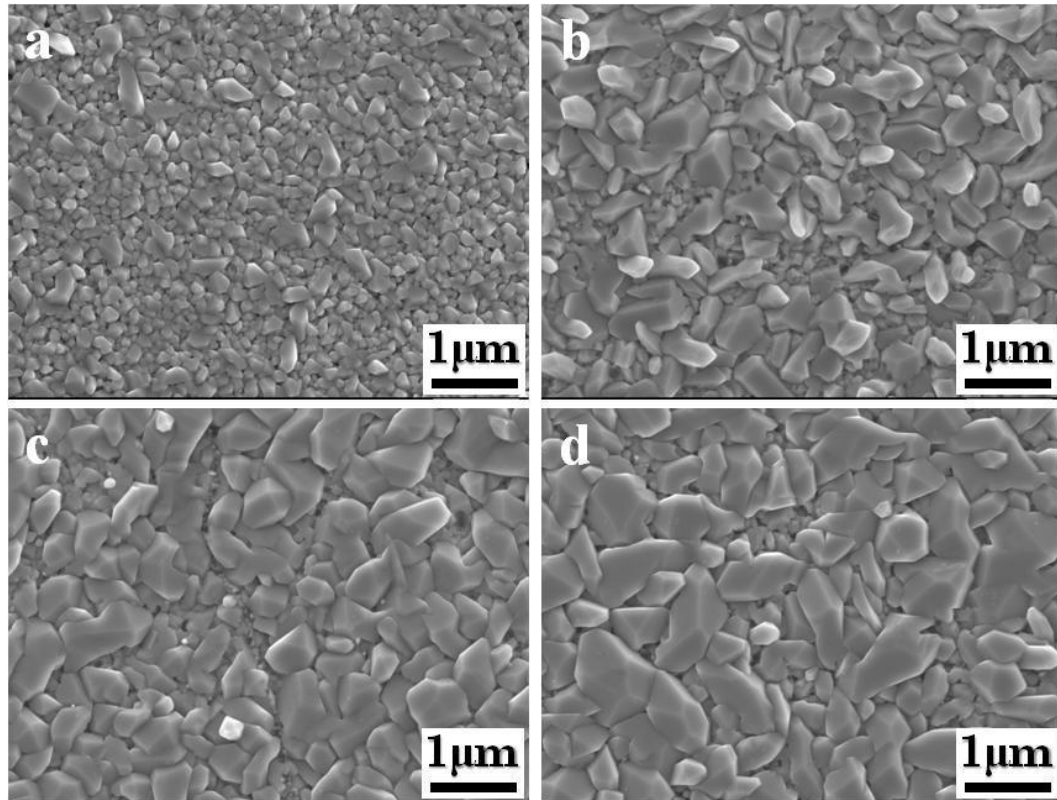


Figure 5.7: SEM micrographs of the Fe-Al interfacial layer for the 0.2Mn steel galvanized in a 0.20 wt% dissolved Al bath for reaction times of: a) 2.13s, b) 3.55s, c) 5.56s and d) 7.61s.

Figure 5.7 shows the microstructural evolution of the Fe-Al interfacial layer as a function of reaction time for the 0.2Mn steel. In fact, the interfacial layer morphology observed for the 0.2Mn steel is similar to that observed for IF steels (Guttman et al. 1995, Baril et al. 1999, Chen et al. 2008) and consists of a two-layer structure. At lower reaction times, as shown in Figure 5.7a, the lower layer comprised a continuous, compact layer of small (tens of nanometers) equiaxed crystals, whereas the upper layer formed at

higher reaction times (Figure 5.7(b-d) and Figure 5.11a) comprised coarse, non-compact, elongated crystals with some small embedded crystals.

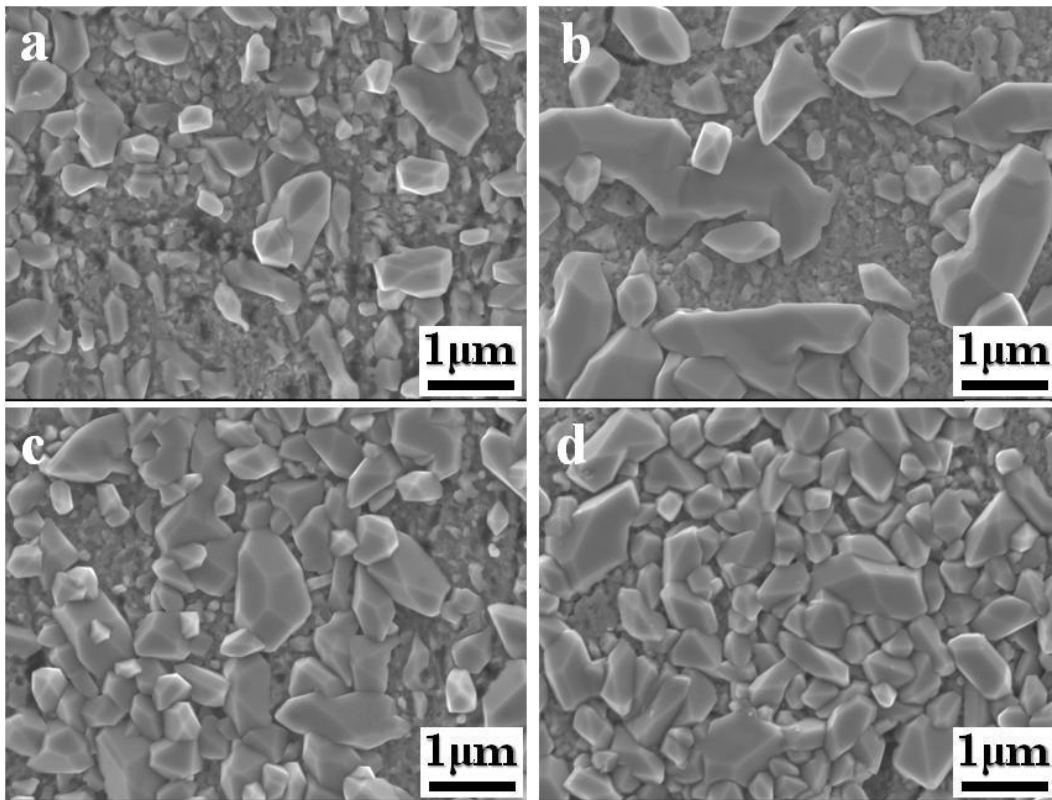


Figure 5.8: SEM micrographs of the Fe-Al interfacial layer for the 1.4Mn steel galvanized in a 0.20 wt% dissolved Al bath for reaction times of: a) 2.20s, b) 3.62s, c) 5.66s and d) 7.68s.

On the other hand, the structure of the Fe-Al interfacial layer on the higher Mn containing steels, as shown in Figure 5.8 through Figure 5.11, were not homogenous and consisted of a mixture of fine and coarse crystals, as previously reported by Li et al.

(2011) and Sagl et al. (2013). However, with increasing reaction time the number of fine Fe-Al crystals decreased and the interfacial layer exhibited a coarser and more compact morphology.

In addition, some “bare” areas were observed for the high Mn steels, particularly at shorter reaction times (Figure 5.8a, Figure 5.9a and Figure 5.10a). From Figure 5.11, it can be seen that the “bare” areas were actually a compact layer of very fine Fe-Al crystals, similar to the lower layer seen in Figure 5.7a.

In general, the 1.4Mn steel interfacial layer showed a coarser morphology as compared to that of the 2.5Mn and 3.0Mn steels. Also, for all reaction times, the interfacial layer formed on the higher Mn steels showed a less compact microstructure compared to that of the 0.2Mn steel. It should be noted that no Fe-Zn intermetallic were observed for all experimental steels.

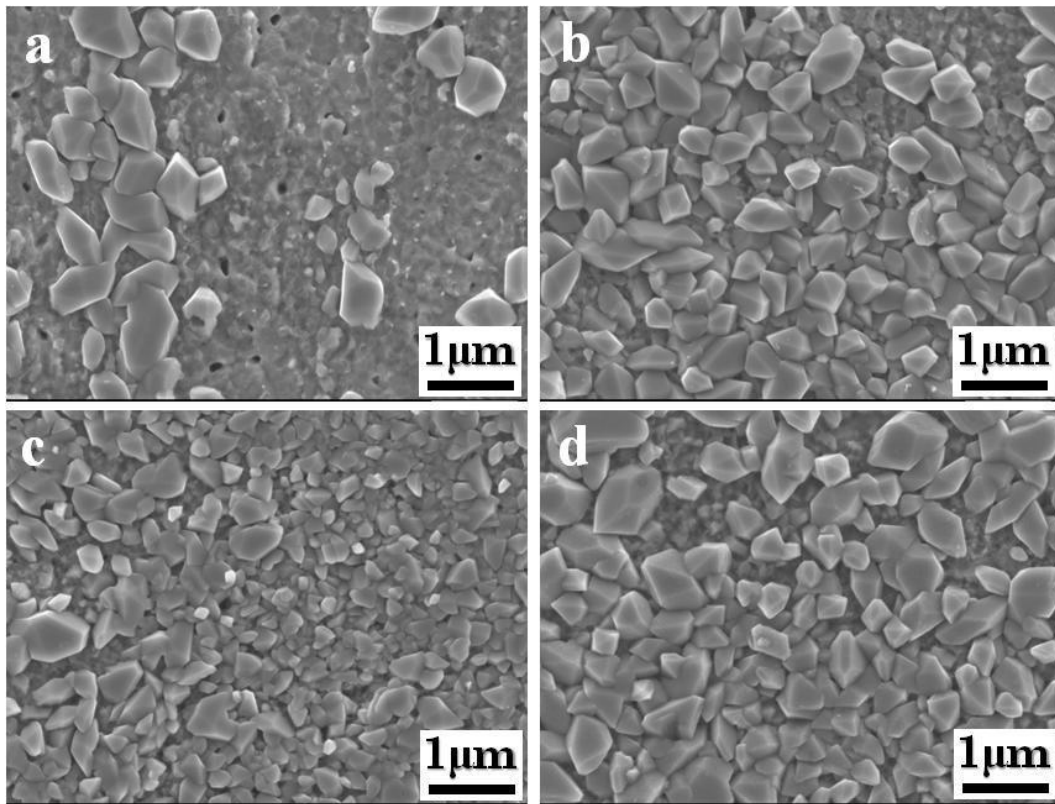


Figure 5.9: SEM micrographs of the Fe-Al interfacial layer for the 2.5Mn steel galvanized in a 0.20 wt% dissolved Al bath for reaction times of: a) 2.23s, b) 3.65s, c) 5.66s and d) 7.71s.

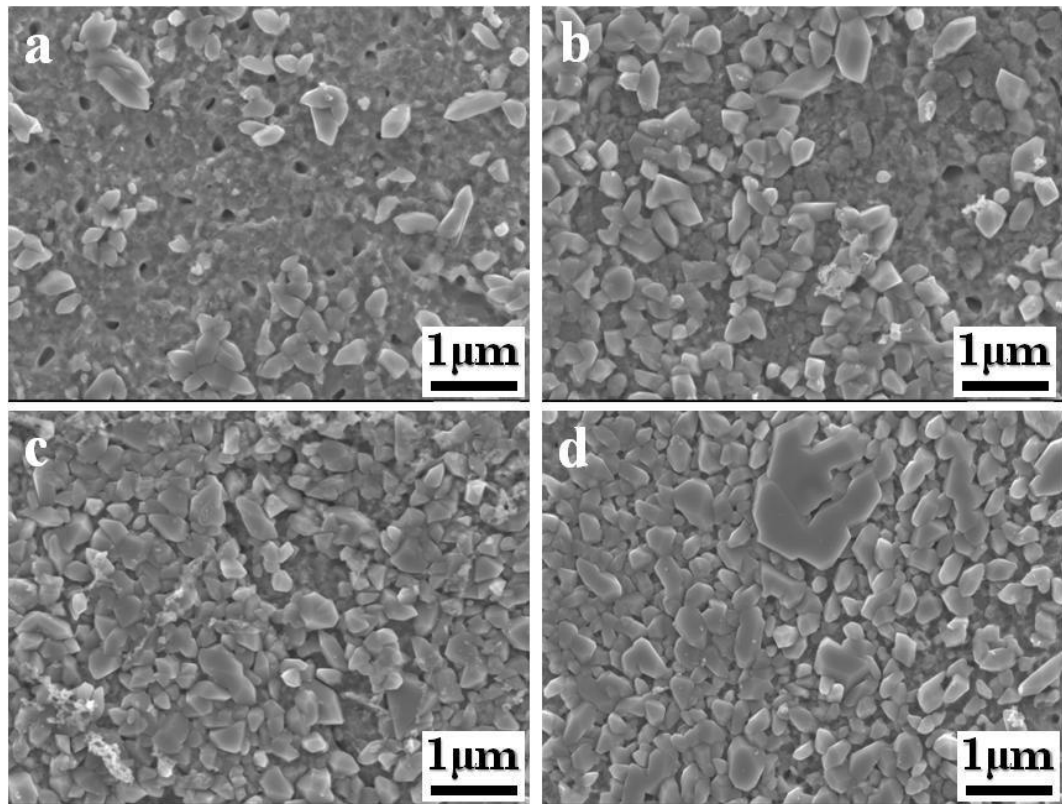


Figure 5.10: SEM micrographs of the Fe-Al interfacial layer for the 3.0Mn steel galvanized in a 0.20 wt% dissolved Al bath for reaction times of: a) 2.23s, b) 3.65s, c) 5.66s and d) 7.71s.

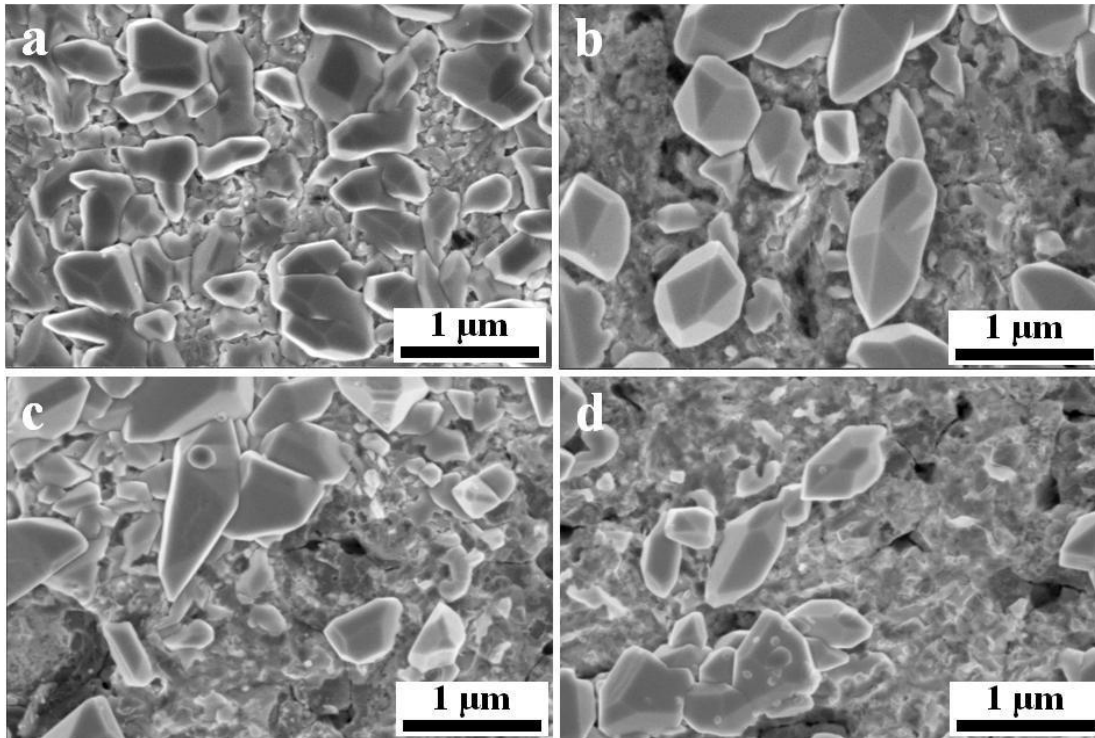


Figure 5.11: High resolution SEM images of the Fe-Al interfacial layer for the 0.20 wt% dissolved Al bath as a function of alloy Mn content and reaction time for a 2s immersion time: a) 0.2Mn-3.55s, b) 1.4Mn-3.62s, c) 2.5Mn-3.65s and d) 3.0Mn-3.65s.

### 5.2.1.2 TEM analysis of the steel/coating interface

Transmission electron microscopy (TEM) with energy dispersive X-ray (EDX) elemental mapping and quantitative point analysis were performed across the steel/zinc coating interface of selected samples to further investigate the interfacial layer and any residual oxide morphologies.

Figure 5.12 shows a TEM micrograph and EDX elemental mappings of the 0.2Mn steel galvanized for the 2.13s reaction time. The continuous, compact Al-rich layer at the Fe/Zn interface is the well developed Fe-Al interfacial layer, in consistent with the SEM image shown in Figure 5.7a. It should be noted that no Mn and O rich areas were detected and, therefore, no Mn and O maps are shown.

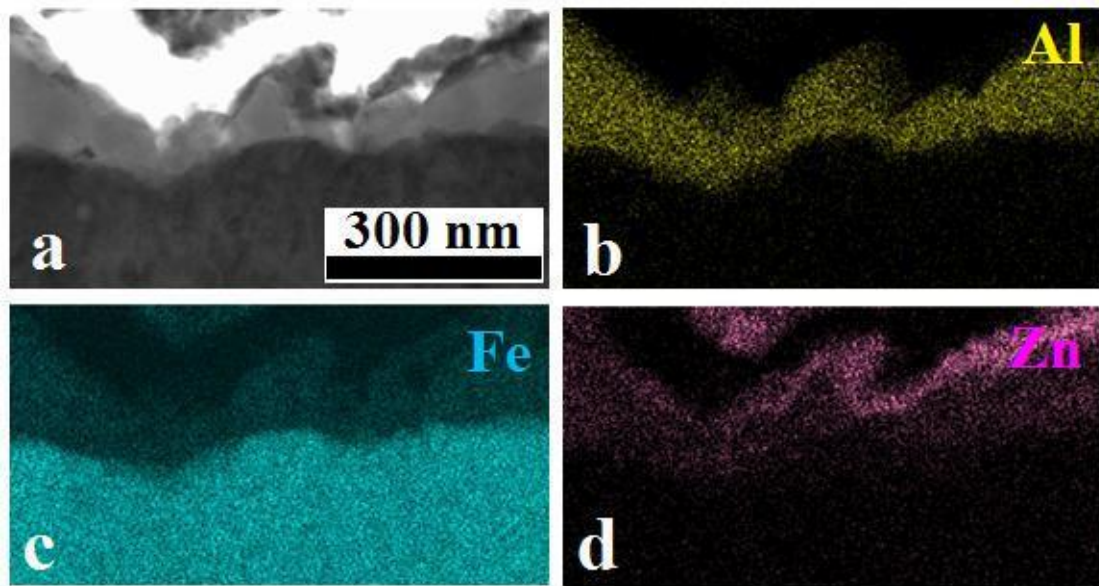


Figure 5.12: TEM micrograph and EDX mapping of the steel/coating interface for the 0.2Mn steel at 2.13s reaction time a) bright field image, b) Al, c) Fe and d) Zn maps.

On the other hand, TEM analysis of the cross-sections of the higher Mn steels showed that Mn rich grains remained at the Fe/Zn interface after galvanizing, as shown in Figure 5.13 through Figure 5.17. In fact, by increasing the steel Mn content, the thickness of the remained Mn-rich layer increased.

Figure 5.13 shows the TEM micrograph and EDX elemental mappings for the 1.4Mn steel and 2.20s reaction time. Quantitative point analyses of points A through D in Figure 5.13a are shown in Table 5.3. It should be mentioned that chemistry and morphology of determined phases are consistent with that reported by several authors (Baril and L'Esperance 1999, Chen et al. 2008, Bellhouse and McDermid 2010, 2011 and 2012, Sagl et al. 2013). It can be seen that, despite the presence of a Mn-rich layer at the steel surface (points A and B), a well developed Fe-Al interfacial layer formed at the steel/zinc interface. As shown by points C and D, fine and coarse morphologies of Fe/Al interfacial layer were observed consistent with SEM image in Figure 5.8a. Penetration of Zn(Al) liquid through the MnO layer and subsurface and resulting formation of Fe-Al layer below the MnO particles were observed, as shown by point D.

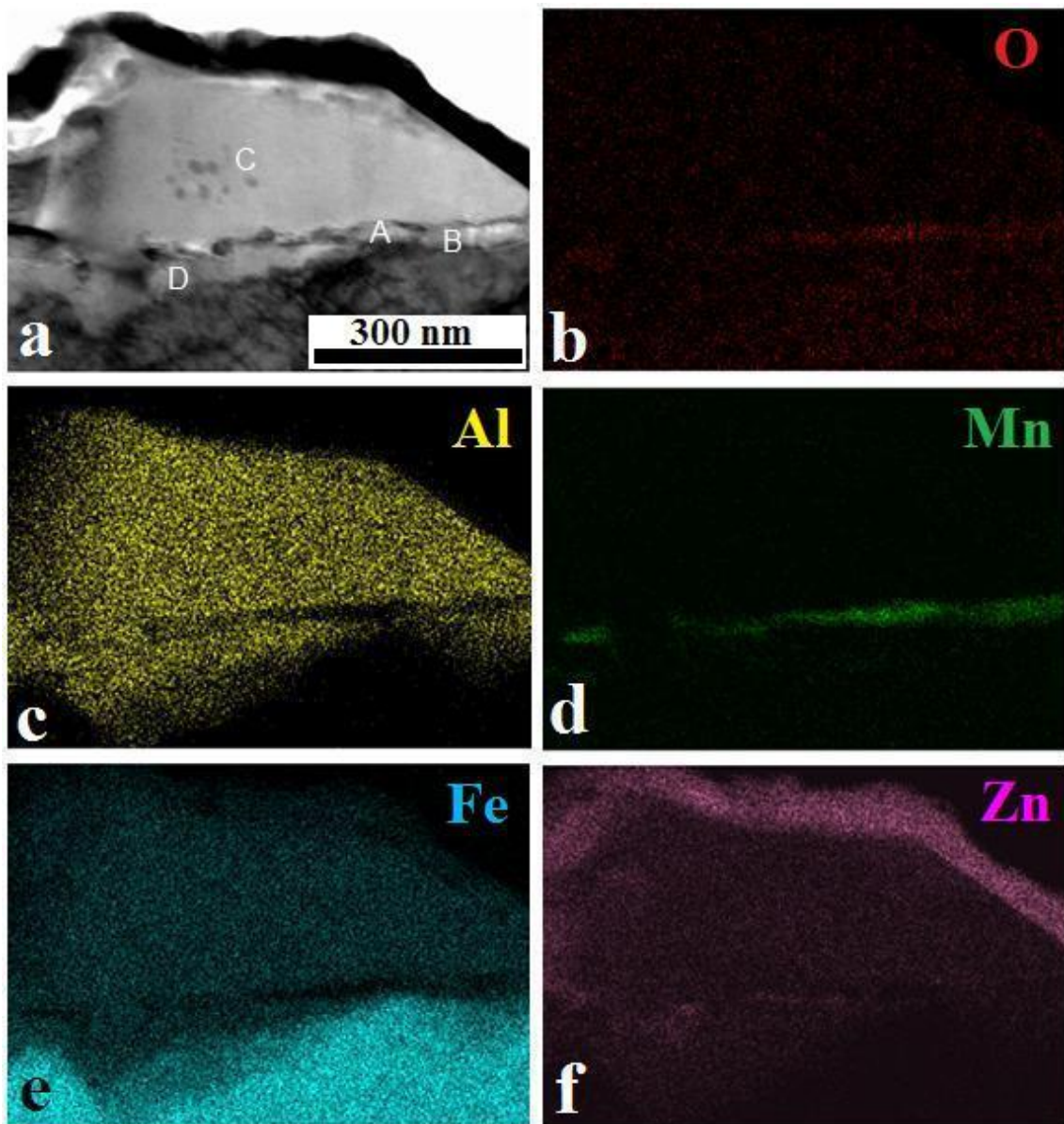


Figure 5.13: TEM micrograph and EDX mapping of the steel/coating interface for the 1.4Mn steel at 2.20s reaction time a) bright field image, b) Al, c) Fe and d) Zn maps.

Table 5.3: TEM-EDX point analyses for the 1.4Mn steel corresponding to the points indicated in Figure 5.13a (atomic%)

Point	O	Mn	Al	Fe	Zn	Phase Present
A	33.8	45.2	10.9	7.4	2.7	MnO <sub>x</sub>
B	20.5	22.0	33.4	15.5	8.6	MnO, Fe <sub>2</sub> Al <sub>5-x</sub> Zn <sub>x</sub>
C	6.4	0.1	54.4	27.4	11.7	Fe <sub>2</sub> Al <sub>5-x</sub> Zn <sub>x</sub>
D	6.2	1.5	53.3	26.2	12.8	Fe <sub>2</sub> Al <sub>5-x</sub> Zn <sub>x</sub>

TEM micrograph and EDX elemental mappings of two areas of the 2.5Mn and 3.0 Mn steels for 2.23s reaction time are shown in Figure 5.14 through Figure 5.17. Quantitative analyses of points A through J are provided in Table 5.4. It can be seen that a significant Mn-rich layer remained at the Fe/Zn interface after galvanizing, as shown by points A and F through I. Al-rich grains confirmed the presence of the Fe-Al interfacial layer (points B, C, G and J) as well as some gaps as previously observed in the SEM images (Figure 5.9a and Figure 5.10a). Discontinuities in the Al-rich layer can be attributed to a continuous and thick MnO layer (points A and F) which prevented good reactive wetting and the formation of interfacial layer. However, it can be seen that any discontinuity present in the MnO layer resulted in Fe-Al interfacial layer nucleation and growth (points C, E and J). In fact, in some areas Fe-Al crystals are observed inside or below the MnO layer due to the penetration of liquid Zn(Al) through the MnO, as shown by points B, C, D and G.

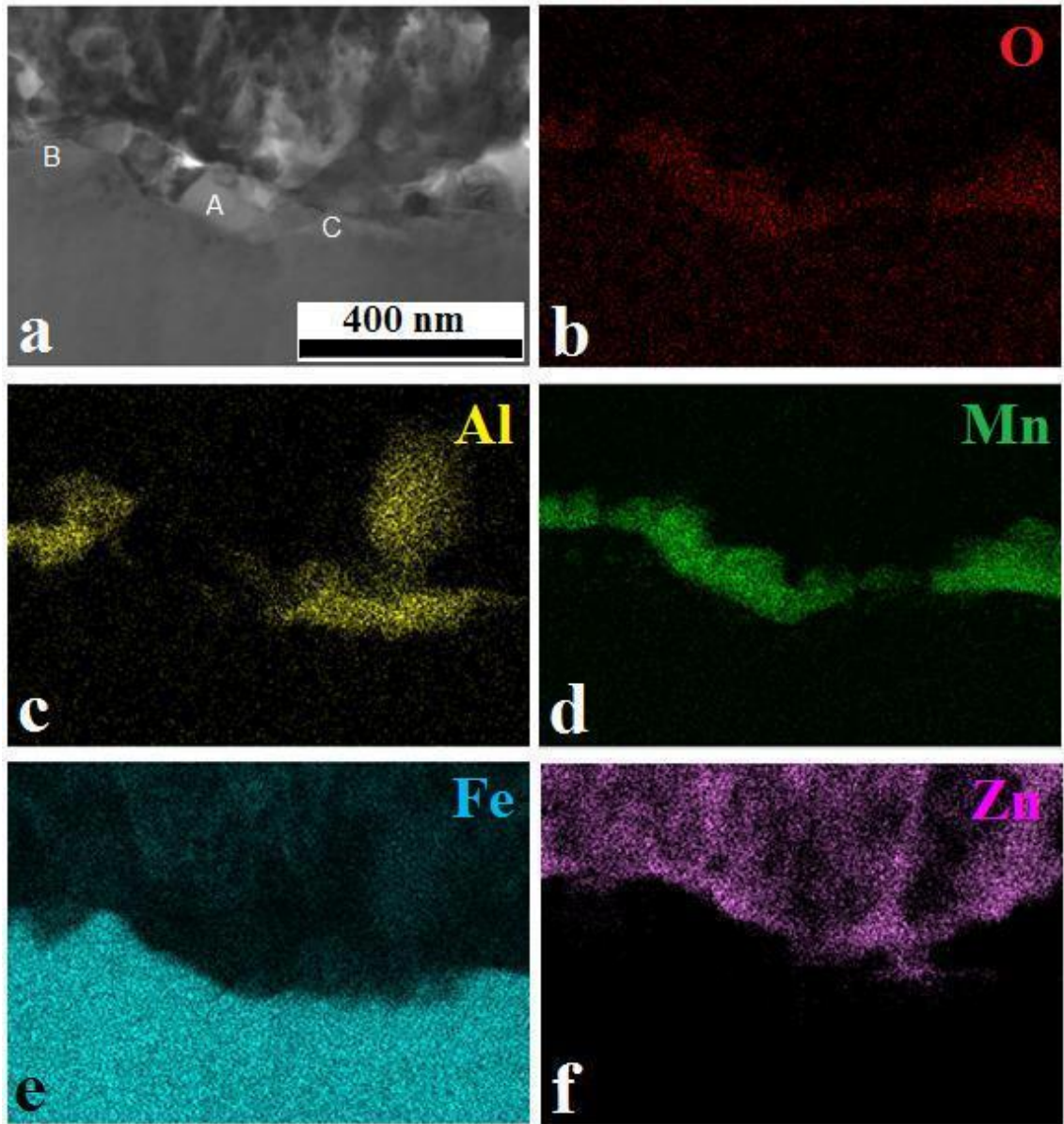


Figure 5.14: TEM micrograph and EDX mapping of the steel/coating interface for the 2.5Mn steel at 2.23s reaction time a) bright field image, b) Al, c) Fe and d) Zn maps.

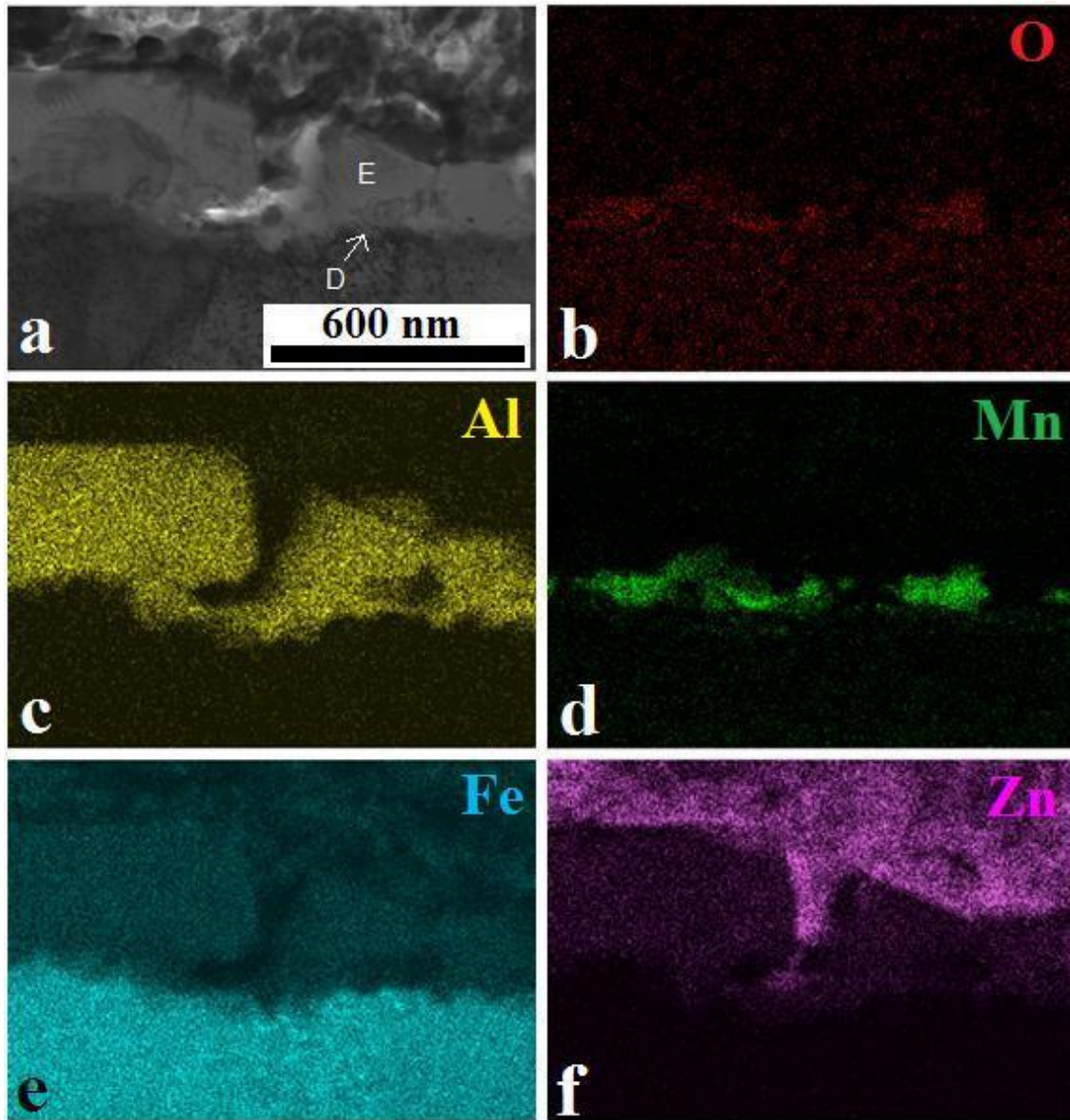


Figure 5.15: TEM micrograph and EDX mapping of the steel/coating interface for the 2.5Mn steel at 2.23s reaction time a) bright field image, b) Al, c) Fe and d) Zn maps.

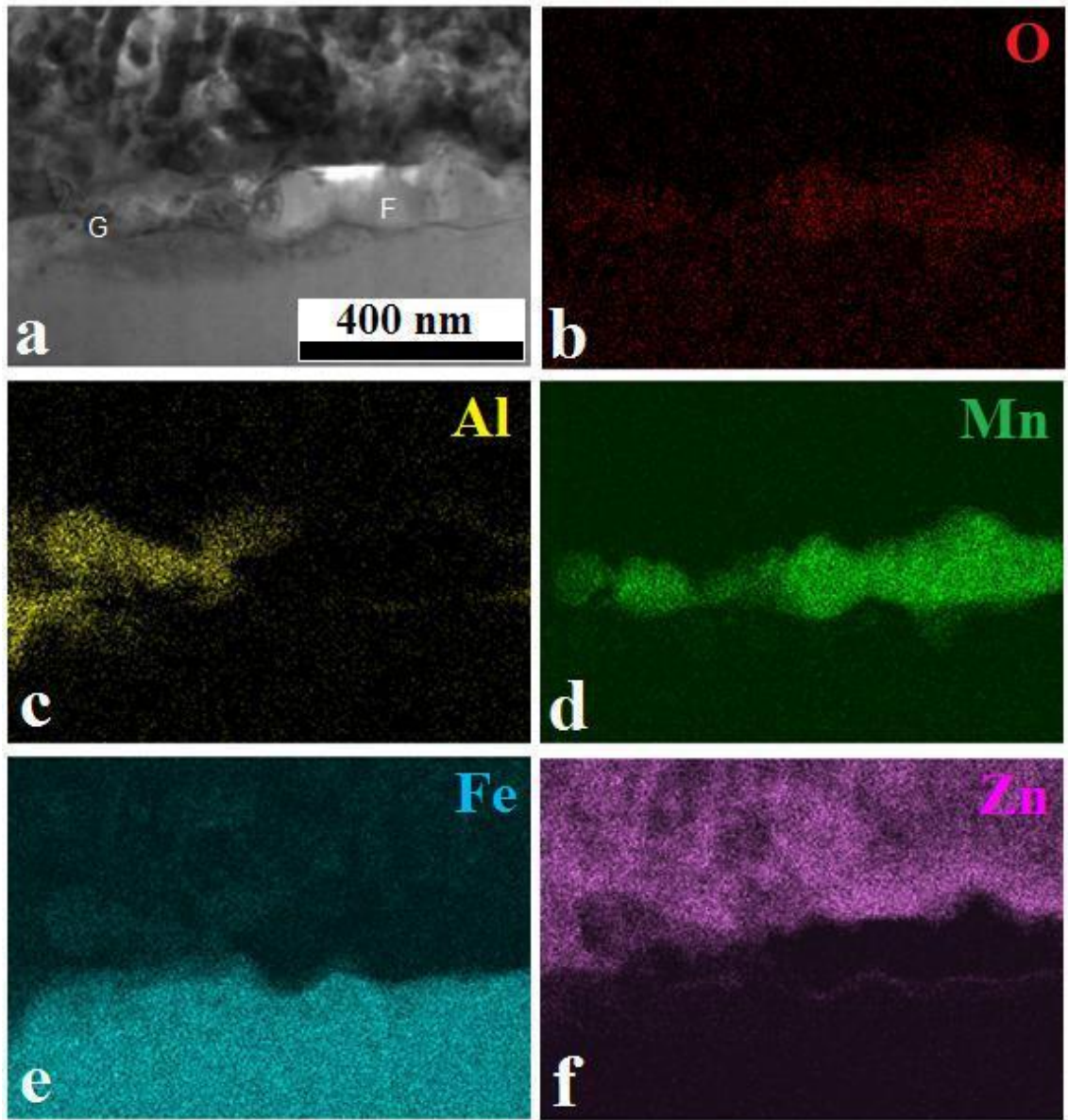


Figure 5.16: TEM micrograph and EDX mapping of the steel/coating interface for the 3.0Mn steel at 2.23s reaction time a) bright field image, b) Al, c) Fe and d) Zn maps.

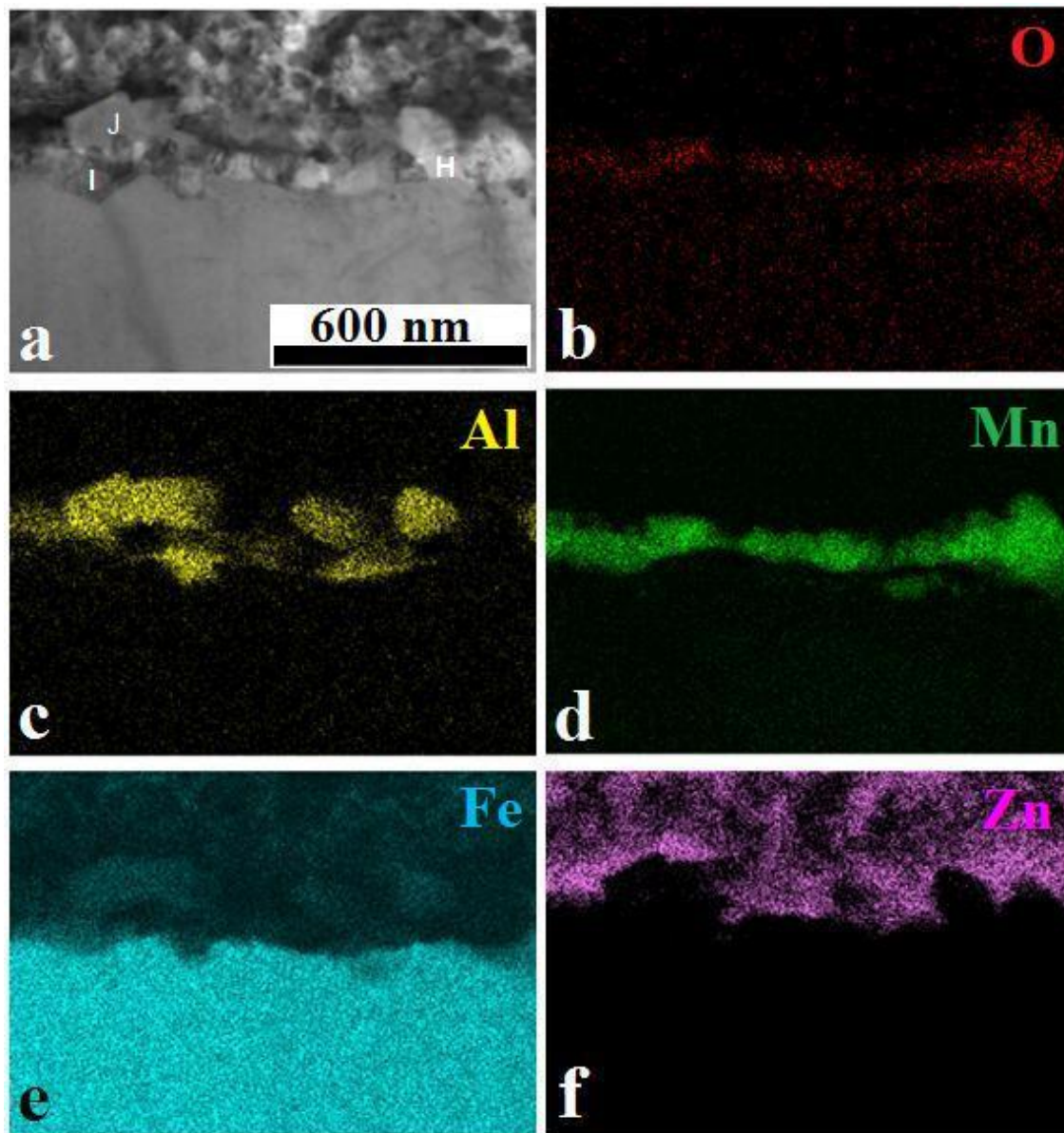


Figure 5.17: TEM micrograph and EDX mapping of the steel/coating interface for the 3.0Mn steel at 2.23s reaction time a) bright field image, b) Al, c) Fe and d) Zn maps.

Table 5.4: TEM-EDX point analysis of the 2.5Mn and 3.0Mn steels corresponding to the points indicated in Figure 5.14a through Figure 5.17a (atomic%)

Point	O	Mn	Al	Fe	Zn	Phase Present
A	34.5	62.6	0.6	2.0	0.3	MnO <sub>x</sub>
B	3.1	3.1	50.4	28.5	14.9	MnO, Fe <sub>2</sub> Al <sub>5-x</sub> Zn <sub>x</sub>
C	3.6	0.4	52.3	29.3	14.4	Fe <sub>2</sub> Al <sub>5-x</sub> Zn <sub>x</sub>
D	16.4	27.8	33.7	16.8	5.3	MnO <sub>x</sub> , Fe <sub>2</sub> Al <sub>5-x</sub> Zn <sub>x</sub>
E	2.9	0.0	57.1	29.1	10.9	Fe <sub>2</sub> Al <sub>5-x</sub> Zn <sub>x</sub>
F	32.1	65.9	0.2	1.8	0.0	MnO <sub>x</sub>
G	16.1	35.9	9.0	34.6	4.4	MnO <sub>x</sub> , Fe (Substrate)
H	33.6	63.3	0.3	2.5	0.3	MnO <sub>x</sub>
I	18.0	32.5	2.8	46.3	0.3	MnO <sub>x</sub> , Fe (Substrate)
J	2.6	0.1	50.5	30.2	16.6	Fe <sub>2</sub> Al <sub>5-x</sub> Zn <sub>x</sub>

### 5.2.1.3 ICP analysis of the Fe-Al interfacial layer

The interfacial layer Al uptake as a function of reaction time and steel Mn content was assessed by dissolving the interfacial layer in an inhibited 10% H<sub>2</sub>SO<sub>4</sub> solution after stripping the Zn overlay using fuming nitric acid and analysing the obtained solution using ICP (Figure 5.18). The Al uptake is expressed in units of mg(Al)/m<sup>2</sup> of substrate. In this case the error bars represent the 95% confidence interval on the average interfacial layer Al uptake obtained from repeated analyses. The interfacial layer Al-uptake was found to increase with increasing reaction time for all experimental steels. Also, despite the selective oxidation of Mn on the 1.4Mn steel surface, the highest interfacial layer Al uptake was observed for the 1.4Mn steel for all reaction times. In fact, the Al uptake for

the 1.4Mn steel was higher versus the 0.2Mn steel, followed by a decline for the higher Mn content steels such that the lowest Al uptake was observed for the 3.0Mn steel.

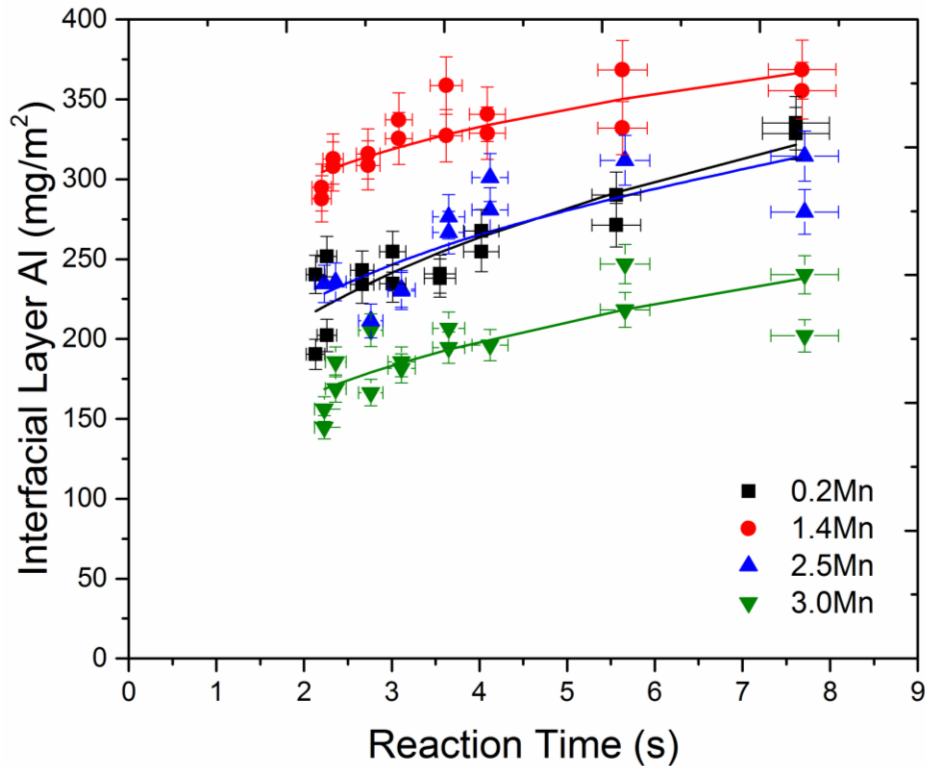


Figure 5.18: Interfacial layer Al-uptake as a function of reaction time and steel Mn content for a 0.20wt% dissolved Al bath.

It can be further seen that the majority of Al uptake took place within a reaction time of less than 2s, indicative of rapid interfacial layer formation. After this time, the interfacial layer Al content increased non-parabolically, corresponding to mixed diffusion-controlled growth. These results are consistent with the two-stage mechanism of

inhibition layer formation advocated by several authors (Guttman 1994, Tang 1995, Toussaint et al. 1998, Giorgi et al. 2005, Chen et al. 2008, Dutta et al. 2009): (i) nucleation and lateral growth of the Fe-Al intermetallic layer at the steel/bath interface, which occurs rapidly with a high rate of Al uptake and is completed when the substrate surface is completely covered by Fe-Al intermetallics and (ii) diffusion controlled growth of the interfacial layer which corresponds to a lower rate of Al uptake and occurs by diffusion of Fe from the substrate through the interfacial layer and diffusion of Al through the Zn bath. It is worth noting that the flux of Fe through the interfacial layer is the rate-limiting step in the growth process.

A power-law growth equation (equation 5.1) was used to fit the interfacial layer Al uptake data in Figure 5.18 such that:

$$Y = K.t^n \quad (5.1)$$

where  $Y$  is the Al uptake of the interfacial layer ( $\text{mg}/\text{m}^2$ ),  $K$  the growth rate constant,  $t$  the reaction time and  $n$  the time exponent. It should be noted that the initial interfacial layer formation steps, including any incubation period and nucleation, were not experimentally captured in this study and only growth kinetics were determined.

The value of  $n$  depends on the structure and growth mode of the inhibition layer. For example, bulk diffusion-controlled growth is characterized by  $n=0.5$  (*i.e.* parabolic growth). However, a rate-controlling mechanism of mixed bulk and grain boundary

diffusion of Fe from the substrate through the Fe-Al interfacial layer resulted in the value of  $n$  being less than 0.5 (Chen et al. 2008). As shown in Table 5.5, the range of values determined for the time exponent,  $n$ , was between 0.15 to 0.31 for the experimental alloys, indicating that the Fe-Al layer growth was mixed-mode Fe mass transport controlled through the interfacial layer.

The high  $K$  and low  $n$  values for the 1.4Mn steel (Table 5.5) indicate an initial fast growth followed by solid-state dominated diffusion-controlled growth at longer reaction times, which is in qualitative agreement with the interfacial layer morphology of the 1.4Mn steel (Figure 5.8). The higher  $n$  values for 2.5Mn and 3.0Mn steels versus the 1.4Mn steel can be explained by higher Fe diffusion through the non-compact and thin Fe-Al interfacial layer observed at the lower reaction times (Figure 5.9 and Figure 5.10).

Table 5.5: Growth rate equation (5.1) parameters for interfacial layer in 0.20 wt% Al bath

Alloy Name	$K$	Standard Error	$n$	Standard Error	$R^2$
0.2Mn	171.1	9.3	0.31	0.04	0.80
1.4Mn	272.4	9.3	0.15	0.02	0.70
2.5Mn	188.7	16.5	0.25	0.06	0.60
3.0Mn	137.4	10.7	0.26	0.05	0.62

## **5.2.2 Zn-0.30 wt% dissolved Al bath**

### **5.2.2.1 SEM analysis of the interfacial layer**

The morphology and the microstructural evolution of the Fe-Al interfacial layer as a function of time were studied by SEM, as shown in Figure 5.19 through Figure 5.22. High resolution SEM was also performed on samples subjected to a 2s immersion time (Table 4.2) to investigate in detail the fine Fe-Al interfacial layer microstructure, as shown in Figure 5.23.

It can be seen that at short reaction times the interfacial layer morphology was composed of fine, equiaxed crystals, whereas the interfacial layer formed at longer reaction times had a coarse, non-compact morphology with some embedded fine crystals. In addition, some “bare” areas composed of very fine Fe-Al crystals were observed for the 2.5Mn and 3.0Mn steels at shorter reaction times (Figure 5.21(a,b), Figure 5.22(a,b) and Figure 5.23(c,d)). However, with increasing reaction time the number of fine Fe-Al crystals decreased and the upper interfacial layer comprised coarser Fe-Al crystals (Figure 5.21(c,d) and Figure 5.22(c,d)).

In general, increasing the dissolved Al bath to 0.30 wt% resulted in a significantly finer and more compact Fe-Al interfacial layer microstructure for all the experimental steels and reaction times (Figure 5.19 through Figure 5.23) when compared to the equivalent 0.20 wt% dissolved Al bath samples (Figure 5.7 through Figure 5.11). Specifically, in the case of the higher Mn steels (i.e. 1.4Mn, 2.5Mn and 3.0Mn steels),

increasing the bath Al content resulted in a homogenous and much finer interfacial layer morphology.

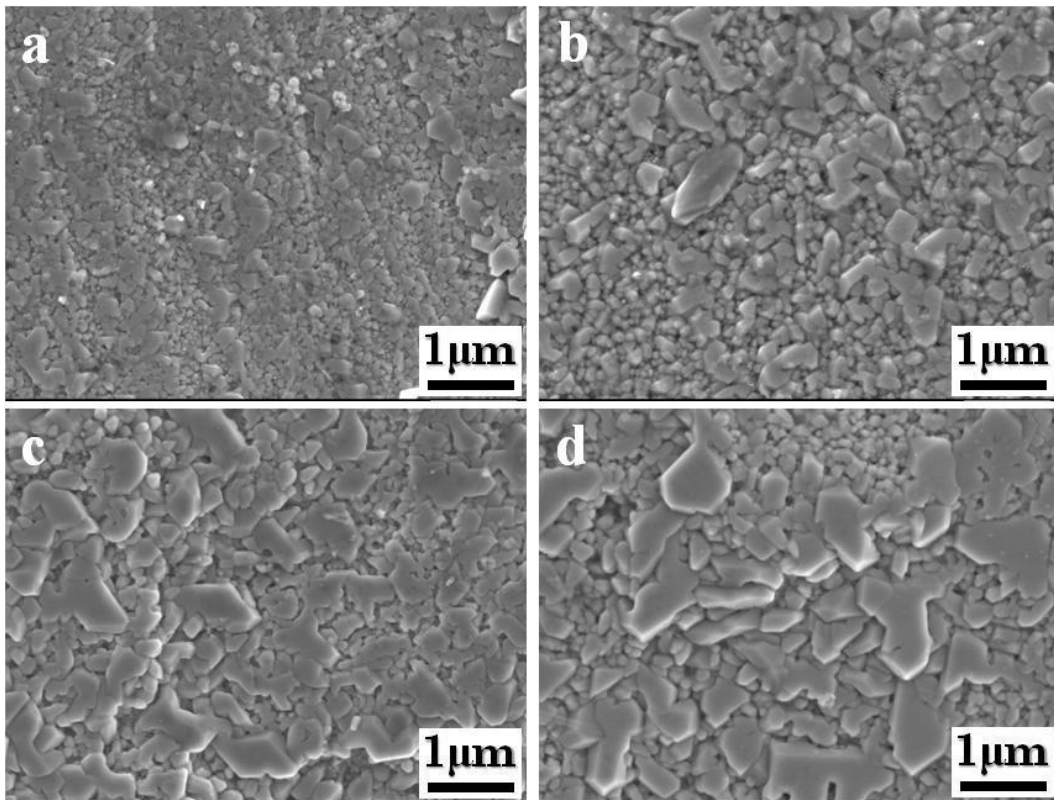


Figure 5.19: SEM micrographs of the Fe-Al interfacial layer for the 0.2Mn steel galvanized in a 0.30 wt% dissolved Al bath for reaction times of: a) 2.13s, b) 3.55s, c) 5.56s and d) 7.61s.

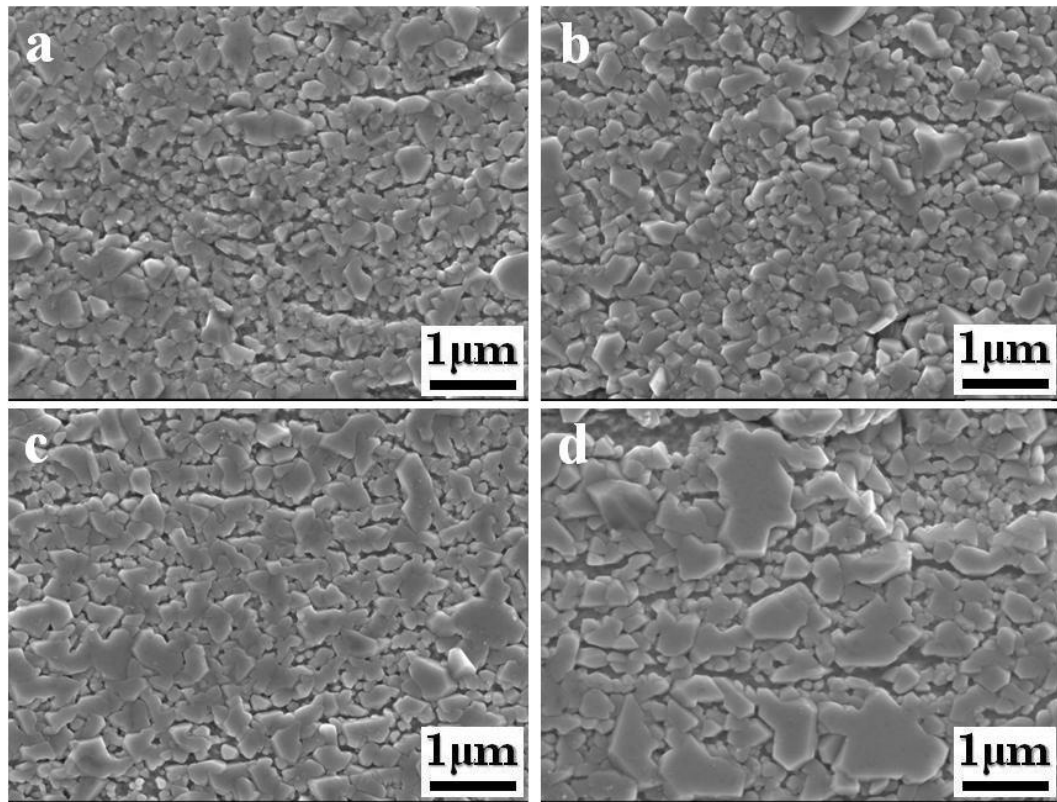


Figure 5.20: SEM micrographs of the Fe-Al interfacial layer for the 1.4Mn steel galvanized in a 0.30 wt% dissolved Al bath for reaction times of: a) 2.20s, b) 3.62s, c) 5.66s and d) 7.68s.

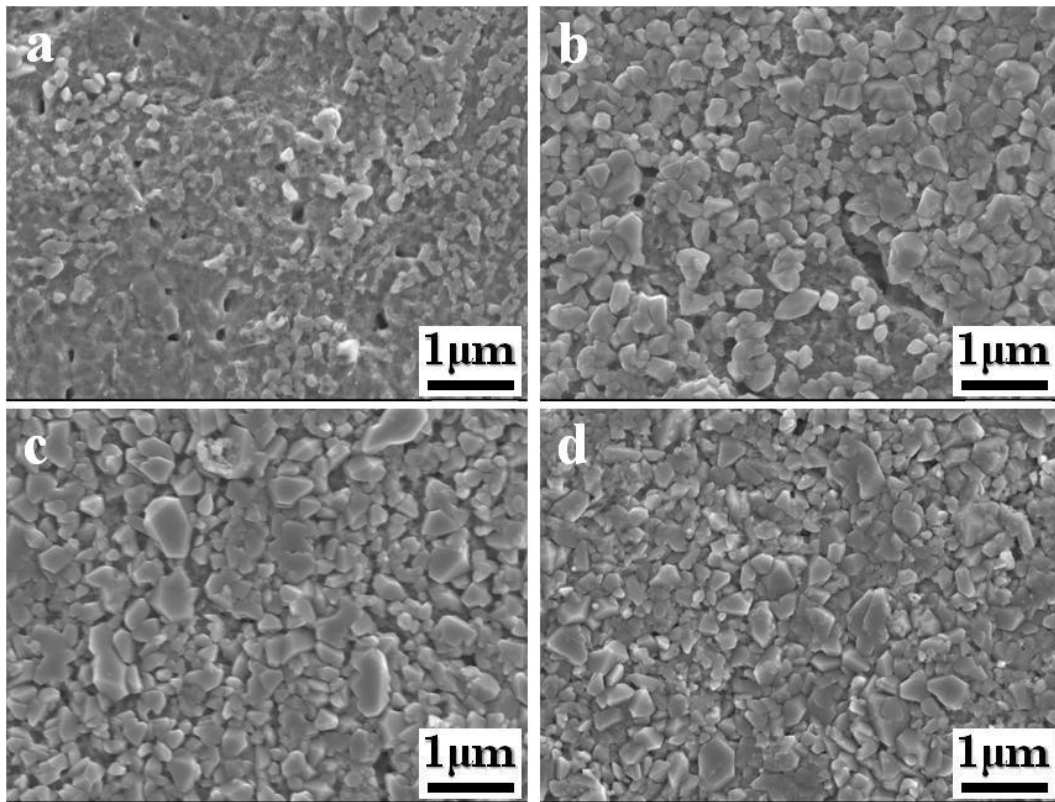


Figure 5.21: SEM micrographs of the Fe-Al interfacial layer for the 2.5Mn steel galvanized in a 0.30 wt% dissolved Al bath for reaction times of: a) 2.23s, b) 3.65s, c) 5.66s and d) 7.71s.

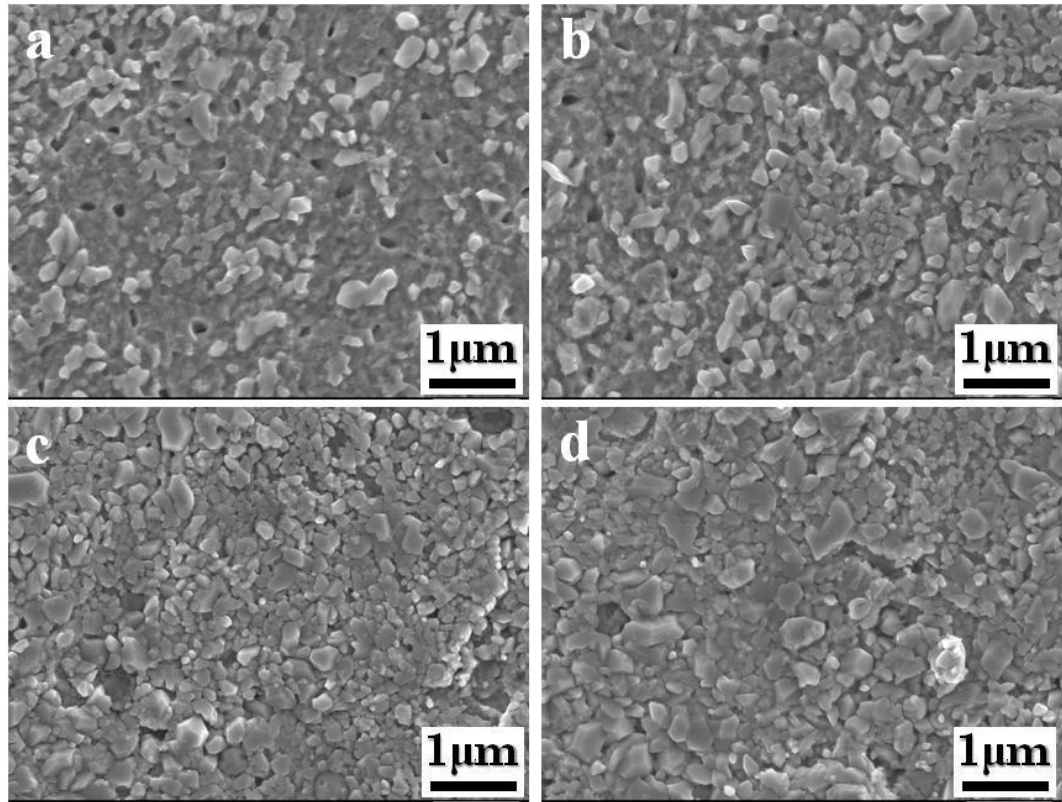


Figure 5.22: SEM micrographs of the Fe-Al interfacial layer for the 3.0Mn steel galvanized in a 0.30 wt% dissolved Al bath for reaction times of: a) 2.23s, b) 3.65s, c) 5.66s and d) 7.71s.

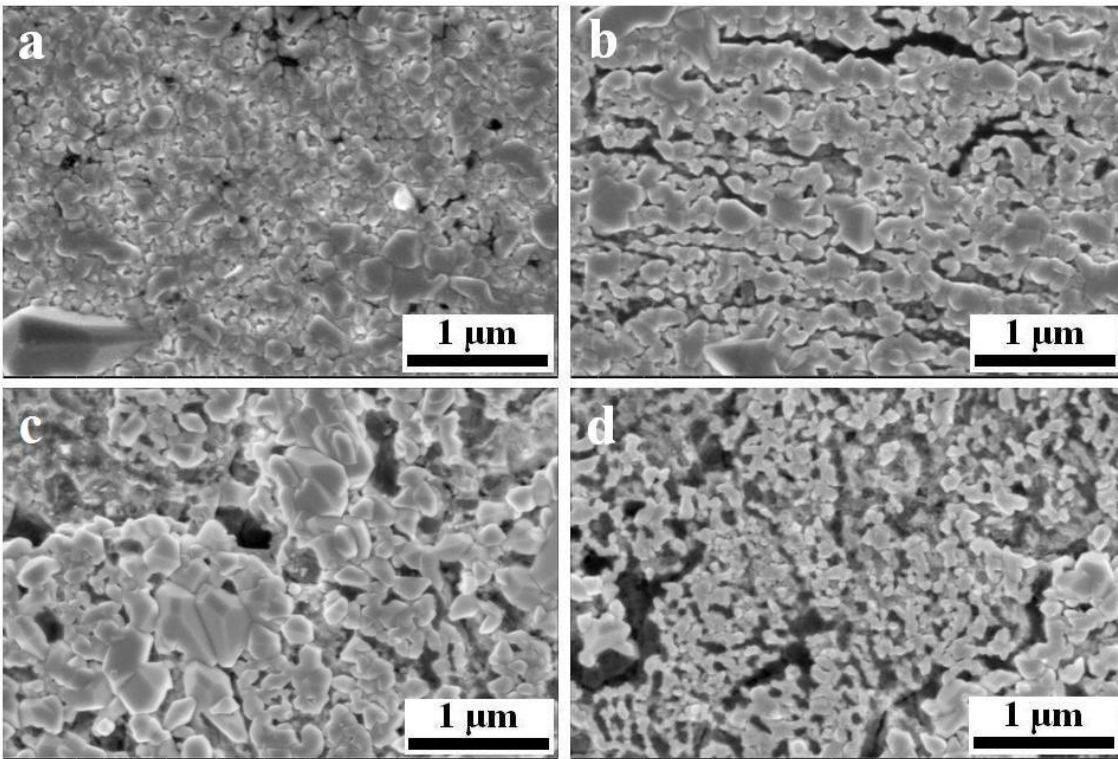


Figure 5.23: High resolution SEM images of the Fe-Al interfacial layer for the 0.30 wt% dissolved Al bath as a function of alloy Mn content and reaction time for a 2s immersion time: a) 0.2Mn-3.55s, b) 1.4Mn-3.62s, c) 2.5Mn-3.65s and d) 3.0Mn-3.65s.

#### 5.2.2.2 TEM analysis of the steel/coating interface

TEM and quantitative analyses of the 1.4Mn steel for the 2.20s reaction time are shown in Figure 5.24 and Table 5.6, respectively. Compared to the TEM analysis of the 1.4Mn steel galvanized in the 0.20 wt% Al bath (Figure 5.13), the Fe-Al interfacial layer was homogenous, thinner and more compact and composed of smaller Fe-Al crystals (points A and B), in agreement with SEM images (Figure 5.8 and Figure 5.20). Also, the

Mn-rich layer is not continuous and is composed of sparse MnO particles (Figure 5.24d) surrounded by Fe-Al crystals, as shown by points A and B. Also, comparison of the Mn, Al and Fe maps (Figure 5.24(c,d,e)) shows the flaking of MnO particles due to the Fe-Al interfacial layer growth below them, as previously reported by Bellhouse et al. (2011) and Sagl et al. (2013).

TEM micrograph and EDX elemental maps of the 2.5Mn steel galvanized for a 2.23s reaction time is shown in Figure 5.25 and quantitative analyses of points C through E in Figure 5.25a is shown in Table 5.6. It can be seen that a significant Mn rich layer remained at the steel substrate/zinc coating interface after galvanizing (Figure 5.25d).

For the 2.5Mn steel galvanized for a 7.71s reaction time in the 0.30 wt% Al bath, the TEM sample (Figure 5.26) was made after removing the zinc layer using inhibited 10 vol.% H<sub>2</sub>SO<sub>4</sub> as the Zn layer was too thick for TEM sample preparation by FIB. Quantitative analyses of points F through H in Figure 5.26a are shown in Table 5.6. A well developed, continuous two-layer interfacial layer comprised of fine (point F) and coarse (point G) Fe-Al crystals was observed at the steel/zinc interface, as shown in Figure 5.26c. In addition, the penetration of the liquid bath along the oxide/substrate interface and along grain boundaries was observed (Figure 5.26f). As shown by the Mn map in Figure 5.26d, regardless of some Mn oxide particles at the subsurface and grain boundaries (point H) no significant Mn-rich grains were observed at the Fe/Zn interface, which can be attributed to aluminothermic reduction (equation 2.8).

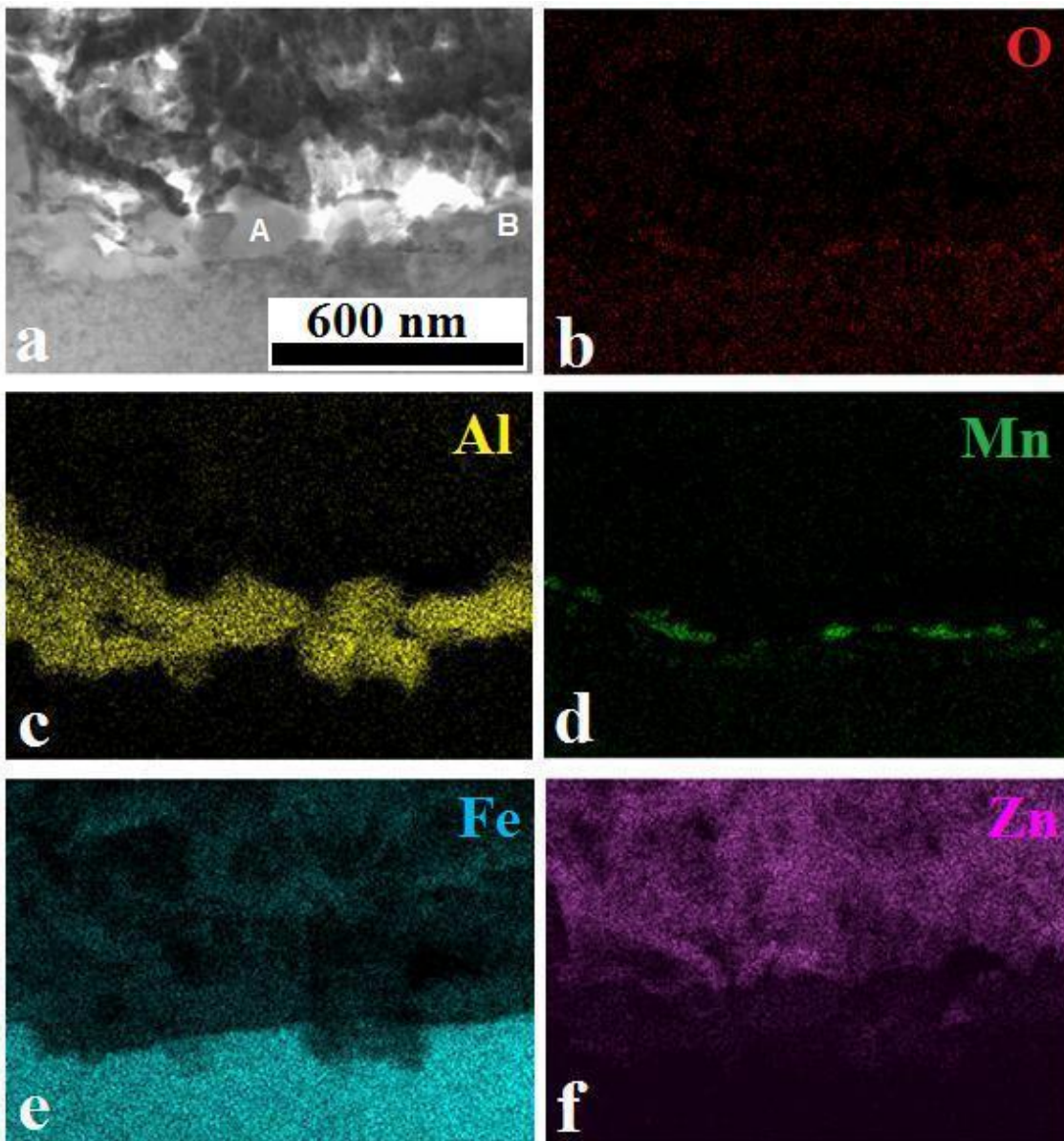


Figure 5.24: TEM micrograph and EDX mapping of the steel/coating interface for the 1.4Mn steel at 2.20s reaction time a) bright field image, b) Al, c) Fe and d) Zn maps.

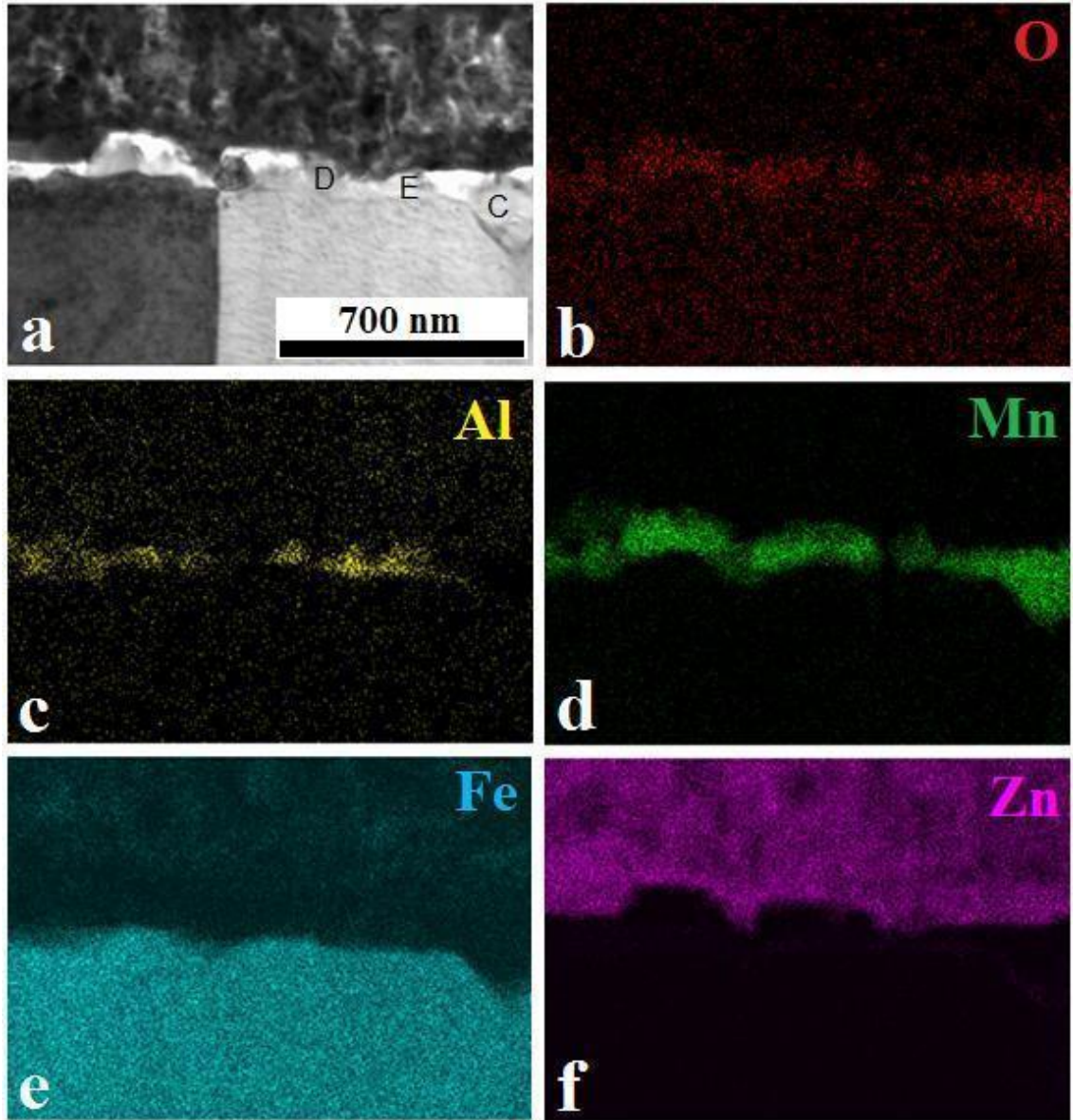


Figure 5.25: TEM micrograph and EDX mapping of the steel/coating interface for the 2.5Mn steel at 2.23s reaction time a) bright field image, b) Al, c) Fe and d) Zn maps.

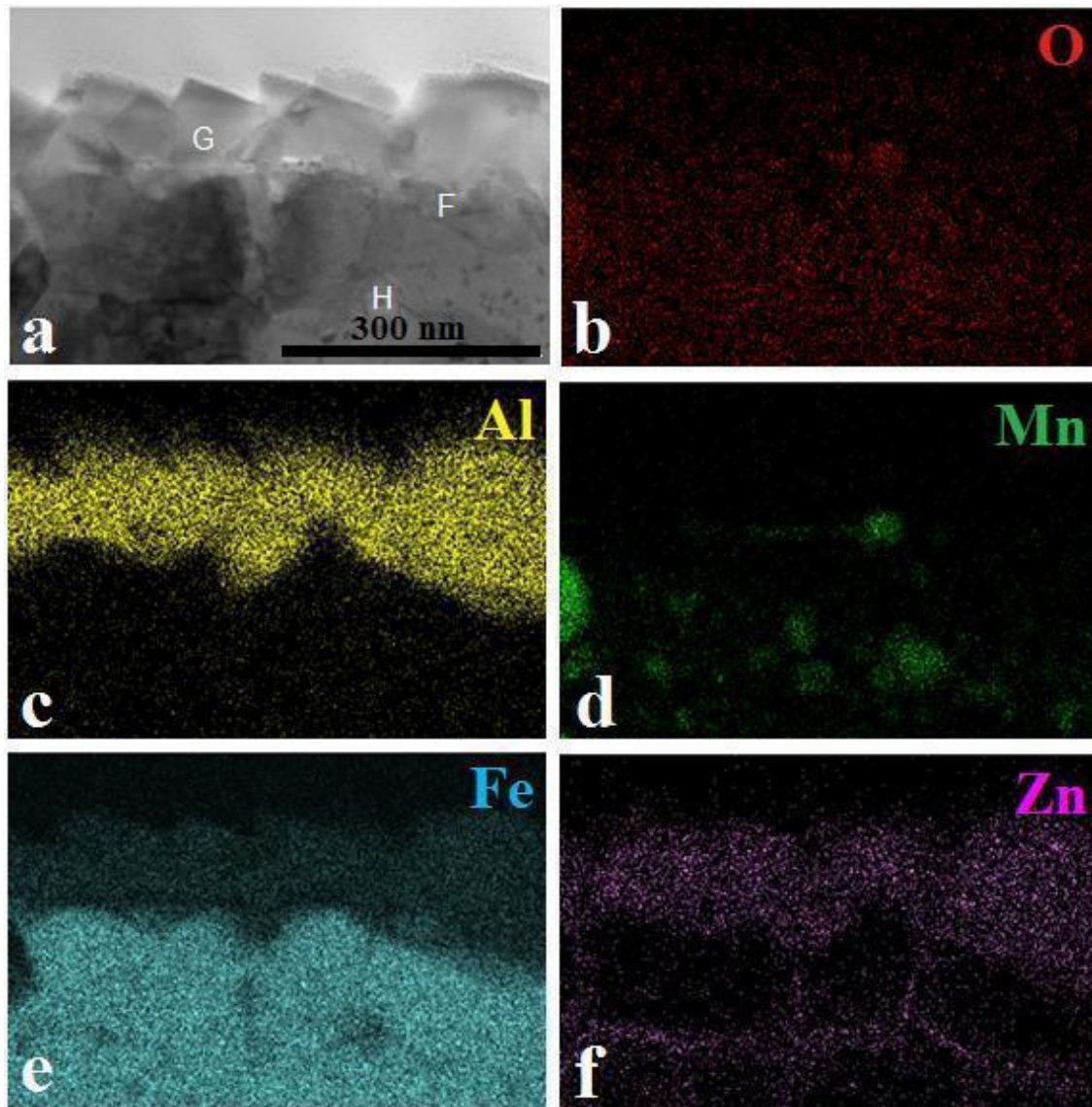


Figure 5.26: TEM micrograph and EDX mapping of the steel/coating interface for the 2.5Mn steel at 7.71s reaction time a) bright field image, b) Al, c) Fe and d) Zn maps.

Table 5.6: TEM-EDX point analysis of the 1.4Mn and 2.5Mn steels corresponding to the points indicated in Figure 5.24a through Figure 5.26a (atomic%)

Point	O	Mn	Al	Fe	Zn	Phase Present
A	2.0	0.0	52.3	30.1	15.6	$\text{Fe}_2\text{Al}_{5-x}\text{Zn}_x$
B	2.2	0.0	60.4	28.8	8.6	$\text{Fe}_2\text{Al}_{5-x}\text{Zn}_x$
C	31.4	65.9	0.0	2.3	0.4	$\text{MnO}_x$
D	25.0	72.4	0.3	2.0	0.3	$\text{MnO}_x$
E	16.9	23.2	37.9	19.7	8.3	$\text{MnO}_x, \text{Fe}_2\text{Al}_{5-x}\text{Zn}_x$
F	2.5	0.1	65.1	28.1	4.2	$\text{Fe}_2\text{Al}_{5-x}\text{Zn}_x$
G	9.7	0.1	58.2	27.7	4.3	$\text{Fe}_2\text{Al}_{5-x}\text{Zn}_x$
H	31.7	18.8	0.5	45.1	3.9	$\text{MnO}_x, \text{Fe}$ (Substrate)

### 5.2.2.3 ICP analysis of the Fe-Al interfacial layer

The interfacial layer Al uptake in the case of the 0.30 wt% dissolved Al bath (Figure 5.27) showed several significantly different trends when compared to the 0.20 wt% dissolved Al bath (Figure 5.18). As was the case for the 0.20 wt% Al bath, by increasing the reaction time the interfacial layer Al-uptake increased for all experimental steels. Nevertheless, increasing the dissolved Al bath resulted in lower Al uptake for the 0.2Mn and 1.4Mn steels for all reaction times. Lower interfacial layer Al uptake is previously reported for low alloyed steels and bath Al content higher than 0.20 wt% (Isobe 1992, Toussaint et al. 1998, Liu and Tang 2004), as discussed in §2.4.3.2. By contrast, the higher Mn substrates (2.5Mn and 3.0Mn steels) exhibited significantly higher Al uptake, particularly for longer reaction times. In fact, despite the significant

surface Mn segregation observed for the 2.5Mn and 3.0Mn steels (Figure 5.2), a higher Al uptake was observed for the 2.5Mn and 3.0Mn steels versus the 0.2Mn and 1.4Mn steels.

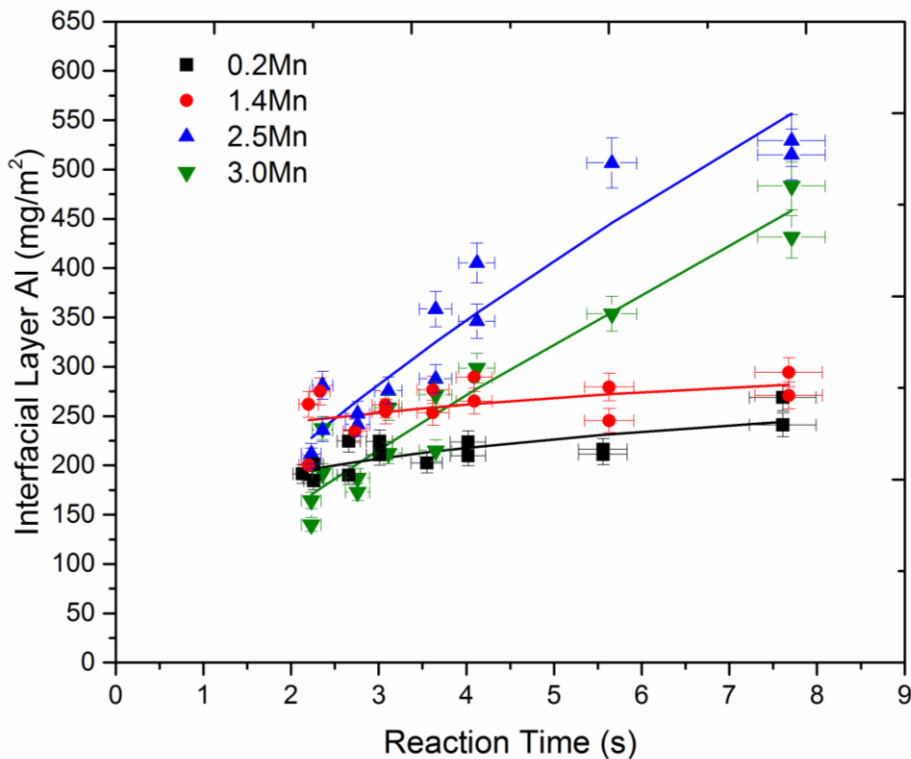


Figure 5.27: Interfacial layer Al-uptake as a function of reaction time and steel Mn content for the 0.30 wt% dissolved Al bath.

A power-law growth equation (equation 5.1) was used to fit the interfacial layer Al uptake data in Figure 5.27 and the  $K$  and  $n$  values for all experimental steels are presented in Table 5.7. Comparing the  $n$  values for the 0.20 wt% Al bath (Table 5.5) and 0.30 wt% Al bath (Table 5.7) shows that by increasing the bath Al content the  $n$  value significantly increased for the 2.5Mn and 3.0Mn steels, but decreased for the 0.2Mn and

1.4Mn steels. In fact, the  $n$  values for the 2.5Mn and 3.0Mn steels in the case of the 0.30 wt% Al bath are much higher than the parabolic growth  $n$  value of 0.5 (*i.e.*  $n = 0.5$ ) and is close to the interface-controlled growth  $n$  value of 1 (*i.e.*  $n=1$ ), implying the presence of a very open or highly defective interfacial layer structure for these substrates. These observations are consistent with the nature of the 2.5Mn and 3.0Mn interfacial structures observed in Figure 5.21 through Figure 5.23. Also, the lower  $n$  values for the 0.2Mn and 1.4Mn steels for 0.30 wt% Al bath can be attributed to the finer, more compact interfacial layer microstructures observed in Figure 5.19, Figure 5.20 and Figure 5.23.

Table 5.7: Growth rate equation (5.1) parameters for interfacial layer in 0.30 wt% Al bath

Alloy Name	$K$	Standard Error	$n$	Standard Error	$R^2$
0.2Mn	169.3	10.1	0.18	0.04	0.56
1.4Mn	225.4	16.9	0.11	0.05	0.21
2.5Mn	132.5	12.7	0.69	0.06	0.91
3.0Mn	91.6	9.5	0.79	0.06	0.91

## 6 DISCUSSION

### 6.1 Selective oxidation of experimental alloys during annealing

Significant segregation of Mn in the form of MnO (Figure 5.1b and Table 5.1) was observed at the surface and subsurface of the 1.4Mn, 2.5Mn and 3.0Mn steels after annealing (Figure 5.2). The 0.2Mn steel showed little Mn segregation at the surface (Figure 5.2), as would be expected because of its relatively low Mn content, whereas the 1.4Mn through 3.0Mn steels showed considerable Mn surface enrichment. In addition, by increasing the substrate Mn content, the Mn enrichment on the steel surface (Figure 5.2) and the thickness of the Mn oxide layer increased (Figure 6.1 and Table 5.2), following equation (6.1):

$$t_{MnO} = 29C_{Mn}^{0.5} \quad R^2 = 0.98 \quad (6.1)$$

where  $t_{MnO}$  is Mn FWHM depth (nm) and  $C_{Mn}$  is the substrate Mn concentration (wt%).

In addition, no continuous uniform MnO layer was observed for all the experimental steels. The morphological observations of the as-annealed surfaces revealed that the 0.2Mn steel showed some oxides at the grain boundaries with small sparse oxide particles on the bulk grain surface (Figure 5.3a). The 1.4Mn steel showed sparse oxide nodules on the bulk grains as well as oxide ridges at the grain boundaries and adjacent areas (Figure 5.3b and Figure 5.4). However, for the 2.5Mn and 3.0Mn steels, larger oxide nodules as well as film-like oxides were observed on the bulk grain surfaces and at

the grain boundaries and adjacent areas (Figure 5.3(c,d) through Figure 5.6). The ridge morphology at the grain boundaries is indicative of external oxidation at these short circuit diffusion paths arising from the increased O and Mn diffusion rates. Also, the fraction of the surface covered by MnO increased with increasing the steel Mn content (Table 5.2). However, no full surface coverage by MnO was observed, as a large amount of metallic Fe was detected on the surface of all the steels (Figure 5.1a).

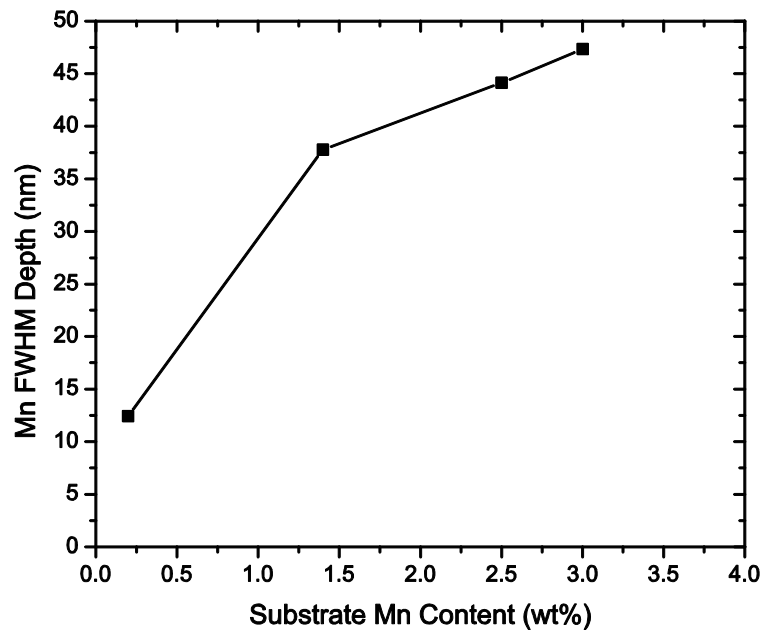


Figure 6.1: MnO layer thickness as a function of substrate Mn content.

## 6.2 Fe-Al interfacial layer development

Despite the selective oxidation of the steels surface, a well-developed Fe-Al interfacial layer and good reactive wetting was observed for all experimental steels. No Fe-Zn intermetallics were observed as part of the interfacial layer.

A uniform, compact Fe-Al interfacial layer morphology consisting of small equiaxed crystals was observed for the 0.2Mn steel at short reaction times for both the 0.20 wt% and 0.30 wt% dissolved Al baths (Figure 5.7(a,b) and Figure 5.19(a,b)) corresponding to the compact inner interfacial layer; however, the fine morphology of the interfacial layer changed to the coarse, non-compact and elongated morphology corresponding to the outer interfacial layer precipitated on the inner layer small crystals at longer reaction times (Figure 5.7(c,d) and Figure 5.19(c,d)). These observations were in agreement with the two-layer morphology previously reported by Guttman et al. (1995), Baril and L'Esperance (1999) and Chen et al. (2008). The lower layer, which is in contact with the substrate, is a compact layer of small equiaxed, closed packed crystals, whereas the upper layer that is in contact with the zinc bath consists of coarser, elongated crystals. However, increasing the dissolved Al bath to 0.30 wt% Al resulted in a finer, more compact Fe-Al interfacial layer microstructure in the case of the 0.2Mn steel.

The effects of substrate Mn content and reaction time on interfacial layer growth was determined by measuring the interfacial layer Al uptake using ICP, as shown in

Figure 5.18 and Figure 5.27 for the 0.20 and 0.30 wt% dissolved Al baths, respectively. The majority of the interfacial layer Al uptake occurred in reaction times of less than 2s (0.5s immersion time). After this time, the interfacial layer Al pickup generally increased non-parabolically (Table 5.5 and Table 5.7), corresponding to a mixed growth mechanism of bulk diffusion and grain boundary diffusion of Fe from the substrate through the Fe-Al interfacial layer, as discussed in §5.2.1.3. These results agree with the two-stage inhibition layer formation advocated by several authors (Guttman 1994, Tang 1995, Toussaint et al. 1998, Giorgi et al. 2005, Chen et al. 2008, Dutta et al. 2009): (i) nucleation and lateral growth, which is associated with a high rate of Al uptake and is completed when the substrate is completely covered by Fe-Al crystals, resulting in the fine, compact Fe-Al layer observed at short reaction times and (ii) solid state diffusional growth, associated with a lower rate of Al uptake resulting in the non-compact upper layer observed at longer reaction times (Figure 5.7(c,d), Figure 5.8(c,d), Figure 5.9(c,d), Figure 5.10(c,d), Figure 5.19(c,d), Figure 5.20(c,d), Figure 5.21(c,d) and Figure 5.22(c,d).

The interfacial layer Al uptake as a function of steel Mn content and bath dissolved Al content for different reaction times is summarized in Figure 6.2. It can be seen that increasing the bath dissolved Al to 0.30 wt% resulted in lower Al uptake for 0.2Mn steel for all reaction times which is consistent with the finer interfacial layer microstructures observed for the 0.30 wt% dissolved Al bath (Figure 5.7 and Figure 5.19).

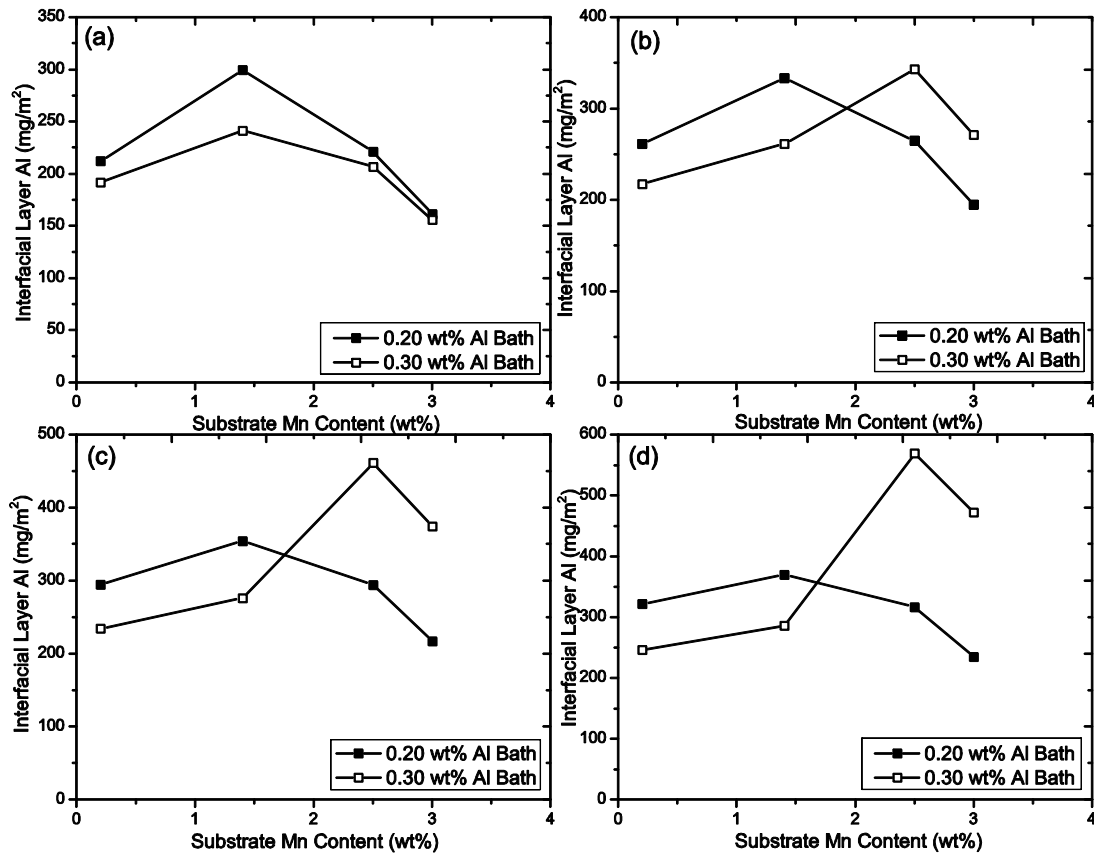


Figure 6.2: Comparison of interfacial layer Al uptake as a function of steel Mn content and bath Al content for: a) 2s, b) 4s, c) 6s and d) 8s reaction times.

The results for the 0.2Mn steel (i.e. lower interfacial layer Al uptake and finer morphology for 0.30 wt% Al bath) can be explained by the balance between Fe dissolution from the substrate and interfacial layer Al pickup, as suggested by Liu and Tang (2004). As was discussed in §2.4.3.2, in this model, the maximum interfacial layer Al pickup for a simple, low alloy steel (e.g. IF steel) occurs at a bath dissolved Al of

approximately 0.20 wt% for a 460°C bath (Figure 6.3); below this bath dissolved Al the interfacial layer growth is Al limited and above this bath dissolved Al it is Fe limited. In another word, increasing the bath Al content to 0.30 wt% resulted in more rapid coverage of substrate with  $\text{Fe}_2\text{Al}_5\text{Zn}_x$  crystals, therefore starting the Fe diffusion controlled growth of the interfacial layer sooner.

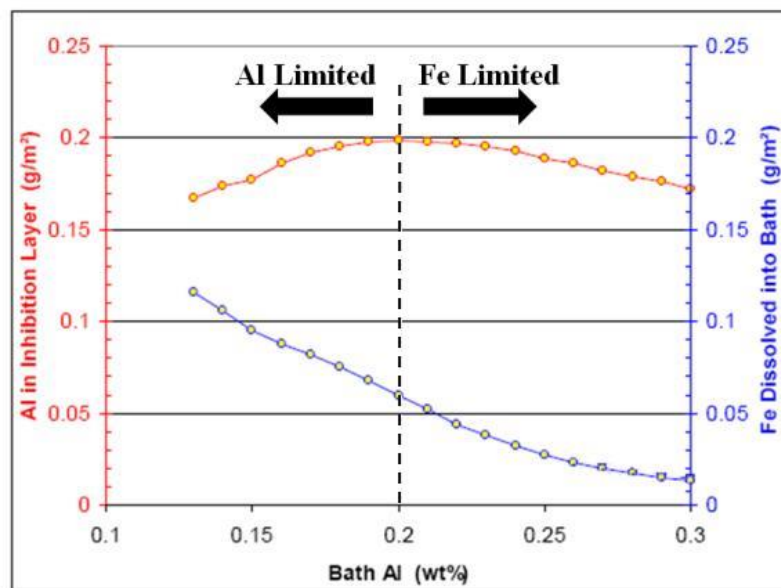


Figure 6.3: Interfacial layer Al uptake and Fe dissolution from the strip versus bath dissolved Al for a 460 °C bath (Liu and Tang 2004).

On the other hand, a coarser, non-homogenous and non-compact interfacial layer morphology was observed for 1.4Mn, 2.5Mn and 3.0Mn steels for 0.20 wt% Al bath (Figure 5.8 through Figure 5.10). Significant areas composed of fine Fe-Al intermetallics were observed between the coarse Fe-Al crystals, especially for the 2.5Mn and 3.0Mn

steels at shorter reaction times (Figure 5.11(b-d), Figure 5.14 and Figure 5.16). These non-homogeneities in the interfacial layer can be attributed to the localized presence of a thicker continuous MnO film which delayed reactive wetting, as shown in Figure 5.14d and Figure 5.16d. However, with increasing the reaction time the number of coarse Fe-Al crystals increased and the interfacial layer comprised larger, elongated crystals, among which some small equiaxed crystals could be observed (Figure 5.8(c,d), Figure 5.9(c,d) and Figure 5.10(c,d)).

However, in the case of 0.30 wt% Al bath, a finer and more homogeneous interfacial layer morphology was observed (Figure 5.20, Figure 5.21 and Figure 5.22). Some areas composed of very fine Fe-Al crystals were also observed for 2.5Mn and 3.0Mn steels at shorter reaction times (Figure 5.20(a,b), Figure 5.21(a,b), Figure 5.22(a,b) and Figure 5.23(c,d)). However, with increasing reaction time the population of fine Fe-Al crystals decreased and the interfacial layer largely comprised the coarser layer of Fe-Al crystals (Figure 5.20(c,d), Figure 5.21(c,d) and Figure 5.22(c,d)).

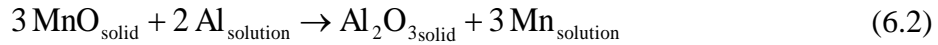
In addition, for the 0.20 wt% Al bath, the 1.4Mn and 3.0Mn steels showed the highest and the lowest Al uptakes, respectively, for all reaction times with the Al pickup for the 2.5Mn steel being intermediate between the two (Figure 5.18 and Figure 6.2). However, increasing the bath dissolved Al content to 0.30 wt% resulted in an increase in the 2.5Mn and 3.0Mn steel Al uptake, particularly at longer reaction times, whereas the Al uptake for the 0.2Mn and 1.4Mn steels decreased (Figure 5.27 and Figure 6.2). Indeed,

despite the significant external MnO on the 2.5Mn and 3.0Mn steels (Figure 6.1), the highest Al uptakes were observed for the 2.5Mn and 3.0Mn steels, respectively, for the 0.30 wt% dissolved Al bath at the longer reaction times (Figure 6.2(c,d)).

Examination of Table 5.5 and Table 5.7 reveals that all  $n$  values were less than parabolic growth  $n$  value of 0.5 for the 0.20 wt% Al bath and for the 0.2Mn and 1.4Mn steels with the 0.30 wt% Al bath, consistent with the mixed mode growth model advocated by Chen et al. (2008), indicating that Fe-Al layer growth was Fe mass transport controlled through the interfacial layer, where the Fe mass transport mechanism was a combination of grain boundary and lattice diffusion and the balance between them shifted to the latter during microstructure coarsening. However, it can be seen that by increasing the bath Al content to 0.30 wt%, the  $n$  values for the 2.5Mn and 3.0Mn steels were significantly greater than 0.5 and close to the interface-controlled growth  $n$  value of 1, implying the presence of a very open and highly defective interfacial layer structure for these substrates which is in agreement with the Fe-Al interfacial layer structures observed for 2.5Mn and 3.0Mn in Figure 5.21 through Figure 5.23.

In fact, to explain the higher Mn steels results the role of dissolved Al in MnO reduction through aluminothermic reduction (equation 6.2) and microstructural considerations (Figure 5.11 and Figure 5.23) should be considered. As was discussed in §2.4.3.3, Kavitha and McDermid (2012) measured the aluminothermic reduction kinetics for a 0.20 wt% dissolved Al bath at 460°C, as shown in equation (6.3). It can be seen that

the MnO reduction kinetics can only reduce a 90nm MnO film within a normal CGL dipping time of 4s.



$$\Delta x(\text{MnO}, \text{nm}) = -49.3 - 9.45 t_{\text{reaction}}, t_{\text{reaction}} \geq 1.2 \text{s} \quad (6.3)$$

Nevertheless, there is evidence that is consistent with the occurrence of aluminothermic reduction during galvanizing of the current steels. For example, the lack of any MnO films at the surface of the 0.2Mn steel (Figure 5.12) and the presence of a 30nm discontinuous MnO film at the surface of the 1.4Mn substrate (Figure 5.13 and Figure 5.24) after 2s reaction time, where the initial thicknesses were approximately 25nm and 40nm (Figure 5.2), respectively, are evidence of this reduction having occurred. In addition, for the 2.5Mn steel dipped in the 0.30 wt% dissolved Al bath, the surface was almost completely covered with Mn oxide after 2.23s reaction time (Figure 5.25), whereas after 7.71s reaction time the surface was almost free of Mn oxide (Figure 5.26).

Thus, in addition to the bath Al consumed in the formation of the Fe-Al layer, bath dissolved Al was also consumed in the reactive wetting of higher Mn steels through the aluminothermic reduction of surface MnO (equation 6.2).

The presence of this additional process (equation 6.2) during Fe-Al interfacial layer formation on the higher Mn alloys had at least two effects:

1) As the rate of aluminothermic reduction is very rapid in its initial stages and the dissolution reaction slows down (Figure 2.13 and equation (6.3)), the interfacial layer on higher Mn steels with nodular external oxide films is now a more defective, two phase mixture of MnO and  $\eta\text{-Fe}_2\text{Al}_5\text{Zn}_x$  ( $0.56 \text{ J/m}^2$  mismatch between Fe-Al grains and MnO is reported by Song et al. (2012)). TEM analysis detected significant MnO remaining between Fe-Al grains, as shown in Figure 5.13 through Figure 5.17, Figure 5.24 and Figure 5.25. At some points, penetration of liquid Zn (Al) through the Mn-rich layer and subsurface resulted in Fe-Al crystals formation below and between the MnO particles (points C and D in Figure 5.13, point B in Figure 5.14, point G in Figure 5.16 and points C and D in Figure 5.24). Also, a heterogeneous and non-compact interfacial layer morphology consisting of a mixture of fine and coarse Fe-Al crystals was observed for the higher Mn steels. In particular, significant areas of very fine crystals of Fe-Al lower layer were observed for the 2.5Mn and 3.0Mn steels at shorter reaction times which with increasing reaction time the number of fine Fe-Al crystals decreased and the interfacial layer exhibited a coarser and more compact morphology (Figure 5.9, Figure 5.10, Figure 5.21 and Figure 5.22).

2) Oxide reduction consumes dissolved Al and, if sufficient quantities are consumed in the mass transport boundary layer, will cause the growth of the Fe-Al layer to become Al limited (Figure 6.3). Lower Al pickup for the 2.5Mn and 3.0Mn steels compared to 1.4Mn steel for 0.20 wt% Al bath, and the decline in Al pickup for the 3.0Mn steel

compare to 2.5Mn steel for 0.30 wt% Al bath (Figure 6.2) are the evidence of Al limited growth due to the aluminothermic reduction of the thicker and larger surface MnO layers observed for the 2.5Mn and 3.0Mn steels (Figure 5.2 and Figure 6.1).

Consequently, the dual factors of additional Al consumption from reaction (6.2) and the more open microstructures associated with the two-phase nature of a MnO-containing interfacial layer will result in significant alterations to the Fe dissolution from the substrate and interfacial layer Al pickup balance discussed in the model of Liu and Tang (2004) (Figure 6.3). For example, in the case of the 1.4Mn steel, the more open interfacial layer structure accelerated Fe diffusion through the interfacial layer and increased Al uptake versus the 0.2Mn substrate for the same bath Al (Figure 6.2). However, in the case of the 2.5Mn substrate and 0.20 wt% Al bath, additional Al consumption through MnO reduction caused the interfacial layer growth to become Al limited, whereas the open structure dominated growth in the case of the 0.30 wt% Al bath due to the greater Al supply. A similar explanation can be applied for the 3.0Mn steel, where the Al supply limit was more severe due to the thicker MnO layer and larger surface coverage present in this case (Figure 6.1).

However, this was not the case for the 0.30 wt% Al baths, where the open structure and rapid mass transport of Fe through the interfacial layer for the 2.5Mn and 3.0Mn substrates, combined with the higher Al supply available from the 0.30 wt% Al bath after MnO reduction, resulted in significantly increase the Al pickup versus the

0.2Mn and 1.4Mn steels and high  $n$  values close to the  $n = 1$  value advocated for interface-controlled growth, implying the presence of a highly defective or open interfacial layer structure for these substrates. However, the decline in Al pickup for the 3.0Mn substrate compare to the 2.5Mn steel for all reaction times (Figure 5.27) indicates that, despite the open structure of the interfacial layer, the Al available for growth was more limited. The most likely candidate in this case is the additional Al consumed in reducing the thicker and larger surface MnO layer on this substrate (Figure 6.1).

In summary, for the 0.20 wt% Al bath, the combined effects of the more open interfacial layer structure and slight Al depletion through MnO reduction served to increase the interfacial layer Al uptake versus the 0.2Mn base material in the case of the 1.4Mn steel. However, in the case of the 2.5Mn and 3.0Mn alloys, increased Al consumption through additional MnO reduction reduced interfacial layer Al pickup as the  $\eta$ -Fe<sub>2</sub>Al<sub>5</sub>Zn<sub>x</sub> growth became Al limited.

For 0.30 wt% Al bath, the increased Al supply and higher local Al content following MnO reduction resulted in the non-compact, highly defective interfacial layers formed on the higher Mn steels dominating the growth process and the Al pickup was higher than that of the 0.2Mn alloy for all experimental reaction times. In the case of the 2.5Mn and 3.0Mn alloys, the highly defective nature of the interfacial layer resulted in the growth kinetics shifting towards being interface controlled from the mixed diffusion mechanism observed for all other alloys and bath Al contents. However, the increased Al

consumption associated with the thicker and larger surface MnO layer on the 3.0Mn steel resulted in the Al uptake being lower than that of the 2.5Mn substrate due to this process being somewhat Al limited. It should be noted that the high Al pickup in the initial 2s is a bit of mystery, but this is the completion of the nucleation stage, where Al diffusion limited growth is not governing the rate of Al pickup and there is no data available to support an Al limited growth model hypothesis at this stage.

### 6.3 Kinetic model of Fe-Al interfacial layer development

Different interfacial layer growth kinetic models have been proposed by several authors (Tang 1995, Toussaint et al. 1998, Giorgi et al. 2005, Chen et al. 2008) and were discussed in section §2.4. It should be noted that in proposed models it is assumed that the interfacial layer growth is controlled by iron diffusion through this layer. Also, the bath dissolved Al supply is unlimited.

As was discussed, Chen et al. (2008) used the growth of an oxide film (Smeltzer et al. 1961, Perrow et al. 1968, Herchl et al. 1972) as an analogy for the growth of the Fe-Al interfacial layer given by:

$$\frac{dx}{dt} = \Omega D_{eff} \frac{\Delta c}{x} \quad (6.4)$$

where  $x$  is the interfacial layer thickness (m),  $t$  the reaction time (s),  $\Omega$  the volume per Fe atom in the  $\text{Fe}_2\text{Al}_{5-x}\text{Zn}_x$  structure,  $\Delta c$  the concentration gradient of Fe across the

interfacial layer and  $D_{eff}$  the effective diffusion coefficient of Fe in the  $Fe_2Al_{5-x}Zn_x$  structure.

Chen et al.'s model (2008) is based on the assumptions that: (i) the flux of Fe through the interfacial layer to react with Al in the zinc bath is the rate-limiting step in the growth process and (ii) the overall Fe transport processes through the interfacial layer comprises both lattice diffusion and grain boundary diffusion. Thus, the effective diffusion coefficient of Fe in the  $Fe_2Al_{5-x}Zn_x$  structure ( $D_{eff}$ ) is expressed as a weighted sum of lattice and grain boundary diffusion:

$$D_{eff} = D_L(1-f) + D_B f \quad (6.5)$$

where  $D_L$  is the lattice diffusion coefficient,  $D_B$  the grain boundary diffusion coefficient and  $f$  the volume fraction of grain boundaries computed as a function of time using equation (6.6):

$$f(t) = \frac{2w}{d_t} = \frac{2w}{(d_0^2 + Kt)^{0.5}} \quad (6.6)$$

where  $w$  is the grain boundary width (assumed to be 1 nm (Smeltzer et al. 1961, Perrow et al. 1968)),  $d_t$  the mean grain size of the interfacial layer at reaction time  $t$ ,  $d_0$  the initial grain size (assumed to be zero) and  $K$  is the growth constant. Substitution of equation (6.4) and equation (6.6) into equation (6.5) and integrating using the boundary condition that  $x=0$  at  $t=0$  (i.e. the Fe-Al layer had zero thickness at  $t=0$ ) and assuming that  $D_B \gg D_L$ ,

the growth law for the interfacial layer as a function of reaction time and bath temperature was obtained:

$$x^2 = K_p \left\{ t + \frac{D_B}{D_L} \frac{4w}{K} (d_0^2 + Kt)^{0.5} \right\} \quad (6.7)$$

$$K_p = 2\Omega D_L \Delta c \quad (6.8)$$

where  $K_p$  is the parabolic rate constant. The Al content of the interfacial layer is subsequently calculated by

$$Al(mg / m^2) = 0.45 \times x \times \rho \quad (6.9)$$

where the factor 0.45 is the mass fraction of Al in  $Fe_2Al_{5-x}Zn_x$ , and  $\rho$  the density of  $Fe_2Al_{5-x}Zn_x$  ( $4125 \times 10^6$  mg/m<sup>3</sup> (Toussaint et al. 1998)).

Following the treatment of Perrow et al. (1968), the integrated form of the interfacial layer growth rate equation (6.4) yields:

$$x^2 = 2\Omega D_{eff} \Delta c t = K_p (eff) t \quad (6.10)$$

where  $K_p(eff)$  is the overall effective rate constant for mixed diffusion controlled growth. According to equation (6.10),  $K_p(eff)$  is a function of the volume of  $Fe_2Al_{5-x}Zn_x$  per Fe atom ( $\Omega$ ), the Fe concentration gradient across the interfacial layer ( $\Delta c$ ) and the effective diffusion coefficient ( $D_{eff}$ ). However,  $\Omega$  is a constant parameter as  $Fe_2Al_{5-x}Zn_x$  was the only phase observed in the interfacial layer for all experimental steels and dissolved Al baths (Table 5.3, Table 5.4 and Table 5.6). Also, because of local supersaturation of Fe in

the vicinity of the steel substrate (Figure 2.5),  $\Delta c$  can be assumed to be constant. Thus, the only parameter that controls  $K_p(\text{eff})$  is  $D_{\text{eff}}$  which is a function of short-circuit diffusion paths fraction in the structure (equation (6.5)).  $K_p(\text{eff})$  values for the experimental alloys reacted in the 0.20 wt% and 0.30 wt% dissolved Al bath were determined using the experimental Al pickup data (Figure 5.18 and Figure 5.27) and equations (6.9) and (6.10) and are presented in Figure 6.4 and Table 6.1.

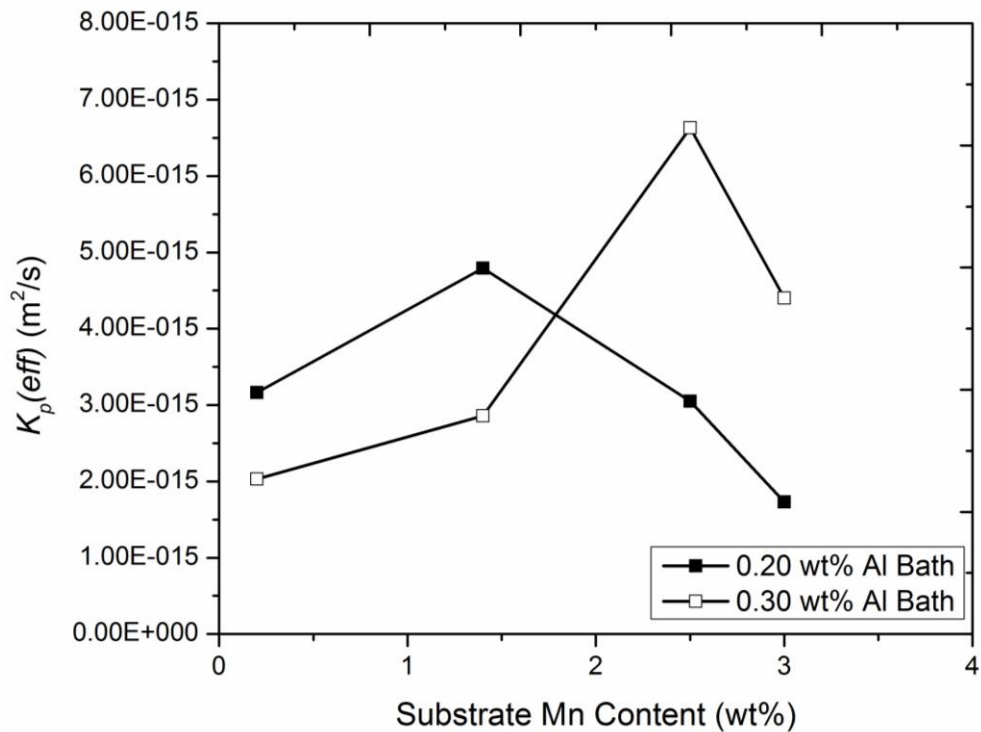


Figure 6.4: Comparison of effective parabolic constant,  $K_p(\text{eff})$ , as a function of steel Mn content and bath Al content.

Table 6.1: Effective parabolic constant values for interfacial layer growth (equation (6.10)).

Alloy Name	$K_p(eff)$ (m <sup>2</sup> /s)	R <sup>2</sup>
0.2Mn – 0.20 wt% Al	$3.16 \times 10^{-15}$	0.96
1.4Mn – 0.20 wt% Al	$4.79 \times 10^{-15}$	0.89
2.5Mn – 0.20 wt% Al	$3.05 \times 10^{-15}$	0.92
3.0Mn – 0.20 wt% Al	$1.73 \times 10^{-15}$	0.92
0.2Mn – 0.30 wt% Al	$2.03 \times 10^{-15}$	0.91
1.4Mn – 0.30 wt% Al	$2.86 \times 10^{-15}$	0.87
2.5Mn – 0.30 wt% Al	$6.63 \times 10^{-15}$	0.95
3.0Mn – 0.30 wt% Al	$4.40 \times 10^{-15}$	0.93

It can be seen that for 0.20 wt% dissolved Al both the highest and lowest  $K_p(eff)$  values are for the 1.4Mn and 3.0Mn steels, respectively. However, increasing the bath Al content to 0.30 wt% Al resulted in significantly higher  $K_p(eff)$  values for the 2.5Mn and 3.0Mn steels and lower values for 0.2Mn and 1.4Mn steels.

As was discussed in §5.2, the structure of the Fe-Al interfacial layer for the higher Mn steels (1.4Mn through 3.0Mn) was not homogenous and consisted of a mixture of fine and coarse crystals (Figure 5.7 through Figure 5.11 and Figure 5.19 through Figure 5.23). In addition, TEM analysis of the cross-sections of the higher Mn steels showed that Mn-rich grains remained at the Fe/Zn interface where, the thickness of the remaining Mn-rich layer increased by increasing the steel Mn content (Figure 5.13 through Figure 5.17, Figure 5.24 and Figure 5.25). The interfacial layer openness was calculated by measuring the two-dimensional area fraction as a function of time with an image analysis system

(Clemex IA, Clemex Technologies, Inc., Longueuil, QC, Canada), as shown in Figure 6.5. It can be seen that the black area fraction represents the fraction of open areas in the interfacial layer structure including grain boundaries, triple junctions and holes and the yellow area is representative of the Fe-Al interfacial layer grains (Figure 6.4(b,d)).

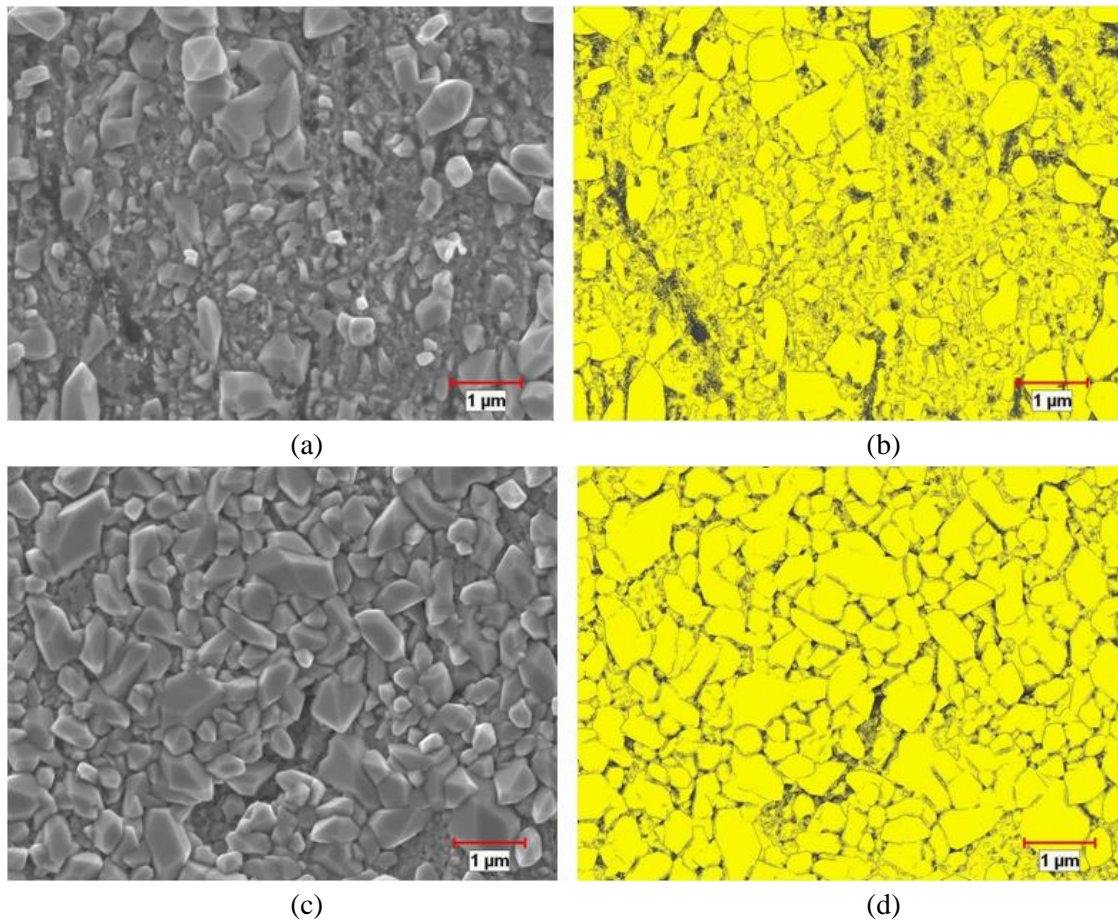


Figure 6.5: Calculation of Fe-Al interfacial layer and short-circuit diffusion paths areas for the 1.4Mn steel galvanized in a 0.20 wt% dissolved Al bath for reaction times of: (a,b) 2.20s and (c,d) 7.68s. Yellow= Fe-Al interfacial layer and black=short circuit diffusion paths.

It should be mentioned that the openness parameter is not exactly equal to short-circuit diffusion paths fraction, as some of those holes and gaps between the interfacial layer grains were filled with MnO, as was observed in TEM images (Figure 5.14 through Figure 5.17, Figure 5.24 and Figure 5.25). However, the trend between interfacial layer openness and steel Mn content can be a good representative of the expected trend between short-circuits diffusion paths fraction and steel Mn content.

The variation of interfacial layer openness with reaction times for different Mn-containing steels for the 0.20 wt% and 0.30 wt% dissolved Al bath are shown in Figure 6.6. A first-order kinetic equation (6.11) was used to fit the data as was proposed by Smeltzer et al. (1961).

$$f(t) = f^0 \exp(-kt) \quad (6.11)$$

where  $f^0$  is the initial fraction of total low resistance paths and  $k$  is the growth constant and their values for different Mn content steels for the 0.20 wt% and 0.30 wt% dissolved Al bath are listed in Table 6.2. It can be seen that by increasing the steel Mn content the fraction of open areas in the interfacial layer increases for both Al baths which is in agreement with SEM observations (Figure 5.7 through Figure 5.11 and Figure 5.19 through Figure 5.23). Also, by increasing the reaction time, interfacial layer openness decreases.

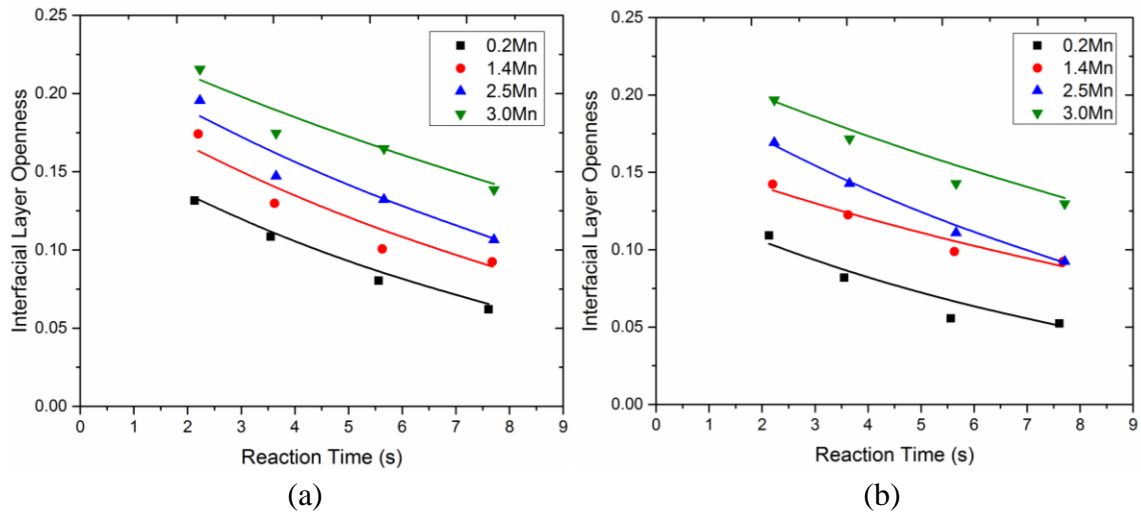


Figure 6.6: Comparison of Fe-Al interfacial layer openness for different Mn-containing steels for the (a) 0.20 wt% and (b) 0.30 wt% dissolved Al baths.

Table 6.2: Fe-Al interfacial layer openness constant values.

Alloy Name	$f^{\theta}$	$k$
0.2Mn – 0.20 wt% Al	0.18	0.13
1.4Mn – 0.20 wt% Al	0.21	0.11
2.5Mn – 0.20 wt% Al	0.23	0.10
3.0Mn – 0.20 wt% Al	0.24	0.07
0.2Mn – 0.30 wt% Al	0.14	0.13
1.4Mn – 0.30 wt% Al	0.17	0.08
2.5Mn – 0.30 wt% Al	0.21	0.11
3.0Mn – 0.30 wt% Al	0.23	0.07

Thus, a more open, defective microstructure associated with the two phase mixture of MnO and  $\text{Fe}_2\text{Al}_{5-x}\text{Zn}_x$  should have resulted in a higher short-circuit diffusion paths fraction and, therefore, a higher effective diffusion coefficient (equation 6.5) and

more rapid mass transport of Fe to the interfacial layer/zinc bath interface for the higher Mn steels.

This trend can explain the higher  $K_p(eff)$  for the 1.4Mn steel versus that for the 0.2Mn steel for the 0.20 wt% dissolved Al bath. However, despite the more open and defective interfacial layer (Figure 6.6a and Table 6.2), lower  $K_p(eff)$  values were observed for 2.5Mn and 3.0Mn steels, suggesting that the rate limiting step in the growth process shifts from Fe transport to the dissolved Al, likely due to Al depletion in the mass transport boundary layer by aluminothermic reduction. This, also, can explain the lowest  $K_p(eff)$  value for the 3.0Mn steel, as the degree of Al depletion is inversely proportional to the MnO thickness and the thickest surface MnO was observed for the 3.0Mn steel (Figure 6.1). However, increasing the dissolved Al bath to 0.30 wt% Al provided more dissolved Al available to react with Fe diffusing through the short-circuit diffusion paths present in the interfacial layer and, therefore, resulted in the higher  $K_p(eff)$  values computed for the 2.5Mn and 3.0 Mn steels (Table 6.1). In fact, in the case of the 2.5Mn and 3.0Mn alloys, the highly defective interfacial layer combined with the higher Al supply available from the 0.30 wt% Al bath after aluminothermic reduction of MnO resulted in the growth kinetics shifting towards being interface controlled from the mixed diffusion mechanism observed for all other alloys and bath Al contents. However, lower  $K_p(eff)$  value for 3.0Mn steel versus 2.5Mn steels in the 0.30 wt% Al bath indicates that, despite more non-compact and defective interfacial layer, the interfacial layer growth was

Al limited which is attributed to the increased Al consumption associate with the thicker and larger surface MnO layer on the 3.0Mn steel (Figure 6.1)

In the model advanced by Smeltzer et al. (1961), the fraction of short-circuits diffusion paths decreased according to the first-order kinetic equation (6.11). Substitution of equations (6.5) and (6.11) into equation (6.4) and integrating using the assumption that  $D_B \gg D_L$ , yields the growth law:

$$x^2 = K_p \left\{ t + \frac{f^0 D_B}{k D_L} (1 - e^{-kt}) \right\} \quad (6.12)$$

It should be noted that, in Smeltzer et al.'s (1961) model,  $D_B$  is the diffusion constant for all short-circuit diffusion paths. Equation (6.12) can be expressed in different forms for various limiting cases useful in analysis of the experimental data:

(i) during the initial stages when the film is thin ( $t \rightarrow 0$ )

$$x^2 = \left(1 + \frac{f^0 D_B}{D_L}\right) K_p t \quad (6.13)$$

and (ii) for thick films ( $e^{-kt} \ll 1$ )

$$x^2 - x_0^2 = K_p t \quad (6.14)$$

$$x_0^2 = K_p \frac{f^0 D_B}{k D_L} \quad (6.15)$$

$$k = \frac{1}{t_0} \ln \frac{x_0^2}{K_p t_0} \quad (6.16)$$

As values for the diffusion and short-circuit diffusion paths parameters are lacking, particularly for two-phase mixture of a MnO-containing interfacial layer for high Mn steels,  $f^0 D_B / D_L$  will be considered as one parameter.  $K_p$  and  $x_0^2$  values for the experimental alloys reacted in the 0.20 wt% and 0.30 wt% dissolved Al baths were determined using the experimental Al pickup data (Figure 5.18 and Figure 5.27) and equation (6.14) and are presented in Figure 6.7 and Table 6.3. The time  $t_0$  at which  $x=x_0$  were calculated using equation (6.9), the power law growth equation (5.1) and growth rate parameters listed in Table 5.5 and Table 5.7.  $k$  and  $f^0 D_B / D_L$  values were calculated from equations (6.16) and (6.15), respectively, and are listed in Table 6.3. It should be mentioned that calculated  $e^{-kt}$  values for all experimental alloys and dissolve Al baths were less than 1 (*i.e.* in the range of  $10^{-2}$  to  $10^{-6}$ ) confirming that the interfacial layer is a thick film for all alloys and dissolve Al baths. The Al content of the interfacial layer was subsequently obtained by equation (6.9). It should be noted that the nonzero intercepts are due to the non-parabolic growth exponents, as shown in Table 5.5 and Table 5.7. In fact, negative intercept values resulted from the near-linear growth exponents observed for the 2.5Mn and 3.0Mn steels in the 0.30 wt% Al bath. In addition, higher  $f^0 D_B / D_L$  values were obtained for the 1.4Mn steel than that for 0.2Mn steels which can be attributed to the residual MnO at the steel/zinc interface (Figure 5.13 and Figure 5.24) and their more open interfacial layer (Figure 5.8, Figure 5.11, Figure 5.20 and Figure 5.23). In addition,

despite the more open and defective interfacial layer ( $f^0$ ) observed for the 2.5Mn and 3.0Mn steels for the 0.20 wt% Al bath (Figure 6.6a, Table 6.2 and Figure 5.9, Figure 5.10 and Figure 5.14 through Figure 5.17), lower  $f^0 D_B / D_L$  values were obtained which can be explained by Al depletion resulting from the aluminothermic reduction of MnO.

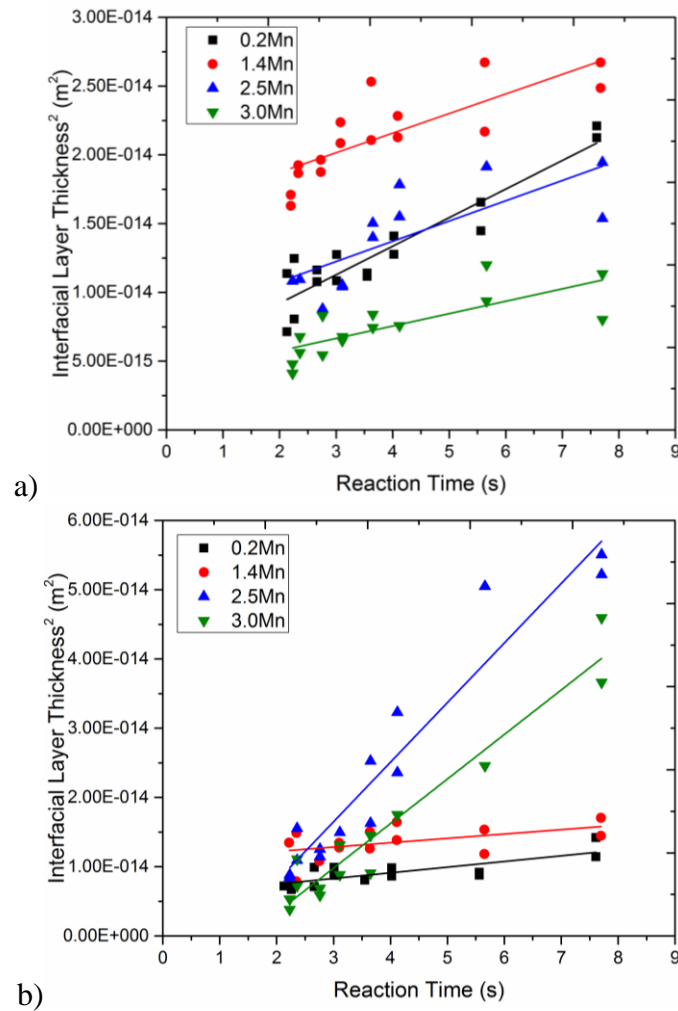


Figure 6.7: Computation of  $K_p$  values from interfacial layer growth data for different Mn-containing steels for the (a) 0.20 wt% and (b) 0.30 wt% dissolved Al baths.

Table 6.3: Values for interfacial layer growth model (equations (6.14) through (6.16)).

Alloy Name	$K_p$ (m <sup>2</sup> /s)	$x_0^2$ (m <sup>2</sup> )	$t_0$ (s)	$k$ (m <sup>2</sup> /s)	$f^0 D_B / D_L$
0.2Mn – 0.20 wt% Al	$2.08 \times 10^{-15}$	$5.06 \times 10^{-15}$	0.78	1.44	3.51
1.4Mn – 0.20 wt% Al	$1.43 \times 10^{-15}$	$1.59 \times 10^{-14}$	1.36	1.55	17.16
2.5Mn – 0.20 wt% Al	$1.47 \times 10^{-15}$	$7.83 \times 10^{-15}$	1.35	1.02	5.41
3.0Mn – 0.20 wt% Al	$9.01 \times 10^{-16}$	$3.95 \times 10^{-15}$	1.23	1.03	4.51
0.2Mn – 0.30 wt% Al	$8.18 \times 10^{-16}$	$5.85 \times 10^{-15}$	1.10	1.70	12.17
1.4Mn – 0.30 wt% Al	$6.29 \times 10^{-16}$	$1.10 \times 10^{-14}$	1.60	1.49	25.96
2.5Mn – 0.30 wt% Al	$8.60 \times 10^{-15}$	$-9.31 \times 10^{-15}$	-	-	-
3.0Mn – 0.30 wt% Al	$6.43 \times 10^{-15}$	$-9.49 \times 10^{-15}$	-	-	-

Model results with reference to experimental data from the 0.20 wt% and 0.30 wt% dissolved Al baths are shown in Figure 6.8. Due to the negative intercepts and lacking values for  $k$  and  $f^0 D_B / D_L$  for the 2.5Mn and 3.0Mn steels in the 0.30 wt% dissolved Al bath, the fitted curves were calculated using equation (6.10) and the calculated  $K_p(eff)$  values (Table 6.1). It can be seen that the model is in good agreement with the experimental results. The slope at the origin can provide an additional check via equation (6.13) for cases where the experimental data for short times are available. However, no data were captured experimentally at very short reaction times due to the rapid interfacial layer formation. It must be noted that a full evaluation of the model validity rests on obtaining values for lattice and short-circuit diffusion paths volume fractions and diffusion coefficients.

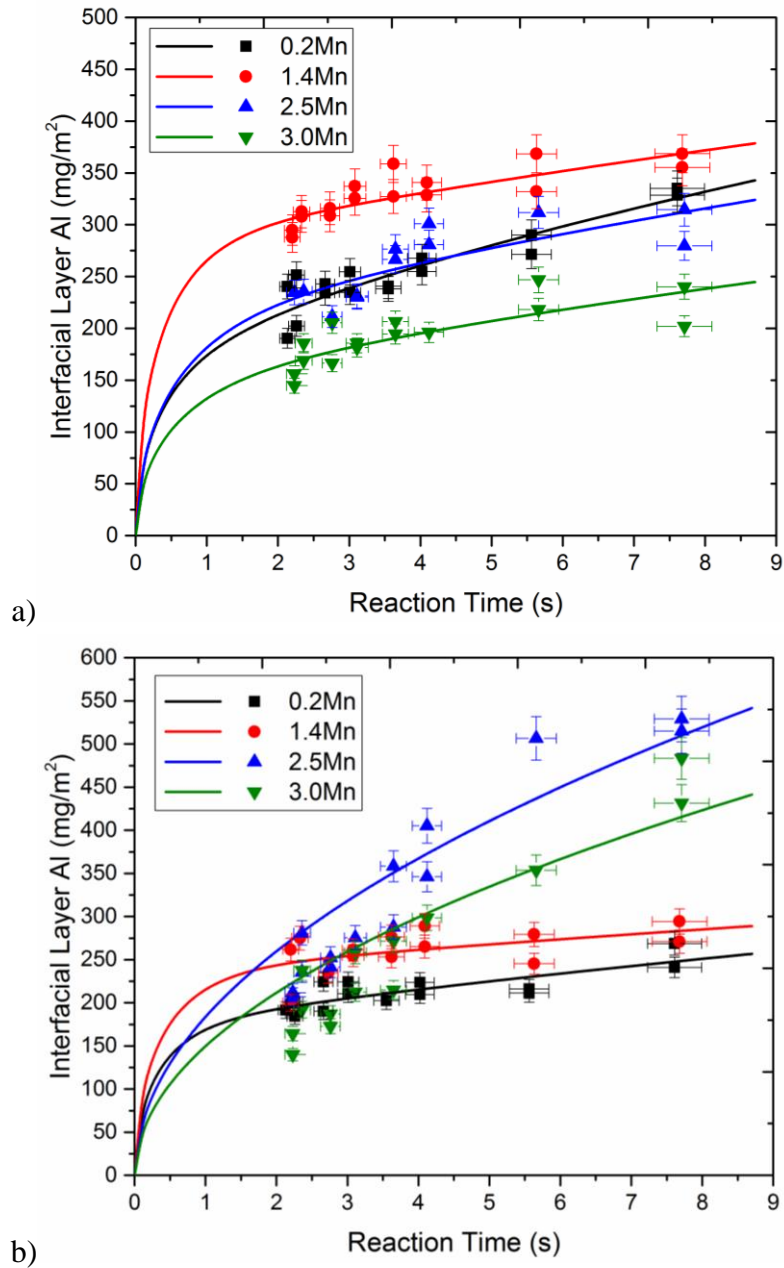


Figure 6.8: Experimental data of interfacial layer Al uptake as a function of reaction time and steel Mn content for (a) 0.20 wt% and (b) 0.30 wt% dissolved Al baths shown with modelling results (data points and lines are experimental and model results, respectively).

## **7 CONCLUSIONS AND RECOMMENDATIONS**

### **7.1 Selective oxidation**

Surface Mn segregation in the form of MnO was observed for all experimental steels during annealing prior to dipping in the Zn-alloy bath. Mn enrichment occurred primarily along the grain boundaries and adjacent areas. The 0.2Mn steel showed some oxide particles at the grain boundaries with fine, widely-spaced oxide nodules on the bulk grains. On the other hand, significant populations of larger oxide nodules on the bulk grains as well as oxide ridges at the grain boundaries and adjacent areas were observed for 1.4Mn, 2.5Mn and 3.0Mn steels. The thickness of the MnO layer and the portion of the substrate surface covered with MnO increased significantly with increasing steel Mn content. Also, a large amount of metallic iron was observed on the surface of all steels.

### **7.2 Fe-Al interfacial layer development**

Despite the selective oxidation of Mn on the steel surface, a well developed Fe-Al interfacial layer was observed for all experimental steels. The Fe-Al interfacial layer morphology observed for the 0.2Mn steel was similar to that previously observed for IF steels. At lower reaction times the interfacial layer morphology comprised a compact layer of fine equiaxed crystals; whereas the interfacial layer at higher reaction times had a coarser morphology with some embedded fine, equiaxed crystals. On the other hand, the

structure of the Fe-Al interfacial layer at short reaction times for the higher Mn steels was not homogenous and consisted of a mixture of fine and coarse crystals. However, with increasing reaction time the population of fine Fe-Al crystals decreased and the interfacial layer was comprised primarily of larger, non-compact Fe-Al crystals. Furthermore, compact, finely crystalline Fe-Al areas were observed at short reaction times for the 2.5Mn and 3.0Mn steels, which corresponded to the compact inner interfacial layer. Moreover, for all reaction times, the interfacial layers observed on the higher Mn containing steels was less compact compared to that of the 0.2Mn steel. Also, increasing the dissolved Al bath to 0.30 wt% Al resulted in a finer, more compact Fe-Al interfacial layer microstructure for all experimental steels and reaction times.

Cross-sections of the higher Mn steels showed that MnO grains remained at the steel/Zn coating interface after galvanizing. In fact, by increasing the steel Mn content, the thickness of the remained Mn-rich oxide layer increased. Also, penetration of Zn(Al) liquid through the MnO layer and subsurface resulted in the formation of Fe-Al layer between and below the MnO particles resulted in a two-phase interfacial layer consisting of MnO and  $\text{Fe}_2\text{Al}_{5-x}\text{Zn}_x$ .

The interfacial layer Al uptake increased non-parabolically with increasing reaction time for all experimental steels and bath Al levels. For the case of the 0.20 wt% Al bath, the 1.4Mn and 3.0Mn steels showed the highest and the lowest Al uptakes, respectively. However, increasing the dissolved Al bath to 0.30 wt% Al resulted in a

lower Al uptake for the 0.2Mn and 1.4Mn steels for all reaction times and a significantly higher Al uptake for the 2.5Mn and 3.0Mn steels, particularly at longer reaction times. Furthermore, growth exponent values were determined to be less than 0.5 for the 0.20 wt% and 0.30 wt% Al baths for the 0.2Mn and 1.4Mn steels, indicative of a mixed lattice and short-circuit diffusion-controlled growth. However, the growth exponent values for the 2.5Mn and 3.0Mn steels in the 0.30 wt% Al bath were close to 1, indicative of a highly defective interfacial layer and suggesting interface-controlled growth.

A kinetic model based on the oxide film growth was used to describe the interfacial layer growth kinetics for Mn-containing steels and 0.20 wt% and 0.30 wt% dissolved Al baths. For the 0.20 wt% Al bath, it was determined that despite dissolved bath Al consumption via aluminothermic reduction of the MnO layer, the presence of unreduced MnO in the Fe-Al interfacial layer and more open interfacial layer structure contributed to increase the effective diffusion coefficient of Fe through interfacial layer and maximize the interfacial layer uptake versus the 0.2Mn base material in the case of the 1.4Mn steel. However, in the case of the 2.5Mn and 3.0Mn steels, regardless of more open and defective interfacial layer, the increased Al consumption due to the thicker and larger surface MnO layer caused the interfacial layer growth to become Al supply limited and, therefore, a lower Al uptake was observed.

In the case of the 0.30 wt% Al bath, the increased Al supply and higher local Al content following MnO reduction resulted in the non-compact, defective nature of the

interfacial layers formed on the higher Mn steels to dominate and the Al pickup was higher than that of the 0.2Mn steel for all experimental reaction times. In the case of the 2.5Mn and 3.0Mn steels, the highly defective nature of the interfacial layer resulted in the growth kinetics shifting to a more interface controlled growth from the mixed lattice and short-circuit diffusion mechanism observed for all other alloys and bath Al contents. However, the increased Al consumption associated with the thicker and larger surface MnO layer on the 3.0Mn steel resulted in the Al uptake being lower than that of the 2.5Mn substrate.

### **7.3 Recommendations for future work**

Selective oxidation and galvanizing of Mn-containing DP steels should continue to be studied for larger range of process atmosphere  $pO_2$  to investigate the influence of Mn internal and external oxidation on the interfacial layer formation kinetics. Improvement to interfacial layer formation can also be made by testing different galvanizing bath chemistries such as the bath studied by Blumenau et al. (2011) having small addition of Mg (0.1 wt%) to enhance the surface oxide reduction.

The galvannealing kinetics of DP steels should also be studied to explore the influence of galvanizing process parameters and steel composition on inhibition

breakdown and growth kinetics of the galvanized layer to facilitate prediction of Fe-Zn phases formation for a given set of process conditions.

Moreover, selective oxidation, galvanizing and galvannealing investigations should be expanded to other advanced high strength steels such TRIP and TWIP steels having different alloying elements, Si/Mn ratios and higher Mn contents to reveal the effect of complex oxide composition and morphology on Fe-Al interfacial layer formation and galvanized layer growth kinetics.

Finally, the effect of galvanizing and galvannealing process parameters on coating adhesion, formability and weldability should be studied.

## 8 References

- Alibeigi, S., R. Kavitha, R.J. Meguerian and J.R. McDermid. 2011. *Acta Mater.* 59: 3537-3549.
- Baril, E. and G. L'Esperance. 1999. *Metall. Mater. Trans. A* 30: 681-695.
- Baril, E., G. L'Esperance and E. Boutin . 1998. Proc. 4<sup>th</sup> Int. Conf. on Zinc Alloy Coated Steel Sheet, Galvatech'98, Chiba, Japan , September 20-23, 1998, Association for Iron and Steel Technology: 168-173.
- Bellhouse, E.M., A.I.M. Mertens and J.R. McDermid. 2007. *Mater. Sci. Eng. A* 463: 147-156.
- Bellhouse, E.M. and J.R. McDermid. 2008. *Mater. Sci. Eng. A* 491: 39-46.
- Bellhouse, E.M. and J.R. McDermid. 2010. *Metall. Mater. Trans. A* 41: 1539-1553.
- Bellhouse, E.M. and J.R. McDermid. 2011. *Metall. Mater. Trans. A* 42: 2753-2768
- Bellhouse, E.M. and J.R. McDermid. 2012. *Metall. Mater. Trans. A* 43: 2426-2441.
- Biesinger, M.C., B.P. Payne, A.P. Grosvenor, L.W.M. Lau, A.R. Gerson and R.C. Smart. *Appl. Surf. Sci.* 257: 2717-2730.
- Birks, N., G.H. Meier and F.S. Pettit. 2006. *Introduction to the High-Temperature Oxidation of Metals*. Cambridge, UK: Cambridge University Press.
- Blumenau, M., M. Norden, F. Friedel and K. Peters. 2011. *Surf. Coat. Tech.* 206: 559-567.
- Bode, R., M. Meurer, T.W. Schaumann and W. Warnecke2004. Proc. 6<sup>th</sup> Int. Conf. on Zinc Alloy Coated Steel Sheet, Galvatech'04, Chicago, IL, USA, April 4-7, 2004, Association for Iron and Steel Technology: 107-118.

- Briggs, D. and J.C. Rivière. 1983. *Spectral Interpretation. Practical Surface Analysis by Auger and X-ray Photoelectron Spectroscopy*. UK: John Wiley & Sons.
- Bubert, H. and H. Jenett. 2011. *Surface and Thin Film Analysis: A Compendium of Principles, Instrumentation and Applications*. 2<sup>nd</sup> Edition. Weinheim, Germany: John Wiley & Sons.
- Chen, L., R. Fourmentin and J.R. McDermid. 2008. *Metall. Mater. Trans. A* 39: 2128-2142.
- Chen, Z. W., R. M. Sharp and J. T. Gregory. 1990. *Mater. Forum* 14: 130-136.
- Cho, L., S.J. Lee, M.S. Kim, Y.H. Kim, B.C. De Cooman. 2013. *Metall. Mater. Trans. A* 44: 362-71.
- Cvijovic, I., I. Parezanovic and M. Spiegel. 2006. *Corrosion Science* 48: 980-993.
- Dean, J.R., 2005. *Practical inductively coupled plasma spectroscopy*. Chichester, UK : John Wiley & Sons.
- Deng, Z.J., J. Liu, Z.H. Lu, H. Wang and C.J. Lin. 2011. *Adv. Mater. Res.* 295-297: 1669-1674.
- Drillet, P., Z. Zermout, D. Bouleau and J. M. Maigne. 2001. Proc. 5<sup>th</sup> Int. Conf. on Zinc Alloy Coated Steel Sheet, Galvatech'01, Brussels, Belgium, June 26-28, 2001, Association for Iron and Steel Technology: 195-202.
- Drillet, P., Z. Zermout, D. Bouleau, J. Maigne, S. Claessens. 2004. Proc. 6<sup>th</sup> Int. Conf. on Zinc Alloy Coated Steel Sheet, Galvatech'04, Chicago, IL, USA, April 4-7, 2004, Association for Iron and Steel Technology: 1123-1134.
- Dubois, M. 1998. *Zinc-Based Steel Coating Systems: Production and Performance*. TMS, Warrendale, PA, USA: 39-50.
- Dutta, M. and S.B. Singh. 2009. *Scripta Materialia*. 60: 643-646.

- Faderl, J., W. Maschek and J. Strutzenberger. 1995. Proc. 3<sup>rd</sup> Int. Conf. on Zinc Alloy Coated Steel Sheet, Galvatech'95, Chicago, IL, USA, September 17-21, 1995, Association for Iron and Steel Technology: 675-685.
- Faderl, J., M. Pimminger and L. Schonberger. 1992. Proc. 2<sup>nd</sup> Int. Conf. on Zinc Alloy Coated Steel Sheet, Galvatech'92, Amsterdam, The Netherlands, September 8-10, 1992, Association for Iron and Steel Technology: 194-198.
- Fine, H. A. and G. H. Geiger. 1979. *Handbook on Material and Energy Balance Calculations in Metallurgical Processes*. Warrendale, Pennsylvania, USA: The Metallurgical Society of AIME.
- Giorgi, M.L., J.B. Guillot and R. Nicolle. 2005. Mater. Sci. 40: 2263-2268.
- Goldstein, J., D. Newbury, D. Joy, C. Lyman, P. Echlin, E. Lifshin, L. Sawyer and J. Michael. 2003. *Scanning Electron Microscopy and X-Ray Microanalysis*. 3<sup>rd</sup> Edition. New York, NY, USA: Springer.
- Gong, Y.F., H.S. Kim and B.C. De Cooman. 2008. ISIJ Int. 48: 1745-1751.
- Gong, Y.F., H.S. Kim and B.C. De Cooman. 2009. ISIJ Int. 49: 557-563.
- Gong, Y.F. and B.C. De Cooman. 2011. ISIJ Int. 51: 630-637.
- Grabke, H.J., V. Leroy and H. Viehhaus. 1995. ISIJ Inter. 35: 95-113.
- Grant, J.T. 2003. *AES: Basic Principles, Spectral Features and Qualitative Analysis. Surface Analysis by Auger and X-Ray Photoelectron Spectroscopy*. Chichester, UK: IM Publications and Surface Spectra.
- Grosvenor, A.P., B.A. Kobe, M.C. Biesinger and N.S. McIntyre. 2004. Surf. Interface Anal. 36: 1564-1574.
- Guttman, M. 1994. Mater. Sci. Forum 155-156: 527-548.
- Guttman, M., Y. Leprêtre, A. Aubry, M. J. Roch, T. Moreau, P. Drillet, J. M. Mataire and H. Baudin. 1995. Proc. 3<sup>rd</sup> Int. Conf. on Zinc Alloy Coated Steel Sheet, Galvatech'95,

Chicago, IL, USA, September 17-21, 1995, Association for Iron and Steel Technology: 295-307.

Harvey, G. J. and P. D. Mercer. 1973. Metall. Trans. 4: 619-621.

Herchl, R., N. N. Khoi, T. Homma and W. W. Smeltzer .1972. Oxidation of Metals 4: 35-46.

Herveldt, J. Craenen, J. Dilewijns, B. Blanpain, C. Xhoffer and B.C. De Cooman, 1998. Zinc-Based Steel Coating Systems: Production and Performance. TMS, Warrendale, PA, USA: 13-25.

Hill, S.J. 2007. *Inductively coupled plasma spectrometry and its applications*. Chennai, India: Wiley-Blackwell Publishing Ltd.

Inagaki, J., M. Sakurai and M. Sagiya. 1995. ISIJ Int. 35: 1388-1393

Isobe, M. 1992. CAMP-ISIJ 5: 1629-1632.

Jordan, C.E. and A.R. Marder. 1997. Metall. Mater. Trans. A 28: 2683-2694.

Kavitha, R. and J.R. McDermid. 2012. Surf. Coat. Tech. 212: 152-158.

Khondker, R., A. Mertens and J.R. McDermid. 2007. Mater. Sci. Eng. A 463: 157-165.

Kim, Y., J. Lee, S.H. Jeon and K.G. Chin. 2012. Mat. Sci. 47: 8477-8482.

Kiusalaas, R., G. Engberg, H. Klang, E. Schedin and L. Schon. 1998. Proc. 4<sup>th</sup> Int. Conf. on Zinc Alloy Coated Steel Sheet, Galvatech'98, Chiba, Japan , September 20-23, 1998, Association for Iron and Steel Technology: 485-492.

Kofstad, P. 1988. High Temperature Corrosion. Elsevier Applied Science Publishers Ltd.

Leprêtre, Y., J. M. Maigne, M. Guttmann and J. Philibert.1998. Zinc-Based Steel Coating Systems: Production and Performance. TMS, Warrendale, PA, USA: 95-114.

- Li, X.S., S.-I. Baek, C.-S. Oh, S.-J. Kim, and Y.-W. Kim. 2007. *Scripta Mater.* 57: 113-116.
- Li, Y., Sh. Jiang, X. Yuan, B. Chen and Q. Zhang. 2011. *Suf. Interface Anal.* 44: 472-477.
- Liewellyn, D.T., and D.J. Hillis. 1996. *Iron making and Steelmaking.* 23: 471-477.
- Lin, C.S., M. Meshii, and C.C. Cheng. 1995. Proc. 3<sup>rd</sup> Int. Conf. on Zinc Alloy Coated Steel Sheet, Galvatech'95, Chicago, IL, USA, September 17-21, 1995, Association for Iron and Steel Technology: 335-342.
- Liu, Y. H. and N. Y. Tang. 2004. Proc. 6<sup>th</sup> Int. Conf. on Zinc Alloy Coated Steel Sheet, Galvatech'04, Chicago, IL, USA, April 4-7, 2004, Association for Iron and Steel Technology: 1155-1164.
- Loison, D., D. Huin, V. Lanteri, J.P. Servais and R. Cremer. 2001. Proc. 5<sup>th</sup> Int. Conf. on Zinc Alloy Coated Steel Sheet, Galvatech'01, Brussels, Belgium, June 26-28, 2001, Association for Iron and Steel Technology: 203-209.
- Mahieu, J., S. Claessens and B.C. De Cooman. 2001. *Metall. Mater. Trans. A* 32: 2905-2907.
- Mahieu, J., S. Claessens, B.C. De Cooman and F. Goodwin. 2004. Proc. 6<sup>th</sup> Int. Conf. on Zinc Alloy Coated Steel Sheet, Galvatech'04, Chicago, IL, USA, April 4-7, 2004, Association for Iron and Steel Technology: 529-538.
- Marder, A. 2000. *Progress in Materials Science* 45: 191-271.
- Mataigne, J.M., M. Lamberigts and V. Leroy. 1992. *Developments in the Annealing of Sheet Steels*, Eds. R. Pradhan and I. Gupta. Warrendale, PA, USA: Minerals, Metals & Materials Society: 512-528.
- McDermid, J.R., M.H. Kaye and W.T. Thompson. 2007. *Metall. Mater. Trans. B* 38: 215-230.
- McDevitt, E., Y. Morimoto and M. Meshii. 1997. *ISIJ Int.* 37: 776-782.

- Meguerian, R.J. 2007. M.Sc. Thesis, McMaster University, Hamilton, Ontario, Canada.
- Messien, P., J.C. Herman and T. Greday. 1981. Fundamentals of Dual-Phase Steels, Conf. Proc. The Metal. Soc. of AIME 1981, Ed. R.A. Kot B.L. Bramfitt, Warrendale, PA.: 161-180.
- Mintz, B., 2001. Inter. Mater. Rev. 46: 169-197.
- Morimoto, Y., E. McDevitt and M. Meshii. 1997. ISIJ Int. 37: 906-913.
- Nakano, J. 2006. Doctoral Thesis, McMaster University, Hamilton, Ontario, Canada.
- Nakano, J., D.V. Malakhov, S. Yamaguchi and G.R. Purdy. 2007. CALPHAD 31:125-140.
- Olefjord, I., W. Leijon and U. Jelvestam. 1980. Appl. Surf. Sci. 6: 241-255.
- Ollivier-Leduc, A., M.L. Giorgi, D. Balloy and J.B. Guillot. 2010. Corros. Sci. 52: 2498-2504.
- Perrot, P., J. C. Tissier and J. Y. Dauphin. 1992. Z Metallkde. 83: 786-790.
- Perrow, J. M., W. W. Smeltzer and J. D. Embury. 1968. Acta Metall. 16: 1209-1218.
- Rapp, R.A. 1965. Corrosion 21: 382-401.
- Sagl, R., A. Jarosik, D. Stifter and G. Angeli. 2013. Corros. Sci. 70: 268-275.
- Sendzimer, T. 1938. U.S. Patent No. 2,110,893.
- Shastri, C.R., J.A. Rotole and T.W. Kaiser. 2007. Proc. 7<sup>th</sup> Int. Conf. on Zinc Alloy Coated Steel Sheet, Galvatech'07, Osaka, Japan, November 18-22, 2007, Association for Iron and Steel Technology: 403-408.
- Smeltzer, W. W., R. R. Haering and J. S. Kirkaldy. 1961. Acta Metall. 6: 880-885.

- Song, G.M., T. Vystavel, N. van der Pers, J.Th.M. De Hosson, W.G. Sloof. 2012. *Acta Materialia*. 60: 2973-2981.
- Staudte, J., J.M. Mategne, D. Loison and F. Del Frate. 2011. Proc. 8<sup>th</sup> Int. Conf. on Zinc Alloy Coated Steel Sheet, Galvatech'11, Genova, Italy, June 21-24, 2011, Association for Iron and Steel Technology.
- Strohmeier, B.R. and D.M. Hercules. 1984. *J. Phys. Chem.* 88: 4992-4929.
- Swaminathan, S., T. Koll, M. Pohl and M. Spiegel. 2007. Proc. 7<sup>th</sup> Int. Conf. on Zinc Alloy Coated Steel Sheet, Galvatech'07, Osaka, Japan, November 18-22, 2007, Association for Iron and Steel Technology: 460-465.
- Tanaka, T., M. Nishida, K. Hashiguchi and T. Kato. 1979. In R.A. Kot and J.W. Morris (Eds.), *Structure and Properties of Dual-Phase Steels*. New Orleans, LA.: The Metallurgical Society of AIME: 221-241.
- Tang, N. 1995. *Metall. Mater. Trans. A* 26A: 1699-1704.
- Tang, N.-Y. 1998. *Zinc-Based Steel Coating Systems: Production and Performance*. TMS, Warrendale, PA, USA: 3-12.
- Tang, N.-Y. 1999. *Metall. Mater. Trans. B* 30: 144-148.
- Teixeira, S. R., P. H. Dionisio, E. F. D. Silveira, F. L. F. Jr, W. H. Schreiner and I. J. R. Baumvol. 1987. *Mat. Sci. Eng. A* 96: 267-277.
- Thorning, C. and S. Sridhar. 2007. *Philos. Mag.* 87: 3479-3499.
- Toussaint, P., L. Segers, R. Winand and M. Dubois. 1998. *ISIJ Int.* 38: 985-990.
- Vanden Eynde, X., J. P. Servais and M. Lamberigts. 2002. *Surf.Interface Anal.* 33: 322-329.

Vanden Eynde, X., J. P. Servais and M. Lamberigts. 2003. Surf.Interface Anal.35: 1004-1014.

Vanden Eynde, X., J.P. Servais and M. Lamberigts. 2004. Proc. 6th Int. Conf. on Zinc Alloy Coated Steel Sheet, Galvatech'04, Chicago, IL, USA, April 4-7, 2004, Association for Iron and Steel Technology: 361-372.

Wagner, C. 1959. Zeitschrift für Elektrochemie 63: 772-782.

Wang, K.-K., H.-P.Wang, L. Chang, D. Gan, T.-R.Chen and H.-B. Chen. 2009. Proceedings of the Asia-Pacific Galvanizing Conference, The Corrosion Science Society of Korea, Jeju, Korea, November 8-12, paper A-32.

Wang, K.-K., L. Chang, D. Gan and H.-P.Wang. 2010. Thin Solid Films. 518: 1935-1942.